

Miss CR-65364

STRUCTURAL AND DYNAMIC ANALYSIS OF THE APOLLO AFT HEAT SHIELD

by

R.H. Gallagher, R.A. Gellatly, J.R. Batt

REPORT NO. D7218-933004

DECEMBER 1965

Final Report

NASA Contract NAS 9-3528

Prepared For

The National Aeronautics and Space Agency
Manned Spacecraft Center
Houston, Texas

LIBRARY COPY

MAY 3 1966

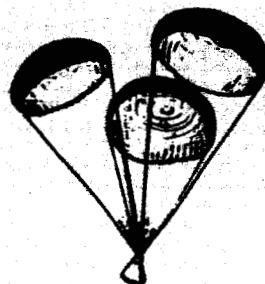
MANNED SPACECRAFT CENTER
HOUSTON, TEXAS

GPO PRICE \$ _____

CFSTI PRICE(S) \$ _____

Hard copy (HC) 5.00

Microfiche (MF) 1.00



11 653 July 65



BELL AEROSYSTEMS A **Textron** COMPANY

Facility Form 602

N66 27053 (ACCESSION NUMBER)	(THRU)
157 (PAGES)	(CODE)
CR-65364 (NASA CR OR TMX OR AD NUMBER)	(CATEGORY)

STRUCTURAL AND DYNAMIC ANALYSIS OF THE APOLLO AFT HEAT SHIELD

by

R.H. Gallagher, R.A. Gellatly, J.R. Batt

REPORT NO. D7218-933004

DECEMBER 1965

Final Report

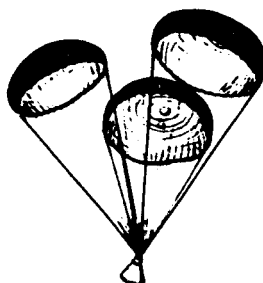
NASA Contract NAS 9-3528

Prepared For

The National Aeronautics and Space Agency

Manned Spacecraft Center

Houston, Texas



BELL AEROSYSTEMS A **Textron** COMPANY

FOREWORD

Work described in this report was performed by personnel of Textron's Bell Aerosystems Company for the Structures and Mechanics Division of the NASA Manned Spacecraft Center, Houston, Texas under contract NAS 9-3528. The work was performed in the period September 12, 1964 to March 1, 1966 under the direction of Mr. R.H. Gallagher, who acted as Principal Investigator. The effort was monitored by Mr. F.J. Stebbins of the Structures and Mechanics Division, NASA Manned Spacecraft Center.

The subject effort entailed contributions from many disciplines and therefore represents the contributions of numerous individuals other than the cited authors. The authors are particularly appreciative of the support provided this project by Messrs. F. Braun, and W. Luberacki.

ABSTRACT

27053

Analyses are performed of the Apollo Aft Heat Shield for conditions of water impact and thermal stress. The water impact condition is first treated as a quasi-static problem in the determination of localized stresses of a critical nature. Two separate temperature profiles are examined in the solution for thermal stresses.

Dynamic response and elastic instability analyses are performed for a limited number of conditions in order to confirm the influence of these effects with respect to the quasi-static solution. The concepts of discrete element analysis, as they pertain to the Apollo Aft Heat Shield, are reviewed and more advanced and satisfactory idealization procedures are defined.

CONTENTS

Section		Page
I	INTRODUCTION	I-1
II	BASIC DESIGN ANALYSES	II-1
	A. Objectives	II-1
	B. Description of Procedure	II-1
	C. Material Properties	II-8
	D. Effects of Gridwork Refinement	II-8
	E. Analyses in Support of Design Changes	II-14
	F. Analyses for Critical Impact Cases	II-17
	G. Thermal Stress Analyses	II-37
III	DYNAMIC RESPONSE	III-1
	A. Introduction	III-1
	B. Structural Idealization	III-1
	C. Load-Time Histories	III-4
	D. Dynamic Response	III-9
IV	INSTABILITY ANALYSES	IV-1
	A. Objectives	IV-1
	B. Description of Procedure	IV-1
	C. Evaluation Analyses	IV-6
	D. Analysis Results	IV-12
	1. Idealized Heat Shield - Uniform Pressure	IV-12
	2. Actual Heat Shield - Water Impact Cases	IV-13
	E. Finite Displacement Considerations	IV-14
V	DISCRETE ELEMENT PROPERTIES	V-1
	A. Historical Background	V-1
	B. Sandwich Element	V-2
	C. Interelement Compatible Elements	V-8
VI	ANALYTICAL SOLUTIONS	VI-1
	A. Governing Equations	VI-1
	B. Heat Shield with Overhang	VI-4
	C. Solution for Uniform Thermal Force and Uniform Thermal Moment	VI-7
VII	CONCLUDING REMARKS	VII-1
	Appendix A	A-1
	Appendix B	B-1
	Appendix C	C-1
VIII	REFERENCES	VIII-1

ILLUSTRATIONS

Figure		Page
II-1	Block No. 2 - Apollo Aft Heat Shield Scalloped Face Thickness	II-2
II-2	Heat Shield with Scalloped Face Thickness - Analyses Gridwork (Node Point Location)	II-3
II-3	Plate Elements for Heat Shield Analyses	II-6
II-4	Temperature Dependence of Material Properties	II-9
II-5	Heat Shield Gridwork with Scalloped Face Thickness	II-10
II-6	Effects of Grid Refinement	II-16
II-7	Average Pressure versus Time 35 ft/sec	II-18
II-8	Deflection Along Load Axis of Symmetry, $\phi = 16.5^\circ$	II-19
II-9	Deflection Along Load Axis of Symmetry, $\phi = 16.5^\circ$	II-20
II-10	Deflection Along Load Axis of Symmetry, $\phi = 19.6^\circ$	II-21
II-11	Deflection Along Load Axis of Symmetry, $\phi = 19.6^\circ$	II-22
II-12	Deflection Along Load Axis of Symmetry, $\phi = 29.2^\circ$	II-23
II-13	Deflection Along Load Axis of Symmetry, $\phi = 29.2^\circ$	II-24
II-14	Deflection Along Load Axis of Symmetry, $\phi = 10^\circ$	II-25
II-15	Deflection Along Load Axis of Symmetry, $\phi = 15^\circ$	II-26
II-16	Deflection Along Load Axis of Symmetry, $\phi = 20^\circ$	II-27
II-17	Deflection Along Load Axis of Symmetry, $\phi = 25^\circ$	II-28
II-18	Maximum Face Stress	II-29
II-19	Shear Along the Bolt Circle $\phi = 15^\circ$, R = 25 in.	II-31
II-20	Shear Along the Bolt Circle $\phi = 15^\circ$, R = 30 in.	II-32
II-21	Shear Along the Bolt Circle $\phi = 20^\circ$, R = 20 in.	II-33
II-22	Maximum Core Shear Inside and Outside the Bolt Circle	II-34
II-23	Variation of Maximum Face Stress with Impact Angle	II-35
II-24	Variation of Maximum Shear Stress with Impact Angle	II-36
II-25	Thermal Analyses Gridwork	II-38
II-26	Thermal Displacements	II-46
II-27	Thermal Stresses in Upper Sandwich Face - Cold Soak Condition	II-48
II-28	Thermal Stresses in Lower Sandwich Face - Cold Soak Thermal Condition	II-49
II-29	Thermal Stresses in Lower Sandwich Face - Thermal Reentry Condition	II-50
II-30	Thermal Stresses in Upper Sandwich Face - Thermal Reentry Condition	II-51
II-31	Thermal Stresses in Top Surface of the Ablator Cold Soak Thermal Condition	II-52

ILLUSTRATIONS (CONT)

Figure		Page
III-1	Heat Shield Structural Idealization Grid	III-2
III-2	Pressure and Radius Time Histories	III-7
III-3	Forcing Function - Grid Point 7	III-8
III-4	Forcing Function - Grid Point 57	III-9
III-5	Heat Shield First Vibration Mode Shape ($f_1 = 92.26$ cps)	III-10
III-6	Heat Shield Second Vibration Mode Shape ($f_2 = 104.74$ cps) . . .	III-11
III-7	Generalized Coordinate versus Time	III-14
III-8	Generalized Coordinate versus Time	III-15
III-9	Total Displacement versus Time	III-16
III-10	Displacement Along Load Axis of Symmetry Impact Angle $\phi = 15^\circ$	III-17
III-11	Deflection Along Load Axis of Symmetry Impact Angle $\phi = 15^\circ$	III-18
IV-1	Simple Frame for Illustration of Instability Analysis Procedure	IV-2
IV-2	Frame for Numerical Analysis	IV-4
IV-3	Deep Arch - Uniform Pressure	IV-7
IV-4	Spherical Cap - Uniform Pressure	IV-9
IV-5	Heat Shield with Constant Face Thickness Uniform Pressure	IV-10
IV-6	Gridwork for Instability Analyses of Heat Shield with Scalloped Faces	IV-11
IV-7	Heat Shield with Scalloped Face Thickness, 10 in. Radius Loaded Area, $\phi = 10^\circ$	IV-15
IV-8	Heat Shield with Scalloped Face Thickness, 20 in. Radius Loaded Area, $\phi = 10^\circ$	IV-16
IV-9	Heat Shield with Scalloped Face Thickness, 40 in. Radius Loaded Area, $\phi = 10^\circ$	IV-17
V-1	Triangular Sandwich Plate Element	V-3
V-2	Heat Shield Quadrant Triangular Sandwich Panel	V-4
V-3	Comparison of Results - Deflection Along Centerline Due to a Unit Load Applied at the Crown	V-6
V-4	Deflection Predictions versus Gridwork Refinement for Various Core Shear Rigidities	V-7
V-5	Error in Central Deflection Due to Neglect of Shear Deformation	V-9
V-6	Quadrilateral Plate Flexure Element	V-11
V-7	Triangular Plate Flexure Element	V-13
VI-1	Basic Geometry	VI-2
VI-2	Analysis Conditions for Overhang Core	VI-5

TABLES

Number		Page
II-1	Node Point Coordinates - Coarse Grid	II-7
II-2	Node Point Coordinates - Refined Grid	II-11
II-3	Analyses Prior to March 1, 1965	II-15
II-4	Node Point Coordinates - Thermal Stress Analysis Grid	II-39
II-5	Reentry Temperatures and Ablator Thicknesses	II-40
II-6	Element Thermal Stress Analysis Data	II-41
II-7	Table Displacement Normal to Surface - Thermal Cases	II-47
III-1	Node Point Coordinates - Dynamic Analyses - Revised Grid . .	III-5
III-2	Vibration Mode and Frequency Data	III-9
IV-1	Example Frame Results	IV-4

I. INTRODUCTION

In September, 1964, the NASA Manned Spacecraft Center contracted with Bell Aerosystems Company for a six-month study of the application of the discrete element structural analysis method to the prediction of thermal stresses in the Apollo command module aft heat shield. Shortly thereafter, in Dec., 1964, the Apollo aft heat shield sustained damage during tank-testing, occasioning efforts directed towards structural design changes, particularly with respect to the scalloping of the face sheets. Bell Aerosystems Company was asked to assist in this work, via an extension of the contract, and numerous analyses were performed to guide the specific nature of the scalloping to be effected.

The latter effort, which was conducted within a very short period of time, was amplified in March 1965 into a more extensive examination of the heat shield with respect to water impact and thermal stressing conditions. This work is described in detail herein. Other objectives include the substantiation for this class of structure of the principal analysis technique--the matrix discrete element approach--through comparisons with experimental and classical analysis results, and the development of design data for the general heat shield problem.

To meet these objectives, the subject effort was divided into five areas of activity each with subsidiary work items. These are the

- (1) performance of basic design analyses for water impact, treated as a quasi-static problem, and for thermal stress conditions.
- (2) performance of dynamic response analyses for a limited number of conditions.
- (3) determination of buckling pressures for water impact conditions
- (4) examination of discrete element stiffness equations for more accurate matrix analysis of heat shield structures.
- (5) development of a classical solution and, from this, design charts for anticipated heat shield design problems.

Section II of this report describes the work performed in connection with basic design analyses. These analyses exclude the effects of dynamic behavior and elastic instability. Included are assessments of convergence characteristics, two thermal stress analyses, and an extensive series of analyses representing a quasi-static treatment of water impact conditions.

Analyses in which the effects of dynamic response are neglected generate results which are expected to be conservative. Since it is desirable to obtain a quantitative estimate of the degree of conservatism, if any, involved in the static analysis, the dynamic response of the Apollo aft heat shield to water impact was determined. One

impact angle was chosen and histories of the loading at all affected points were defined. The results of this effort appear in Section III.

Elastic instability effects are examined in Section IV. The water impact condition produces membrane stress throughout the heat shield and it is conceivable that these stresses could be large enough to produce a failure of the heat shield in an elastic instability mode. Thus, using a discrete element approach to linear instability analysis, computations were performed for three distributions of pressure to determine the intensity of pressure to cause buckling. The results, which were modified by means of empirical factors to account for the influence of nonlinear effects on buckling, indicate a small but positive margin of safety.

The questions of an appropriate discrete element idealization for the Apollo aft shield are examined in Section V. The significance of the heat shield as a sandwich structure is considered and it is found that principal modes of behavior are represented with sufficient accuracy by means of conventional thin plate formulations. A discrete element formulation for sandwich structures is advanced, however, and it is shown that it holds promise for accurate representation of shallow sandwich shells, provided a high degree of gridwork refinement is feasible. The existing discrete element formulations for shallow shell analysis are reviewed and it is found that new approaches, based on satisfaction of interelement compatibility requirements, hold promise for resolution of difficulties inherent in the present formulations.

A classical approach to the problem of analyzing the Apollo heat shield is presented in Section VI. This approach covers both thermal stress and applied load situations and is extended to account for the overhang of the heat shield beyond the bolt circle. Conclusions are presented in Section VII.

The detailed aspects of the discrete element procedures for instability and dynamic analysis are given in two appendixes. Another Appendix describes the Bell General Purpose Structural Analysis Computer Program.

II. BASIC DESIGN ANALYSES

A. OBJECTIVES

Within the design analyses, a number of classes of problems have been treated. These include

- (1) Analyses to determine the effects of grid refinements
- (2) Analyses in support of the design activity which took place during January 1965
- (3) Analyses to determine critical water impact cases.
- (4) Analyses for the stresses and displacements of the shield under elevated temperature conditions

The actual structure of the Aft Apollo Heat Shield is drawn in Figure II-1. This is the "Block 2" heat shield, with sculptured face sheets. Since the specified loadings, which arise from either water impact pressures or temperature, are symmetric about the axis of geometric symmetry, only one half the heat shield is considered in analyses.

Detailed objectives of the above three types of analyses, together with the results obtained, will be presented following a brief review of the analysis procedure and the material properties common to all analyses.

Included were an extensive series of analyses performed during early phases of the project in conjunction with unscaloped designs, various arrangements of the scalloping, and with the verification of test results from experiments conducted on the ATR-209 heat shield specimen.

B. DESCRIPTION OF PROCEDURE

The analyses of the Apollo aft heat shield described in this section were performed with use of the Bell General Purpose Structural Analysis Program. This program is based on the discrete element approach to matrix structural analysis. A complete description of the theoretical basis of the program, together with an outline of program capabilities, is presented in Appendix A.

Figure II-2 illustrates a typical idealization of the heat shield structure by means of discrete elements. In the idealization shown, five different types of element are employed.

- (1) quadrilateral plate in plane stress
- (2) triangular plate in plane stress.

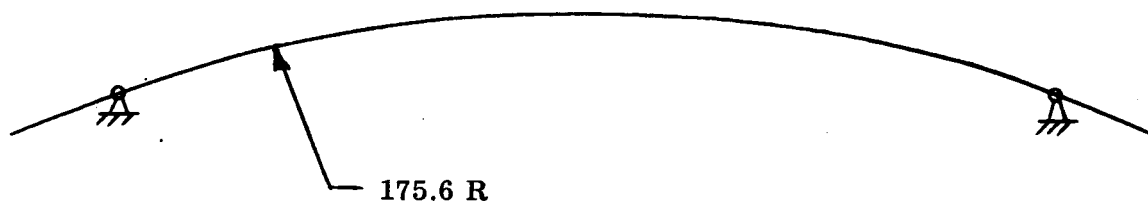


Figure II-1a

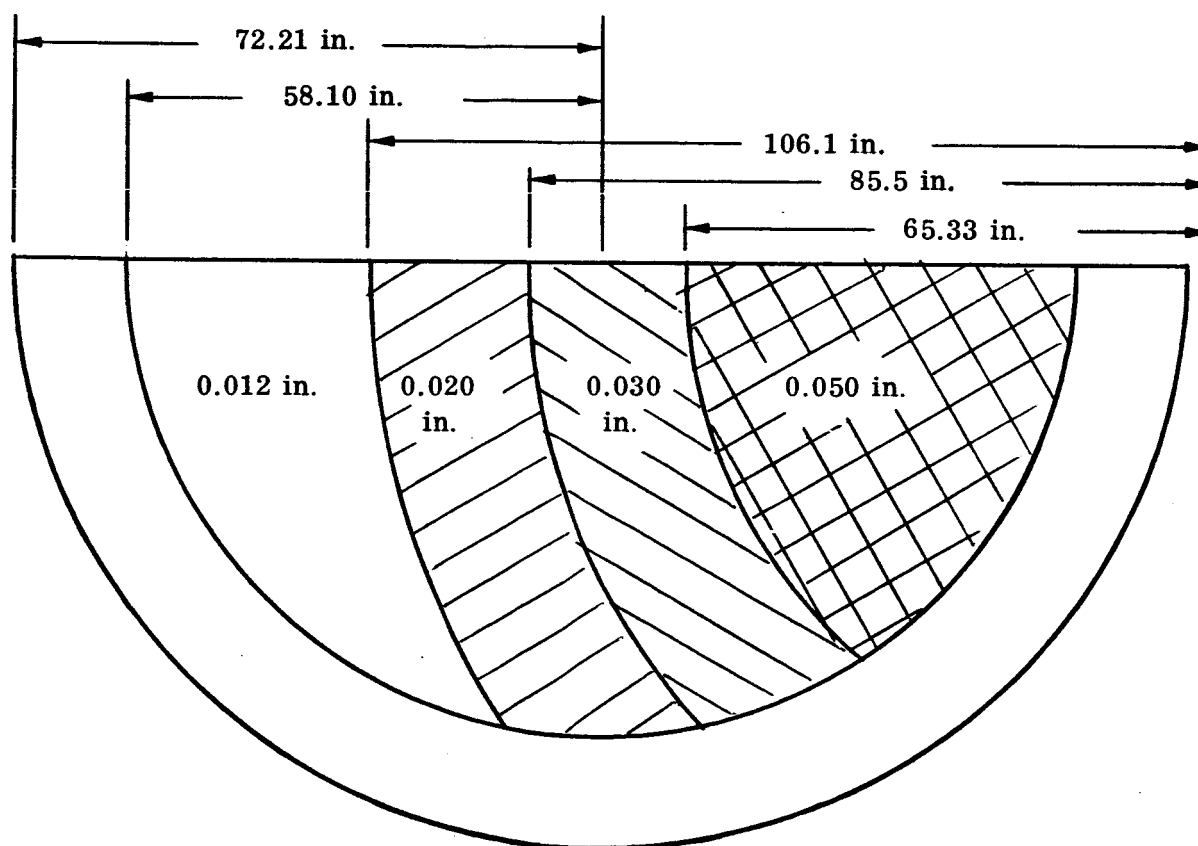


Figure II-1b

Figure II-1b. Block No. 2 - Apollo Aft Heat Shield Scalloped Face Thickness

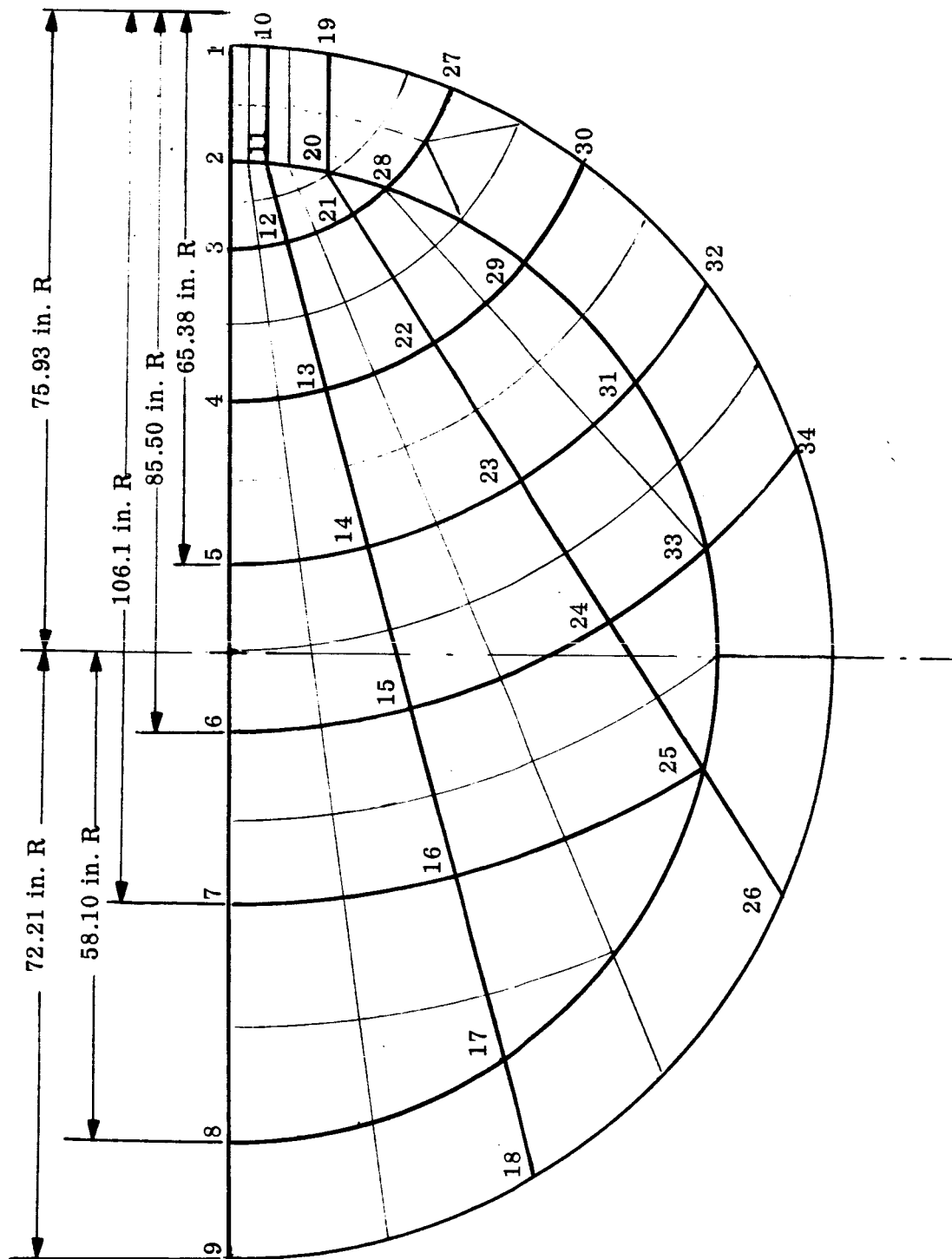


Figure II-2. Heat Shield With Scalloped Face Thickness - Analysis Gridwork (Node Point Location)

- (3) quadrilateral plate in bending
- (4) triangular plate in bending
- (5) axial-flexural-twist element

The first four elements are actually representative of two physical elements of the structure, the quadrilateral and triangle. These elements appear in Figure II-3. From a theoretical standpoint, it is necessary to divide the deformational behavior of these elements into plane stress and flexural behavior, respectively.

A detailed development of the pertinent analytical relationships for these plate elements, in the form of the pertinent stiffness matrices and terms for thermal stress analysis, is given in Reference 3. It should be noted that the flexural properties for both elements are based on simple assumed displacement assumptions of polynomial form.

In establishing the membrane and flexural rigidities of the plate element, for water impact analysis, the sandwich form of construction requires special consideration. Denoting the face thickness as t_f , the membrane rigidity, D_m can be written as

$$D_m = \frac{E(2t_f)}{(1-\mu^2)} \quad (\text{II-1})$$

where μ is Poisson's ratio. Any direct stress carrying capacity of the ablator, bond, and core is disregarded in the water impact computations. (The ablator is included in analyses for thermal stress conditions.) The membrane rigidity is normally expressed as

$$D_m = \frac{Et_m}{(1-\mu^2)} \quad (\text{II-2})$$

Hence, by comparison of II-1 and II-2

$$t_m = 2t_f \quad (\text{II-3})$$

For the flexural rigidity at a plate, D_b , one can write

$$D_b = \frac{Et_b^3}{12(1-\mu^2)} \quad (\text{II-4})$$

In the case of the sandwich, however, the flexural rigidity is actually

$$D_b = \frac{Et_f h^3}{2(1-\mu^2)} \quad (\text{II-5})$$

Comparing II-4 and II-5

$$t_b = \sqrt[3]{6t_f h^2} \quad (\text{II-6})$$

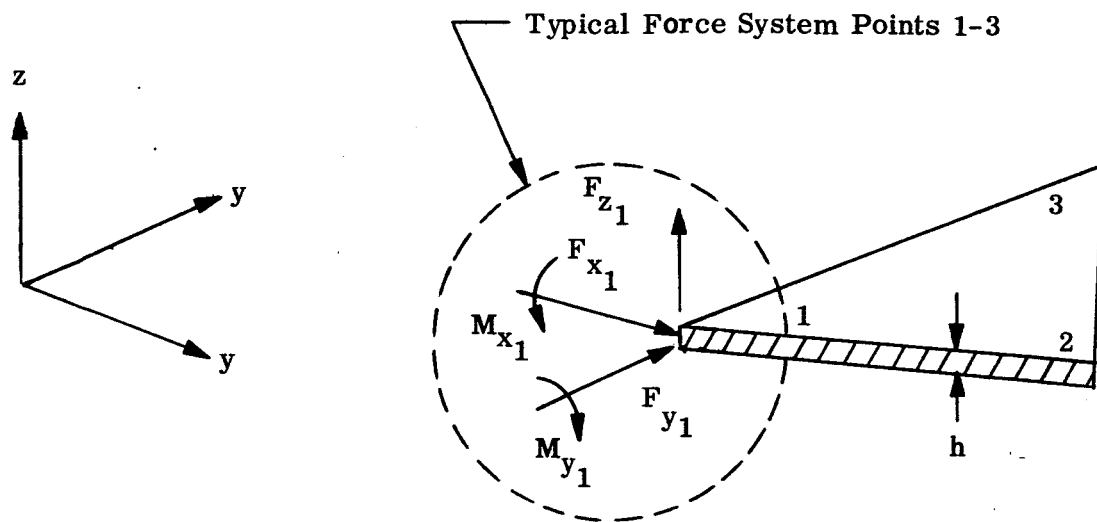
The following is a listing of the equivalent thicknesses, t_m and t_b , as computed from equations II-3 and II-5, for the various face thicknesses for sandwich portions of interest ($h = 2.0$ in.) are:

t_f	t_m	t_b
0.008	0.016	0.577
0.012	0.024	0.661
0.020	0.040	0.783
0.030	0.060	0.896
0.050	0.100	1.063
*	0.025	0.513

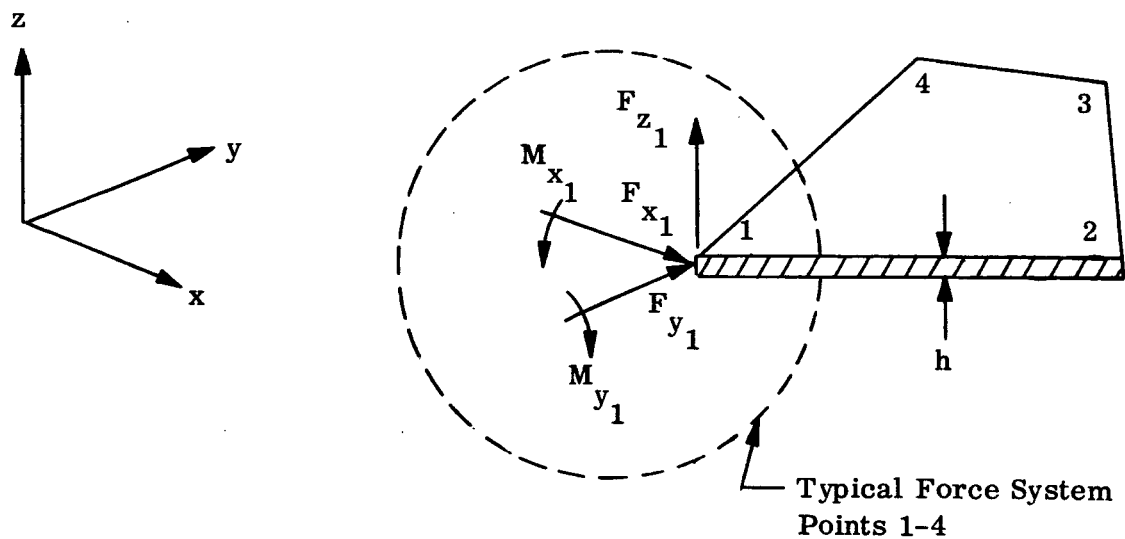
*Corrugated torus flange

The fifth element cited previously is the axial flexural-torsional element used to represent the ring at the circumference of the heat shields in the analyses where the corrugated torus was included. The section properties used were:

Area	=	0.235 in. ²
Moment of Inertia about the X' Axis	=	0.309 x 10 ⁻² in. ⁴
Moment of Inertia about the Y' Axis	=	0.650 x 10 ⁻² in. ⁴
Torsional Rigidity	=	0.710 x 10 ⁻² in. ⁴



a. Triangular Plate Element



b. Quadrilateral Plate Element

Figure II-3. Plate Elements for Heat Shield Analysis

TABLE II-1
 NODE POINT COORDINATES - COARSE GRID
 (See Figure II-2 for Layout)

Node Point			
1	-72.21	0	160.066
2	-58.100	0	165.710
3	-47.982	0	168.919
4	-29.266	0	173.144
5	-10.550	0	175.283
6	9.570	0	175.338
7	30.170	0	172.989
8	58.100	0	165.710
9	72.210	0	160.066
10	-72.032	5.063	160.066
11	-57.879	5.063	165.710
12	-49.021	7.550	168.450
13	-31.001	12.606	172.382
14	-12.981	17.663	174.227
15	6.392	23.094	173.957
16	26.226	28.659	171.250
17	46.797	34.433	165.710
18	61.121	38.451	160.066
19	-71.210	11.973	160.066
20	-56.853	11.973	165.710
21	-52.259	14.859	166.984
22	-36.407	24.809	169.985
23	-20.555	34.759	170.894
24	-3.514	45.456	169.578
25	13.935	56.404	165.710
26	29.260	66.016	160.066
27	-67.158	26.535	160.066
28	-55.050	18.577	165.710
29	-45.854	35.680	165.710
30	-57.962	43.066	160.066
31	-32.046	48.463	165.710
32	-44.153	57.139	160.066
33	-12.055	56.836	165.710
34	-24.163	68.047	160.066

C. MATERIAL PROPERTIES

The cross section of the Aft Apollo Command Module Heat Shield is shown in Figure II-1. Since the properties of the bond are neglected in all analyses described in this report, the materials of interest are the ablator, the face sheets of the sandwich skins, and the core of the sandwich. Only the face sheet properties play a role in water impact analyses and for these the properties are assumed constant at the following values.

Modulus of Elasticity

$$E = 29.5 \times 10^6 \text{ psi}$$

Poisson's Ratio

$$\mu = 0.30$$

Specific Weight

$$\rho = 0.283 \text{ lb/in.}^3$$

Also, in examination of the pertinence of core shear deformation effects:

$$E = 10^5 \text{ psi}$$

$$G_c = 2.8 \times 10^4 \text{ psi (Vertical shear-both directions).}$$

For thermal stress analyses, where the significance of the temperature dependence of material properties must be taken into account, the data represented in Figure II-4 was employed.

D. EFFECTS OF GRIDWORK REFINEMENT

In order to determine the influence of gridwork refinement, a comparison of flexibility coefficients using two different grids was carried out.

In defining the basic form of the grids which are to be used in the discrete element analyses of the heat shield, the shape of the sculpturing of the skins must be taken into account. Although all sculpturing contours are based upon radii drawn from a reference point lying outside the heat shield, a grid which is principally polar with the reference point as origin appears to be the most attractive from the standpoint of the overall planform. A grid using this concept is presented in Figure II-5. In this case, there are 100 node points, each possessing five degrees of freedom (rotational freedom about a normal to the shell surface is basically deleted). When the boundary conditions are introduced, the total number of degrees of freedom is reduced to slightly below the maximum of 492 allowable in the Bell General Purpose Analysis Program. This grid then is typical of the maximum refinement in any particular area would necessitate an increase in the element size elsewhere.

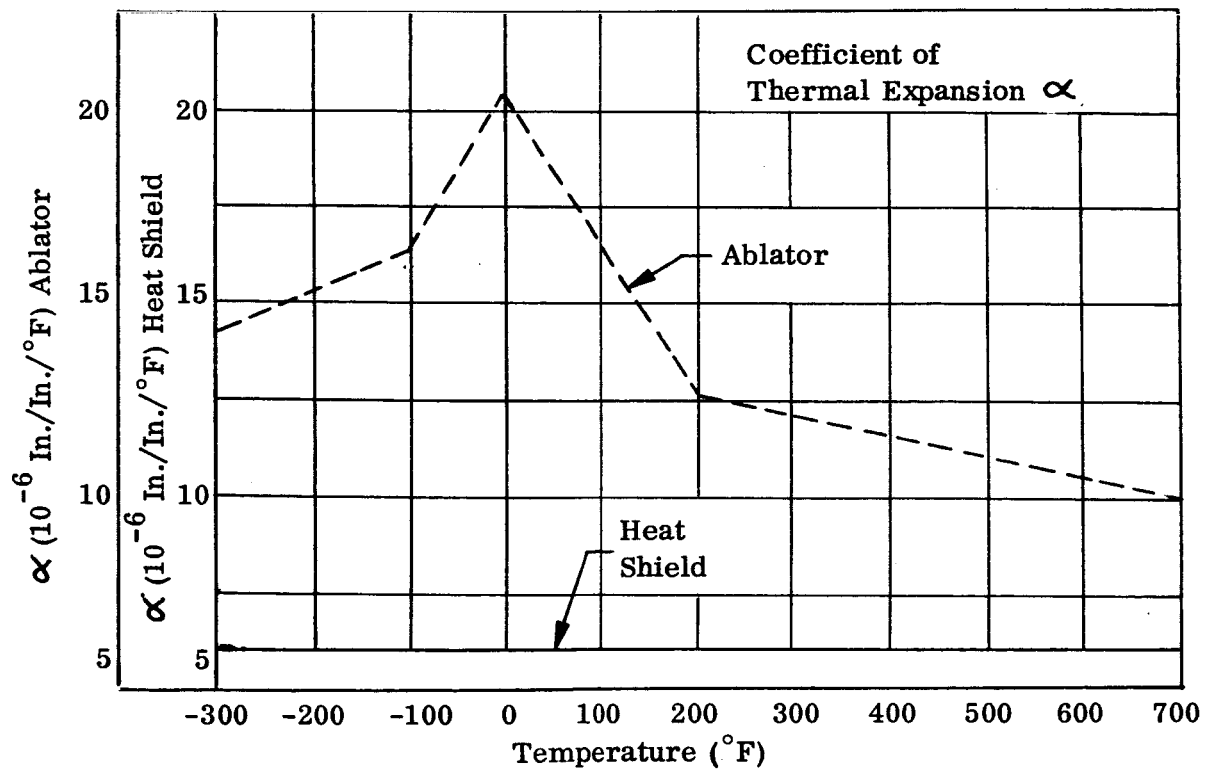
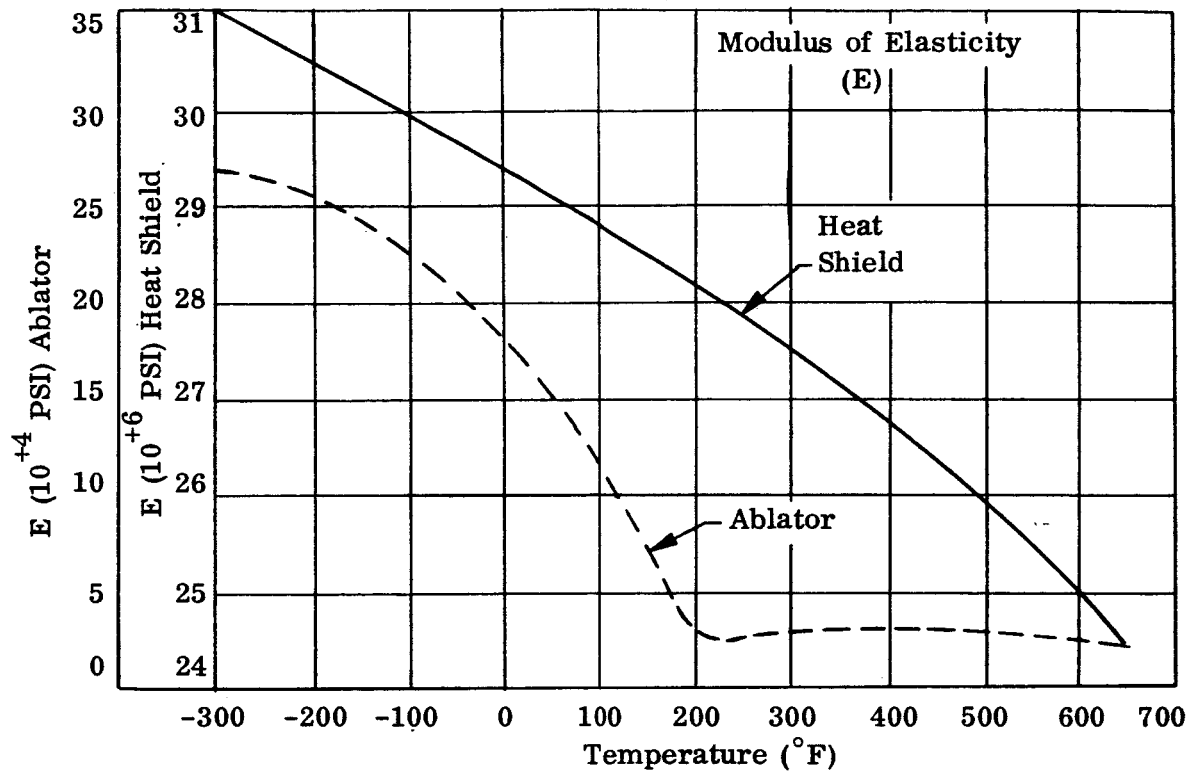


Figure II-4. Temperature Dependence of Material Properties

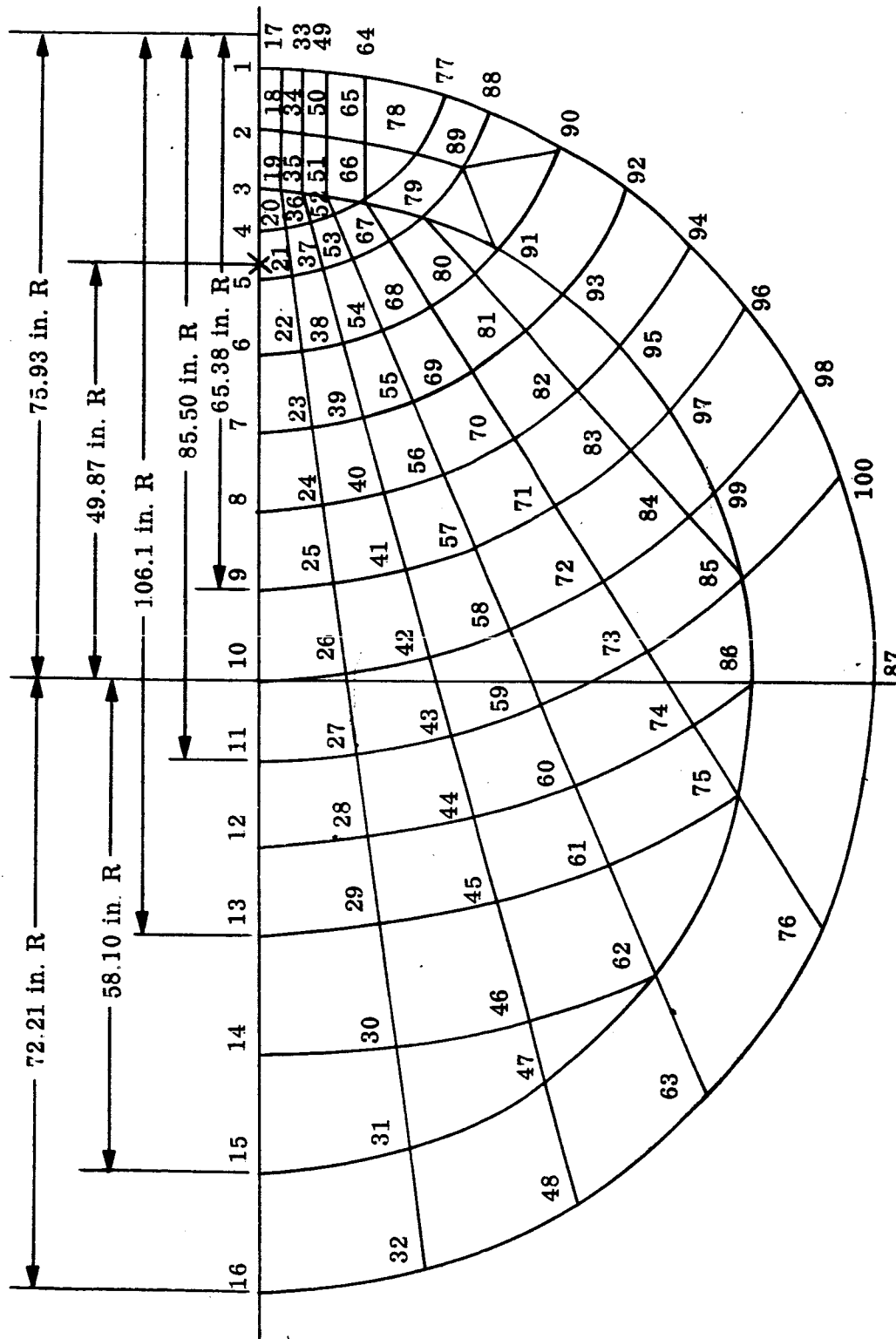


Figure II-5. Heat Shield Gridwork With Scalloped Face Thickness

TABLE II-2
NODE POINT COORDINATES - REFINED GRID

Node Pt.	X	Y	Z
1	-72.21	0	160.066
2	-65.155	0	163.065
3	-58.10	0	165.710
4	-53.407	0	167.282
5	-47.982	0	168.919
6	-38.624	0	171.300
7	-29.266	0	173.144
8	-19.908	0	174.468
9	-10.55	0	175.283
10	0	0	175.6
11	9.57	0	175.339
12	19.87	0	174.473
13	30.17	0	172.989
14	44.135	0	169.964
15	58.10	0	165.710
16	72.21	0	160.066
17	-72.167	2.504	160.066
18	-65.107	2.504	163.065
19	-58.046	2.504	165.710
20	-53.625	3.126	167.182
21	-48.253	3.883	168.796
22	-38.986	5.184	171.140
23	-29.718	6.479	174.114
24	-20.451	7.781	174.231
25	-11.184	9.083	175.008
26	-0.736	10.546	175.282
27	8.741	11.877	174.980
28	18.941	13.309	174.067
29	29.141	14.741	172.537
30	42.971	16.678	169.442
31	55.115	18.383	165.710
32	69.278	20.368	160.066
33	-72.032	5.063	160.066
34	-64.958	5.063	163.065
35	-57.879	5.063	165.710
36	-54.244	6.083	166.901
37	-49.021	7.550	168.450
38	-40.011	10.078	170.684
39	-31.001	12.606	172.382
40	-21.991	15.134	173.560
41	-12.981	17.663	174.227

TABLE II-2 (CONT)

Coordinates

Node Pt.	X	Y	Z
42	-2.823	20.512	174.375
43	6.392	23.094	173.957
44	16.309	25.877	172.915
45	26.226	28.659	171.250
46	39.672	32.431	167.958
47	46.797	34.433	165.710
48	61.121	38.451	160.066
49	-71.796	7.719	160.066
50	-64.696	7.719	163.065
51	-57.585	7.719	165.710
52	-55.171	8.738	166.480
53	-50.171	10.843	167.931
54	-41.547	14.476	170.000
55	-32.922	18.106	171.533
56	-24.297	21.737	172.549
57	-15.672	25.368	173.050
58	-5.948	29.460	173.009
59	2.872	33.174	172.415
60	12.365	37.170	171.176
61	21.858	41.167	169.301
62	34.734	46.574	165.710
63	49.343	52.721	160.066
64	-72.210	11.973	160.066
65	-64.045	11.973	163.065
66	-56.853	11.973	165.710
67	-52.259	14.859	166.984
68	-44.333	19.833	168.751
69	-36.407	24.809	169.985
70	-28.481	29.784	170.696
71	-20.555	34.759	170.894
72	-11.619	40.366	170.502
73	-3.514	45.456	169.578
74	5.212	50.928	167.972
75	13.935	56.404	165.710
76	29.260	66.016	160.066
77	-68.961	21.416	160.066
78	-62.597	18.140	163.065
79	-55.050	18.577	165.710
80	-48.060	24.800	167.064
81	-41.068	31.019	167.889
82	-34.077	37.240	168.188

TABLE II-2 (CONT)

Coordinates

Node Pt.	X	Y	Z
83	-27.086	43.461	167.967
84	-19.205	50.474	167.089
85	-12.055	56.836	165.710
86	0	58.10	165.710
87	0	72.21	160.066
88	-67.158	26.535	160.066
89	-60.776	23.483	163.065
90	-63.136	35.045	160.066
91	-51.029	27.779	165.710
92	-57.962	43.066	160.066
93	-45.854	35.680	165.710
94	-51.634	50.480	160.066
95	-39.527	42.582	165.710
96	-44.153	57.139	160.066
97	-32.046	48.463	165.710
98	-34.336	63.524	160.066
99	-22.228	53.680	165.710
100	-24.163	68.047	160.066

The overall effects of grid refinement can, therefore, be studied by simplifying the mesh of Figure II-5 . One scheme is to omit alternate grid and radial lines. It is important, in the assessment of convergence characteristics, to utilize a regular and consistent refinement of the grid. This new grid (see Figure II-2) then represents effectively the coarsest acceptable mesh. Any further reduction in the number of node points would introduce elements of unreasonable size.

Using these two grids, and with constant face thicknesses for simplicity, static analyses were performed and inter alia the influence coefficient matrix (inverse of the stiffness matrix) obtained. The direct flexibilities for all node points on the axis of symmetry have been selected as realistic characteristics of the structure and are presented in Figure II-6 . The curves are not simple deflections under a fixed loading system, but are the deflections at each individual node point for a unit load applied at that point.

As can be seen, the agreement between the two curves is very good, especially in the region in which impact loads will occur, i.e. to the right of center as drawn. The larger discrepancies between the curves, which occur to the left of center, are associated with the relatively larger discrete elements used in that region. In an actual problem, where the loading does not extend over the entire heat shield, the influence of the above differences is of reduced significance. From this comparison, it can be concluded that the coarse gridwork used in the dynamic and instability analysis investigations, described in later sections, yield acceptably accurate results. The more refined grid is retained in the present static design analyses in order to provide more detailed information about the peak stresses.

E. ANALYSES IN SUPPORT OF DESIGN CHANGES

Work on the subject contract was initiated during September, 1964. During the period between then and March 1, 1965, a succession of analyses were performed in attempts to resolve critical problems which arose as a series of new design conditions, proportions, and arrangement were to meet requirements imposed by water impact. Included were analyses which were solely intended to verify the discrete element approach as an applicable tool for heat shield analysis through comparison with heat shield test data.

Table II-3 summarizes the analyses performed prior to March 1, 1965. A total of sixteen analyses were listed. Each is identified by such factors as the gridwork employed, the nature and intensity of the imposed loading condition, the support conditions, etc. Results for these analyses were transmitted to NASA MSC, accompanied by sketches which describe the idealization, etc. Reference can be made to these sketches for further identification of the listed analyses.

TABL
ANALYSES PRIOR

Run	Grid	Pressure psi	r''*	Impact Center
1	I	50	43.0	z = 36
2	I	100	43.0	z = 36
3	II	Variable		
4	III	Variable		
	IV			
5	V	100	13	10° z 30
6	V	100	13	15° z 44
15	V	100	13	15° z 44
7	VI	100	13.2	15° z 44
14	VII	100	13.2	15° z 44
8	VIII	100	10	10° z 30
9	VIII	100	13	10° z 30
10	VIII	100	15	10° z 30
11	VIII	100	10	15° z 44
12	VIII	100	13	15° z 44
13	VIII	100	15	15° z 44
16	IX	100	13	15° z 44

*Radius of Loaded Area

+ The notation "spring" refers to the use of an approximation for the flexibility of the conic section of the command module structure

Report No. 7218-933004

II-15
0

E II-3

TO MARCH 1, 1965

Face Sheets	Boundary Conditions	Group	Case
0.008	Simple Support, Torus Spring ⁺		
0.008			
0.008	ATR 209 Torus Free		
0.008	ATR 209 Torus Spring		
0.008	One Quadrant, ATR 209		
0.008	No Springs	4	1
0.008	With Springs	4	2
0.008	No Spring	4	B
Scalloped	Guide Grid, Fixed Support, Torus Free	5	A
Scalloped	Refined Grid, Fixed Support, Torus Free	5	B
Scalloped	Simple Support, Torus Spring	6	B-1
Scalloped	Simple Support, Torus Spring	6	B-2
Scalloped	Simple Support, Torus Spring	6	B-3
Scalloped	Simple Support, Torus Spring	6	B-4
Scalloped	Simple Support, Torus Spring	6	B-5
Scalloped	Simple Support, Torus Spring	6	B-6
0.008 Const	Simple Support, Torus Free	7	

2

II-15

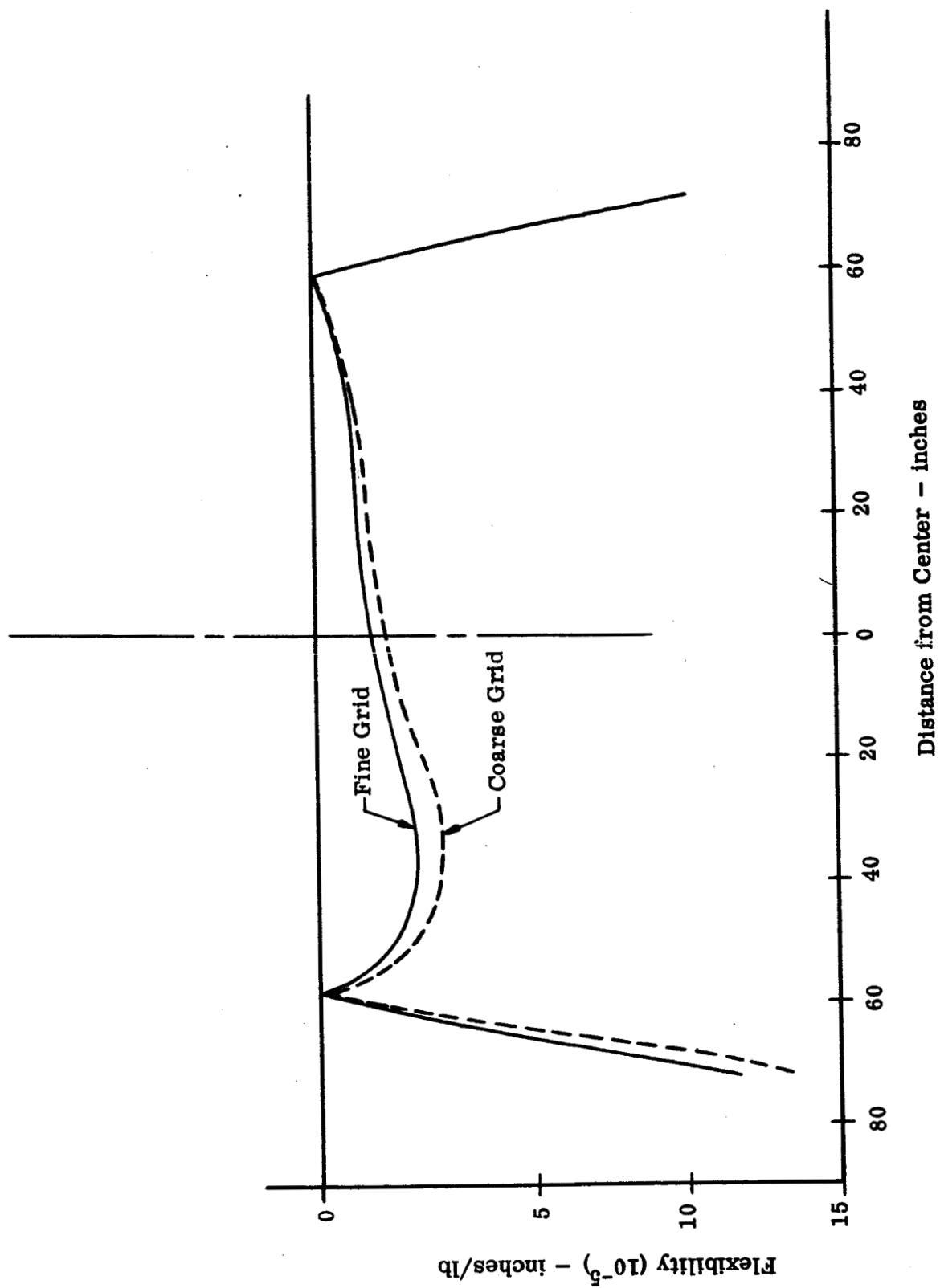


Figure II-6. Effects of Grid Refinement

F. ANALYSES FOR CRITICAL IMPACT CASES

Two general groups of analyses were performed of water impact conditions for the Apollo aft heat shield. One group pertains to drop tests performed by NASA of the BP28 item. These tests are known as tests No. 91, 92 and 93. The second group of analyses, known as the "water impact series", were conducted to determine the critical combinations of impact angle and wetted area in a general manner.

Consider first the drop test analyses. The three tests correspond to water impact angles of 29.2° , 19.6° and 16.5° respectively. In order to provide information over the complete water impact, five circular wetted areas were considered for each of the impact angles. The radii were 10 in., 15 in., 20 in., 25 in. and 40 in. The fifteen design cases were then analyzed using the grid pattern of Figure II-5, with a nominal pressure of 100 psi in each case. The actual pressures for each case are taken from Figure II-7, which presents the pressure-time history for an impact velocity of 35 ft/sec. The corresponding radii of contact areas have been obtained from other data from MSC. The results from the analyses are then scaled by the appropriate factors.

Results, in the form of deflection profiles along the axis of symmetry, are presented in Figures II-8 to II-13 for all fifteen cases considered. The complete results, in the form of displacement components at all of the node points and stresses within the respective elements are listed in the computer analysis printout, furnished with this report.

In the water impact series of analyses the objective was to determine the critical combinations of impact angle and wetted areas for the heat shield. The criteria which were to be applied are those of maximum displacements, maximum membrane stresses in the faces, and maximum shear stresses in the sandwich core.

In order to cover the widest range of conditions, while keeping the amount of data as low as possible, it was decided that four impact angles combined with six wetted areas would provide a sufficient number of analyses. The impact angles used were 10° , 15° , 20° and 25° , and the wetted radii 10 in., 13 in., 15 in., 18 in., 20 in., and 40 in. The velocity of impact has been taken as 35 ft/sec. In general, the refined gridwork shown in Figure II-5 was used.

Figures II-14 to II-17 show the variation of deflection along the axis of symmetry with wetted radius and angle of impact. These show that the maximum deflection occurs in the region between 20 in. and 40 in. radius.

The maximum stress in the faces is shown in Figure II-18. These maximum stresses are obtained as the sum of membrane and bending stresses and occur at various points on the center line of the heat shield.

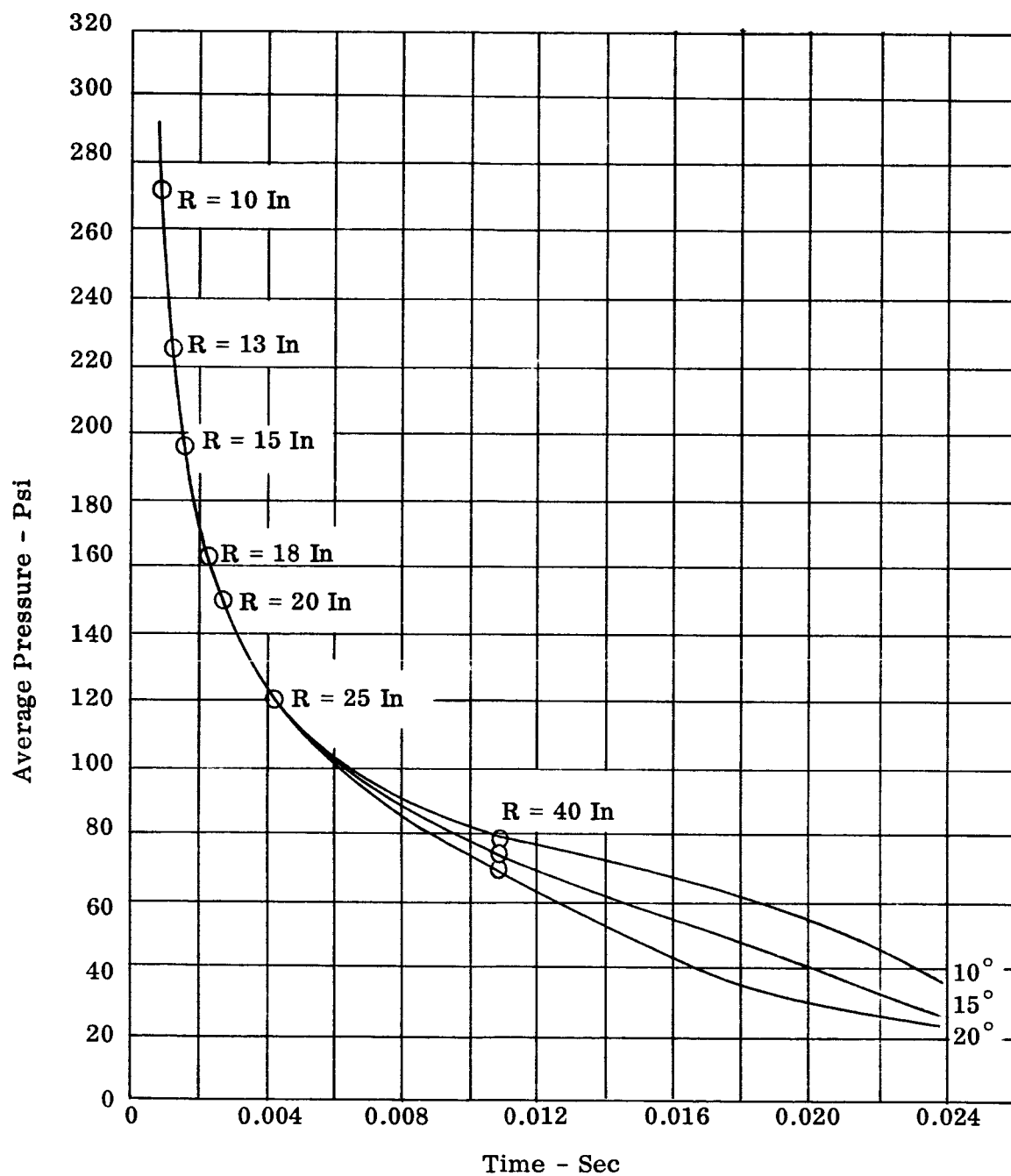
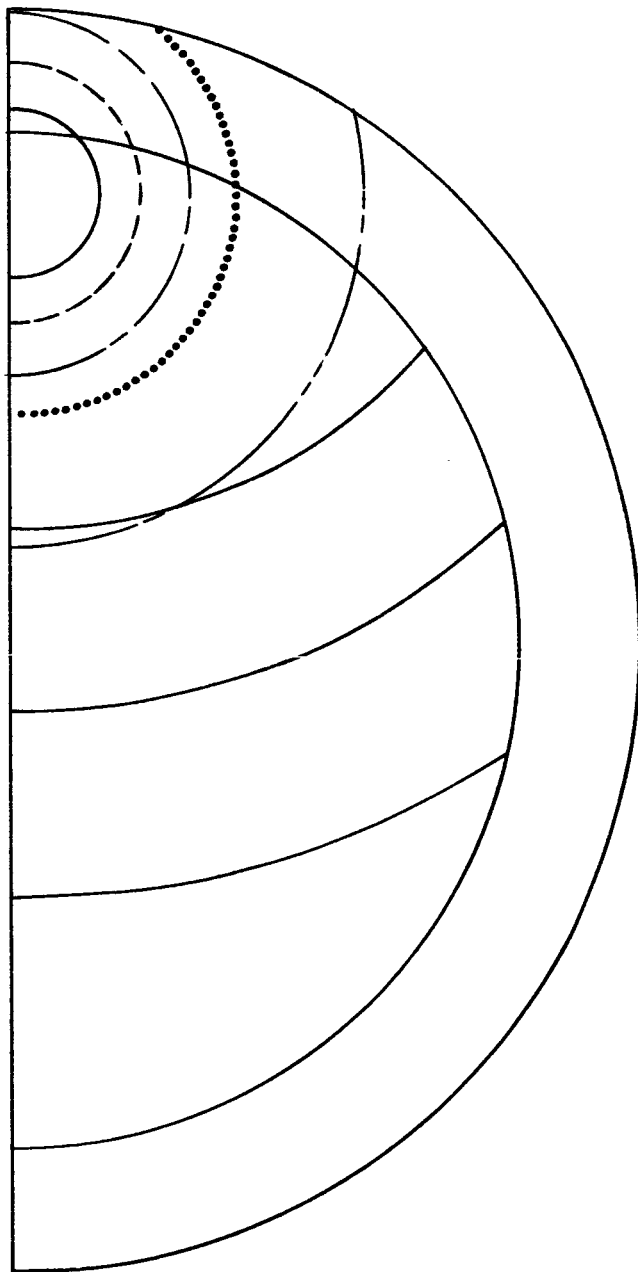


Figure II-7. Average Pressure Versus Time 35 Ft/Sec



Deflection - in.

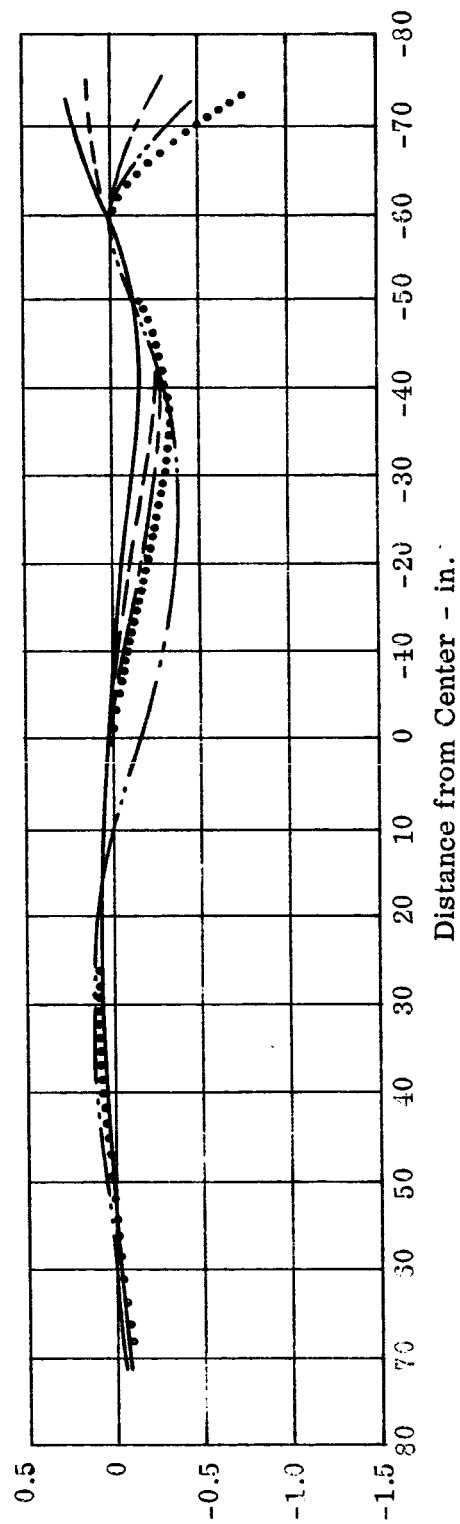


Figure II-8. Deflection Along Load Axis of Symmetry $\phi = 16.5^\circ$

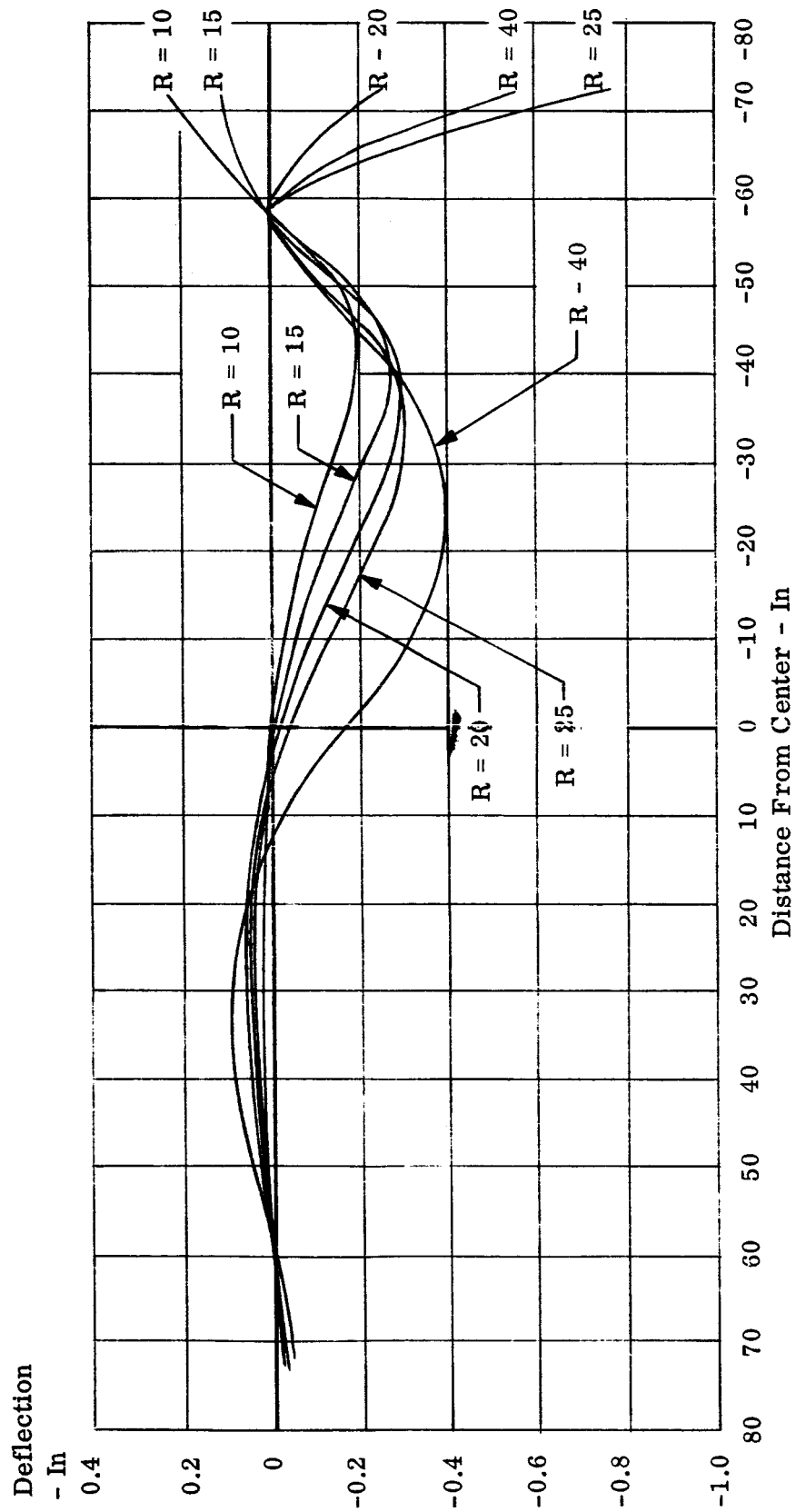


Figure II-9. Deflection Along Load Axis of Symmetry $\phi = 16.5^\circ$

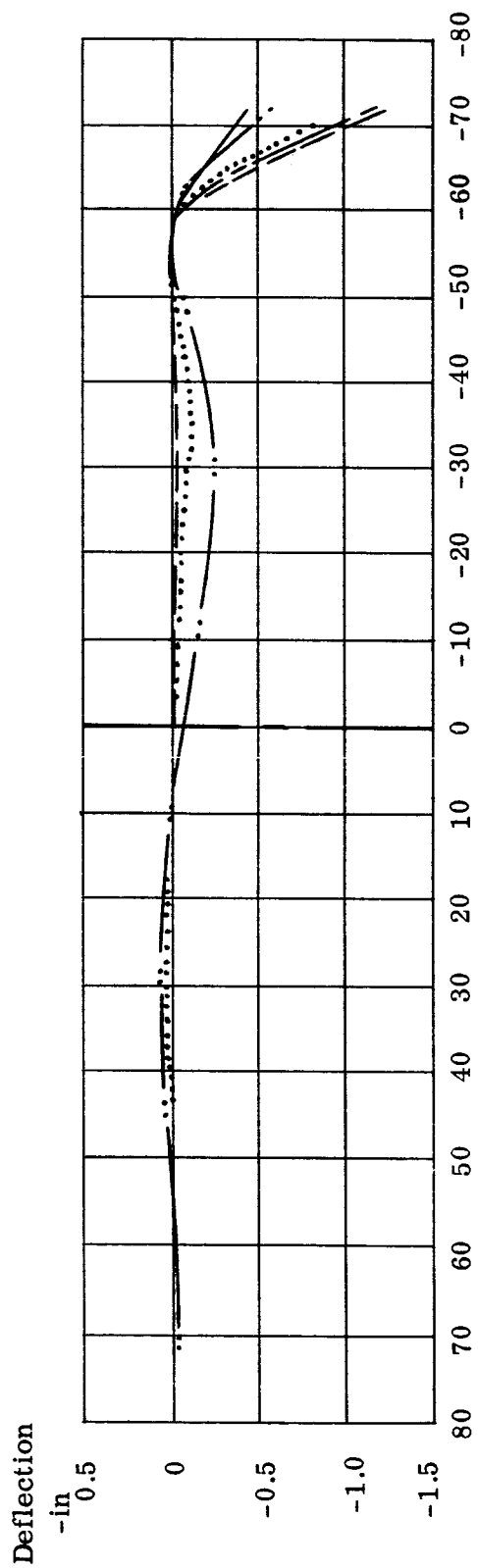
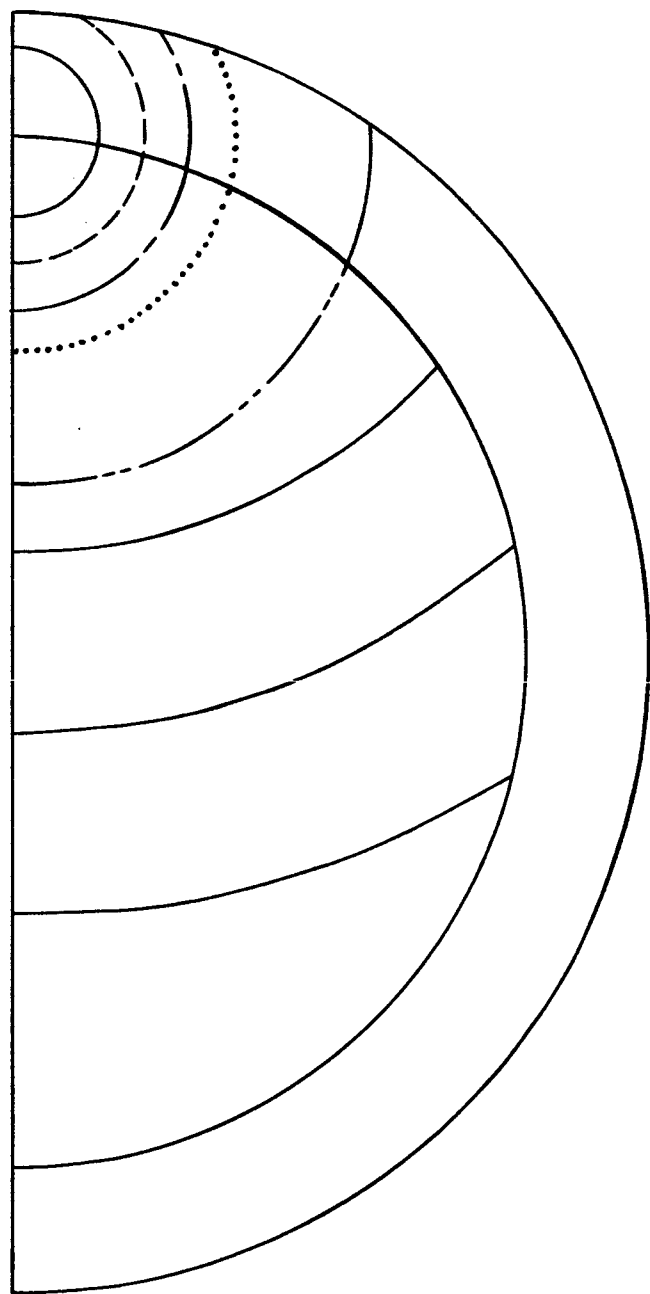


Figure II-10. Deflection Along Load Axis of Symmetry $\phi = 19.6^\circ$

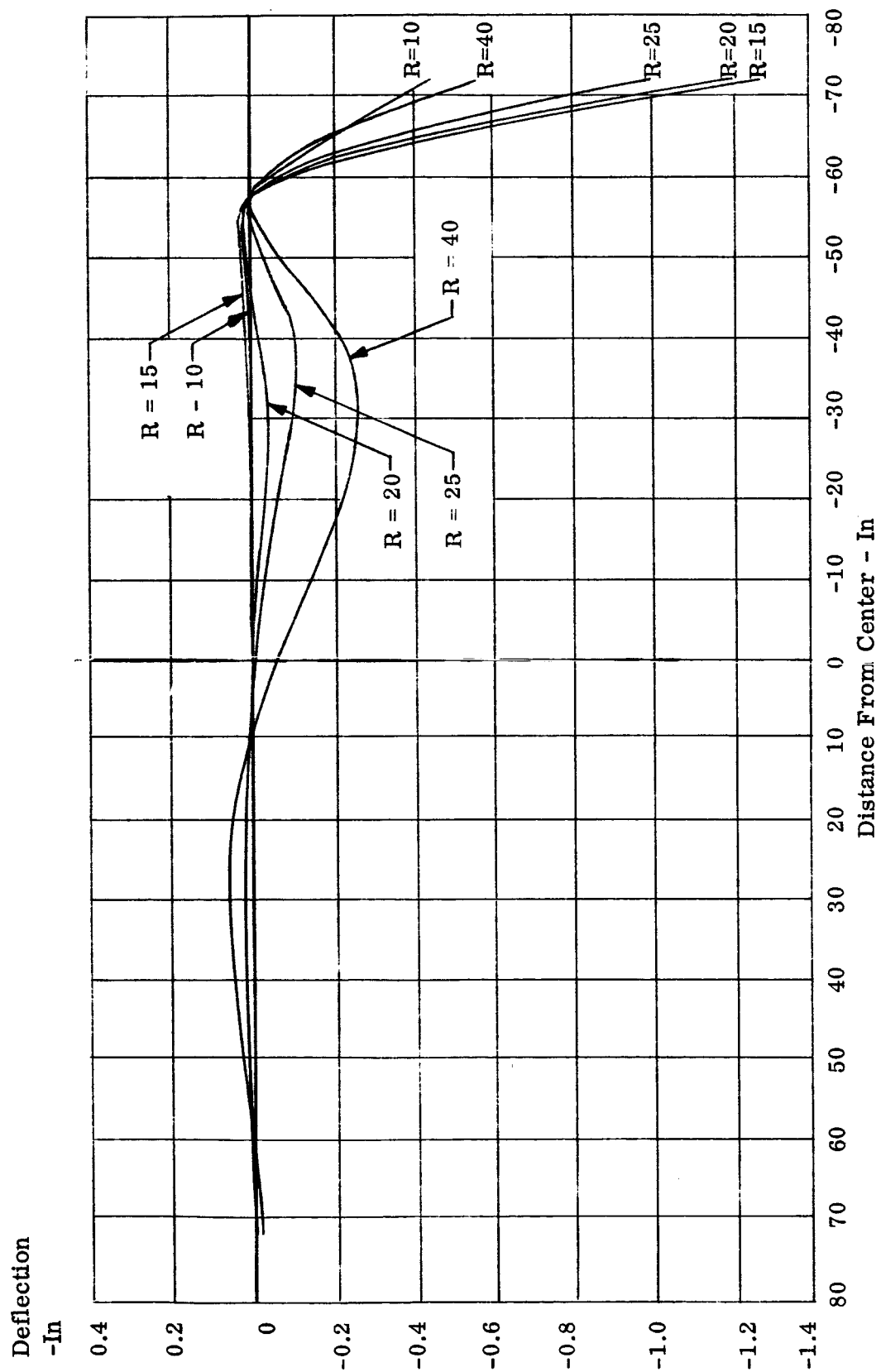


Figure II-11. Deflection Along Load Axis of Symmetry $\phi = 19.6^\circ$

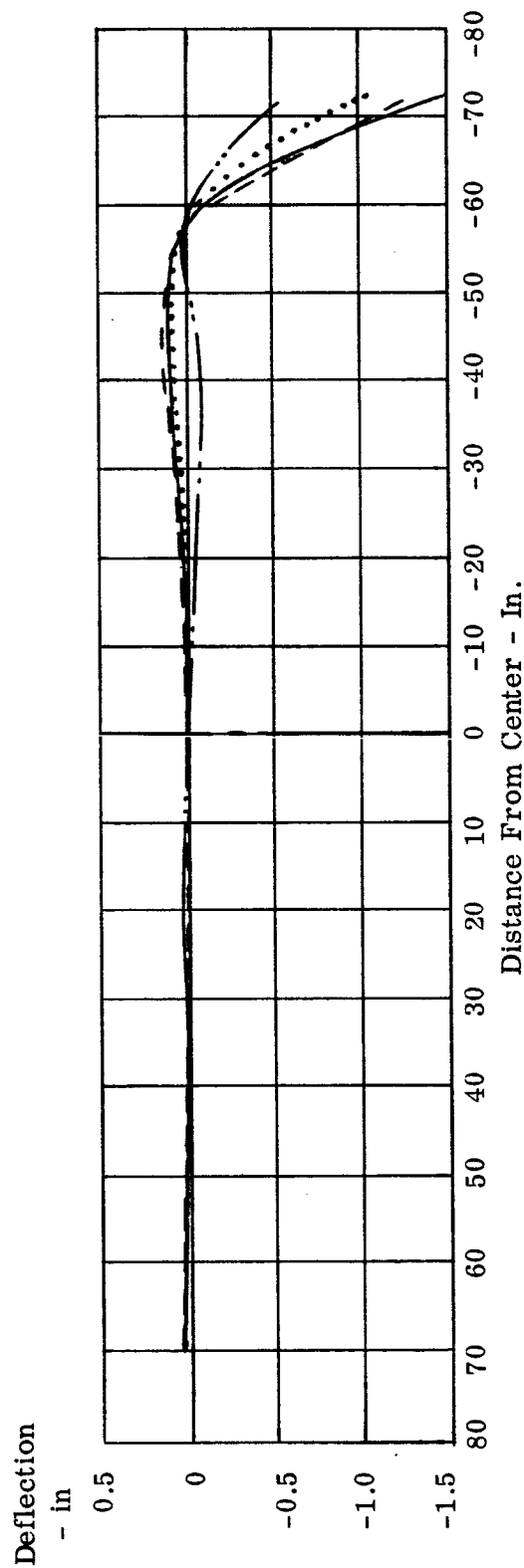
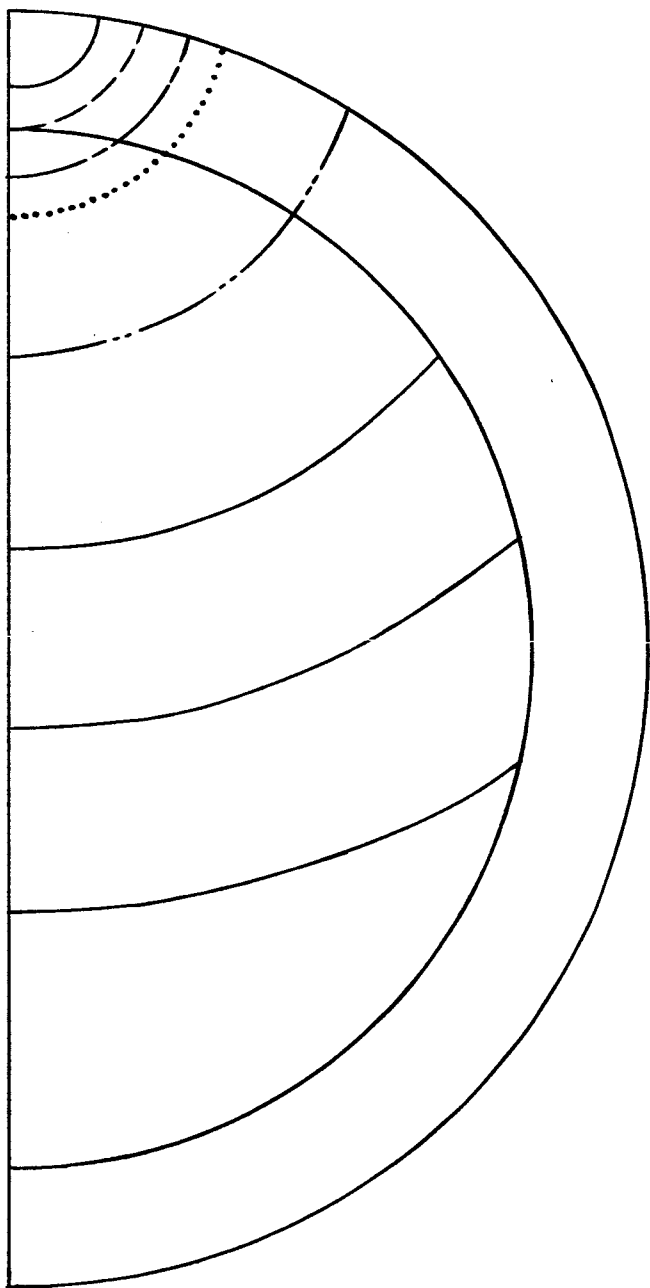


Figure II-12. Deflection Along Load Axis of Symmetry $\phi = 29.2^\circ$

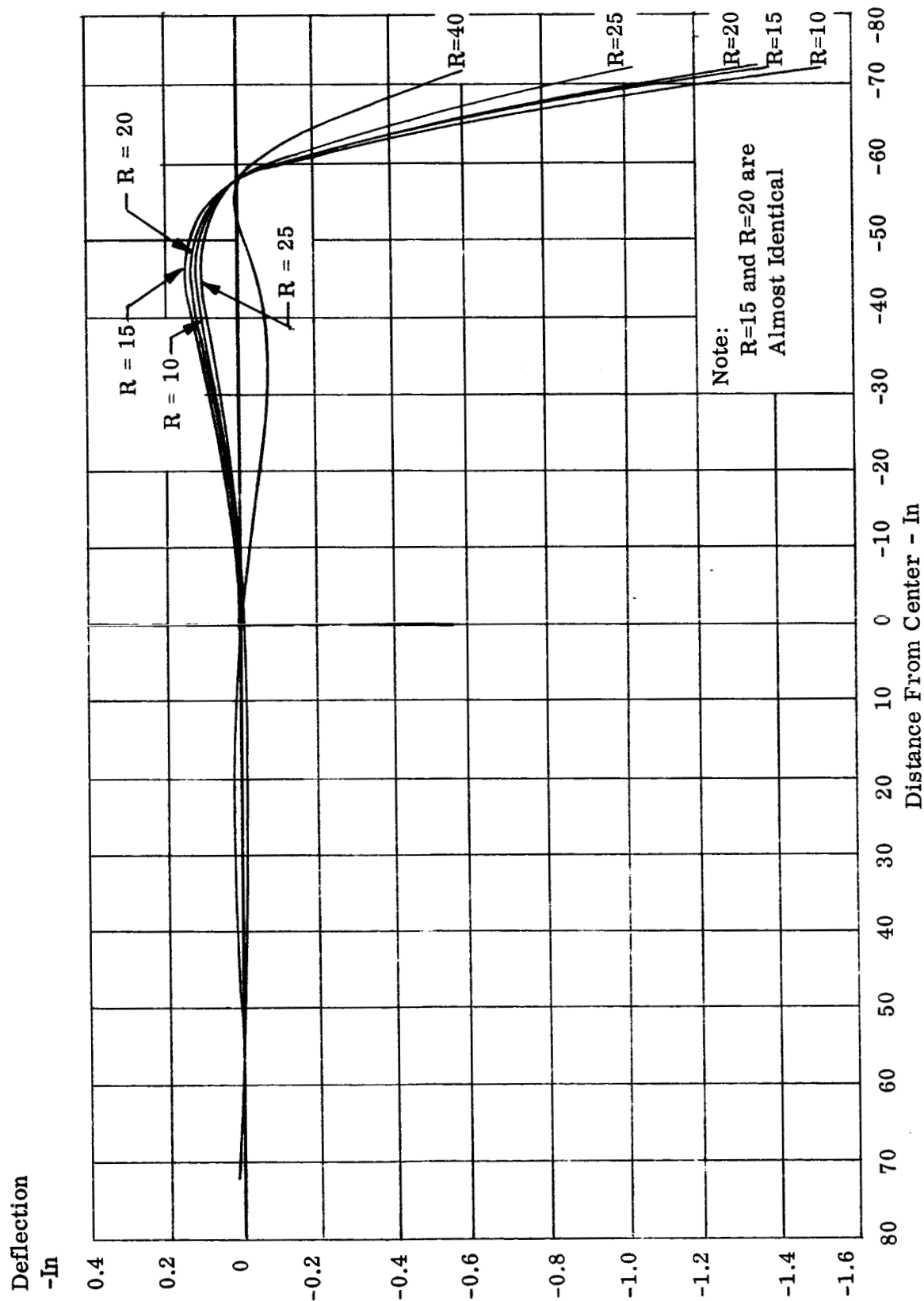


Figure II-13. Deflection Along Load Axis of Symmetry $\phi=29.2^\circ$

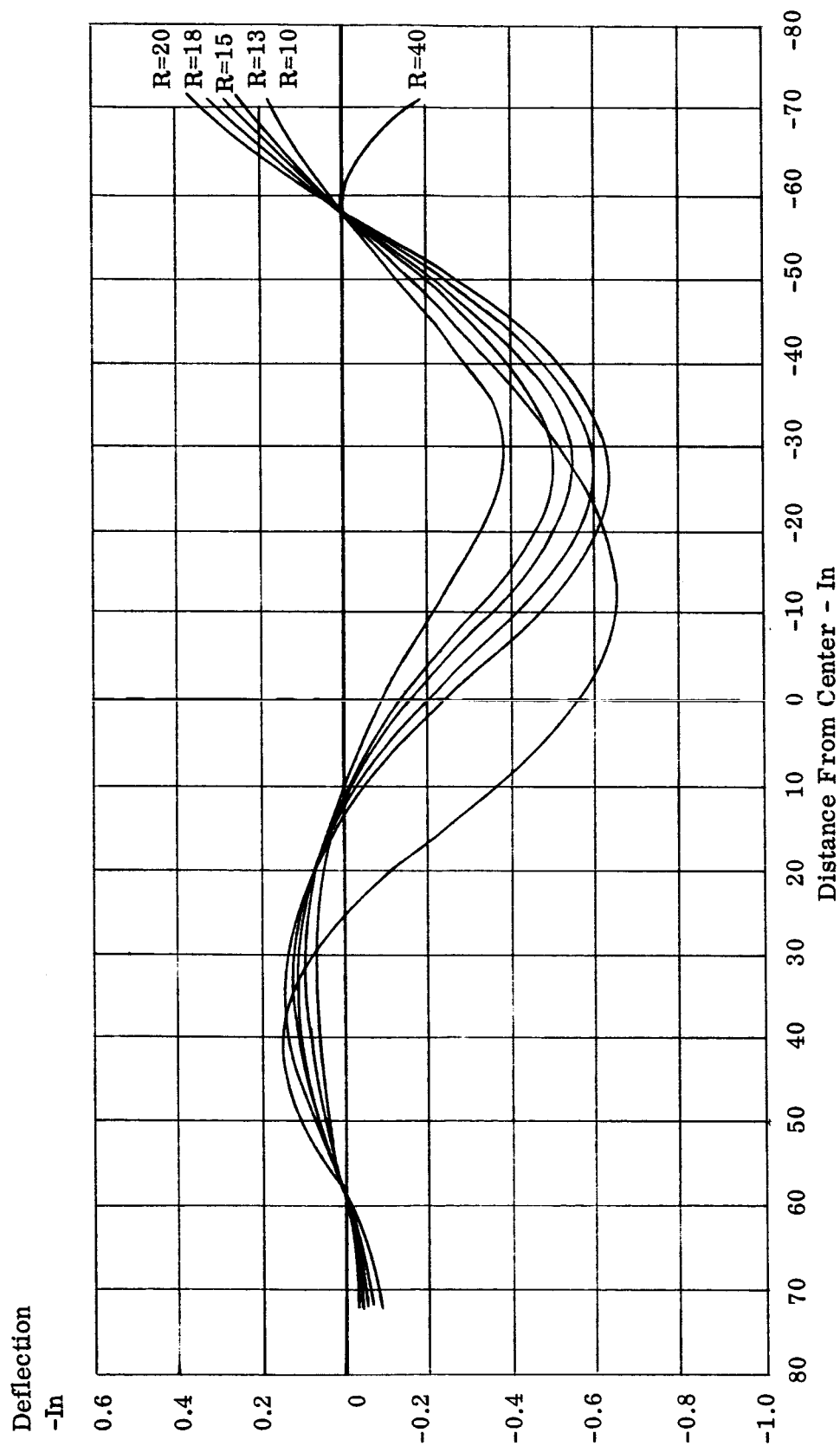


Figure II-14. Deflection Along Load Axis of Symmetry $\phi = 10$

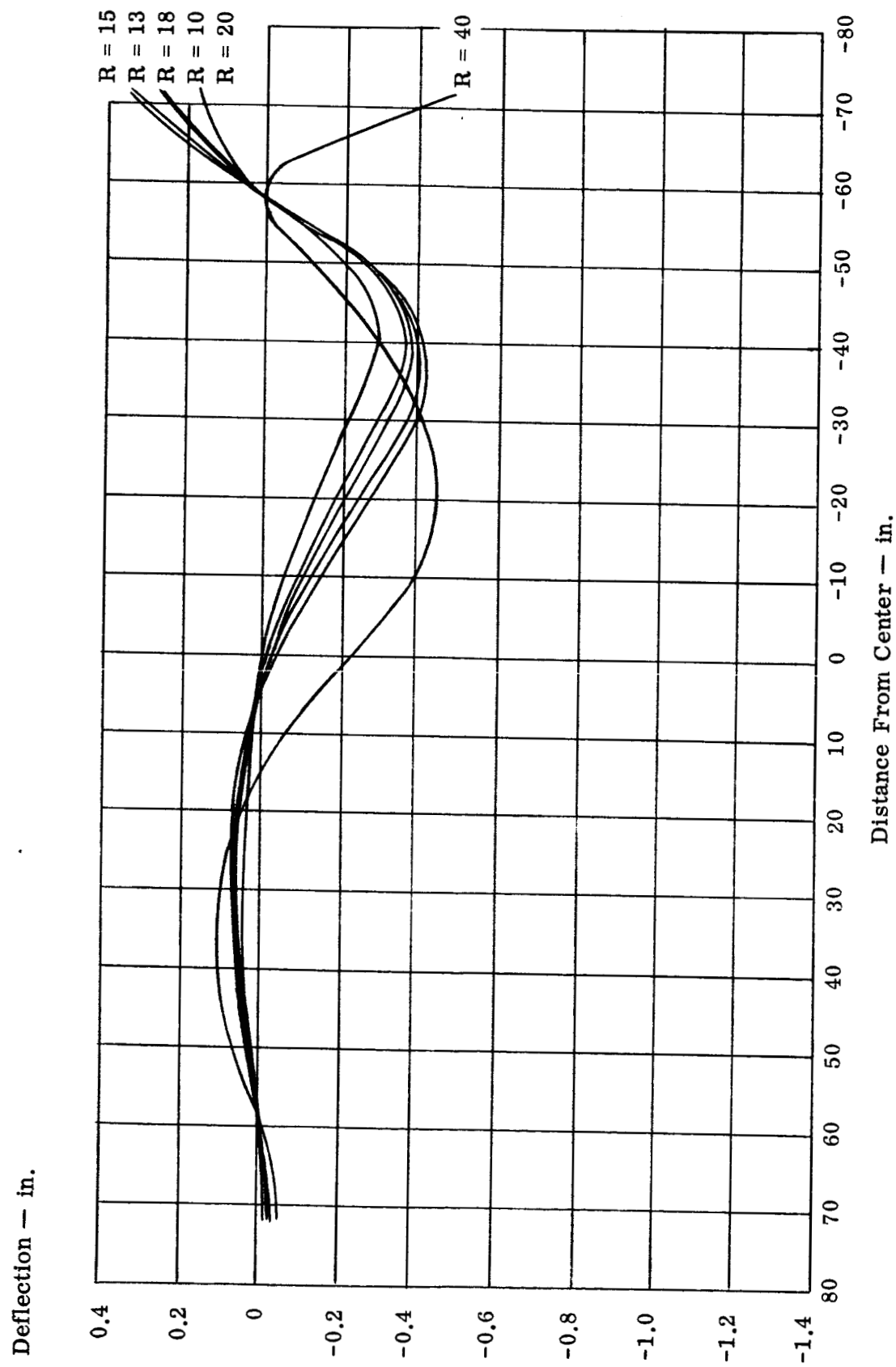


Figure II-15. Deflection Along Load Axis of Symmetry $\phi = 15^\circ$

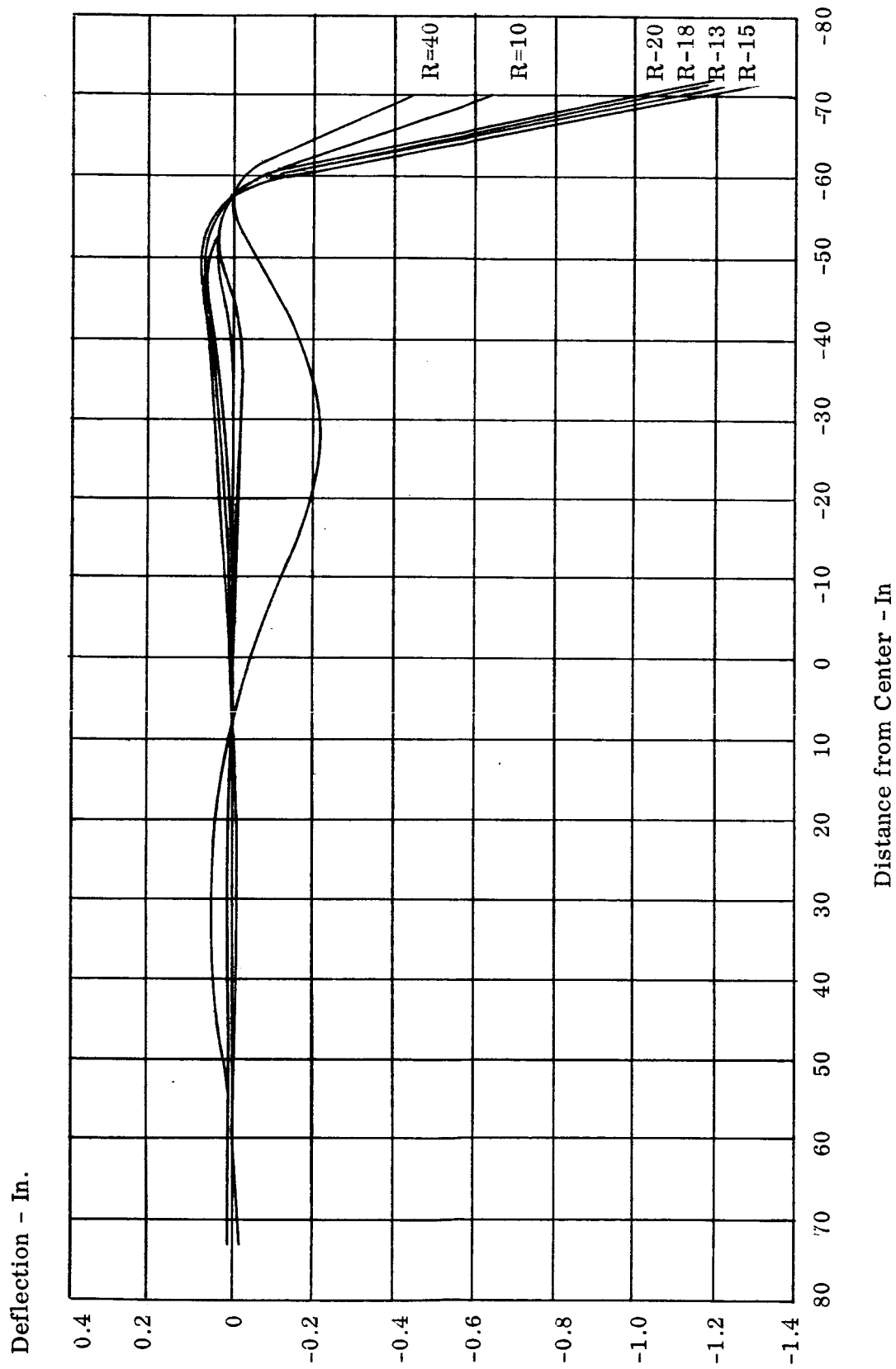


Figure II-16. Deflection Along Load Axis of Symmetry $\phi = 20^\circ$

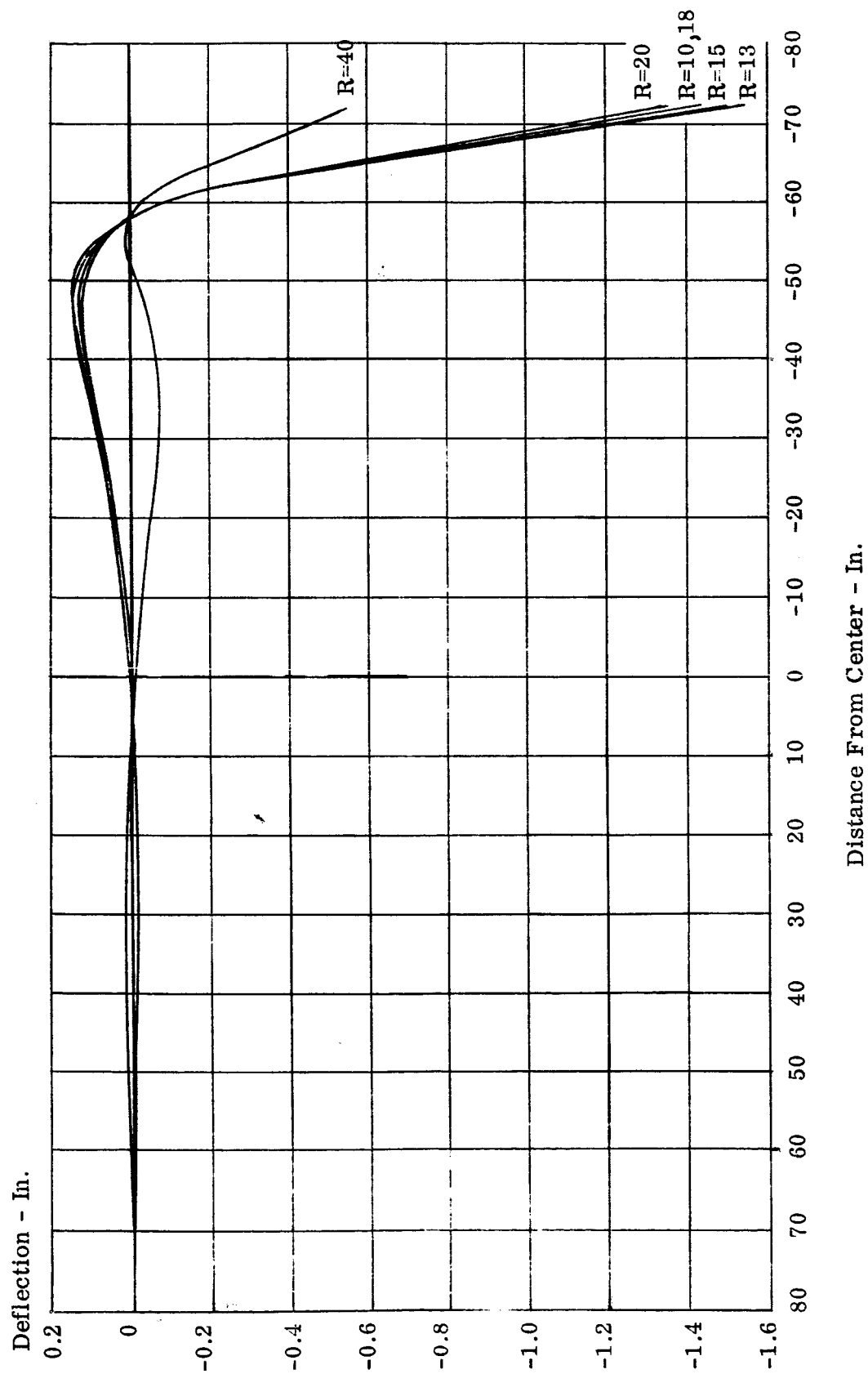


Figure II-17. Deflection Along Load Axis of Symmetry $\phi = 25^\circ$

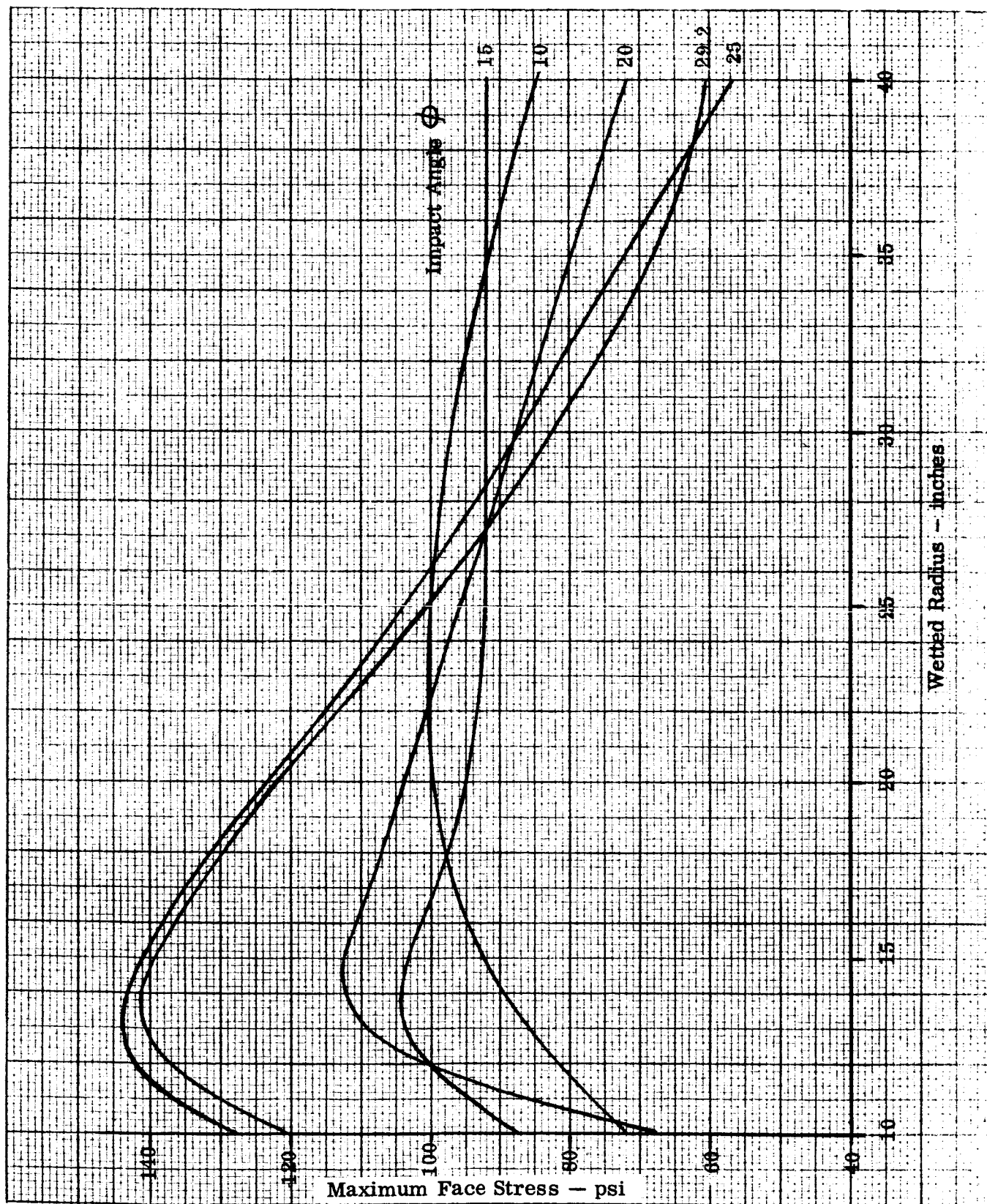


Figure II-18. Maximum Face Stress

At the bolt circle, where the largest shear stresses are recorded, two shear stresses can be computed. These correspond to the heat shield inside and outside the bolt circle respectively. Since the discrete element method generates shear forces at the centroids of the elements, it is necessary to perform an interpolation-extrapolation on the element shear forces and the edge reactions to obtain the shear force distributions at the bolt circle itself. (The edge reaction force is equal to the change in shear force of the bolt circle.)

Figures II-19, II-20, and II-21 show some typical shear stress distributions around the bolt circle. As indicated, the distance between the curves represents the bolt circle reaction.

Figure II-22 depicts the maximum shear stresses inside and outside the bolt circle respectively for the range of impact centers and radii considered.

Figure II-23 and Figure II-24 present the variation of the maximum face stresses and shear stresses with impact angle.

For cases where the load center lies within or on the bolt circle, ($\phi \leq 20^\circ$) the maximum stress is 112,000 psi and lies well within the maximum allowable stress of 150,000 psi. For cases where the load center lies outside the bolt circle ($\phi > 20^\circ$) the maximum stress is 147,000 psi. This can be regarded as pessimistic value, however, since the torus of the heat shield is assumed free to displace in the direction of the applied load. The effect of the actual support is to diminish the above predicted stress level.

In the case of the shear forces, the peak values for both inside and outside the bolt circle occur when the impact center lies on the bolt circle. The maximum values are 3050 lb/in. and 3200 lb/in. respectively. Both values, unfortunately, lie above the quoted allowable of 2600 lb/in., but test results apparently indicate that the core can sustain such shears.

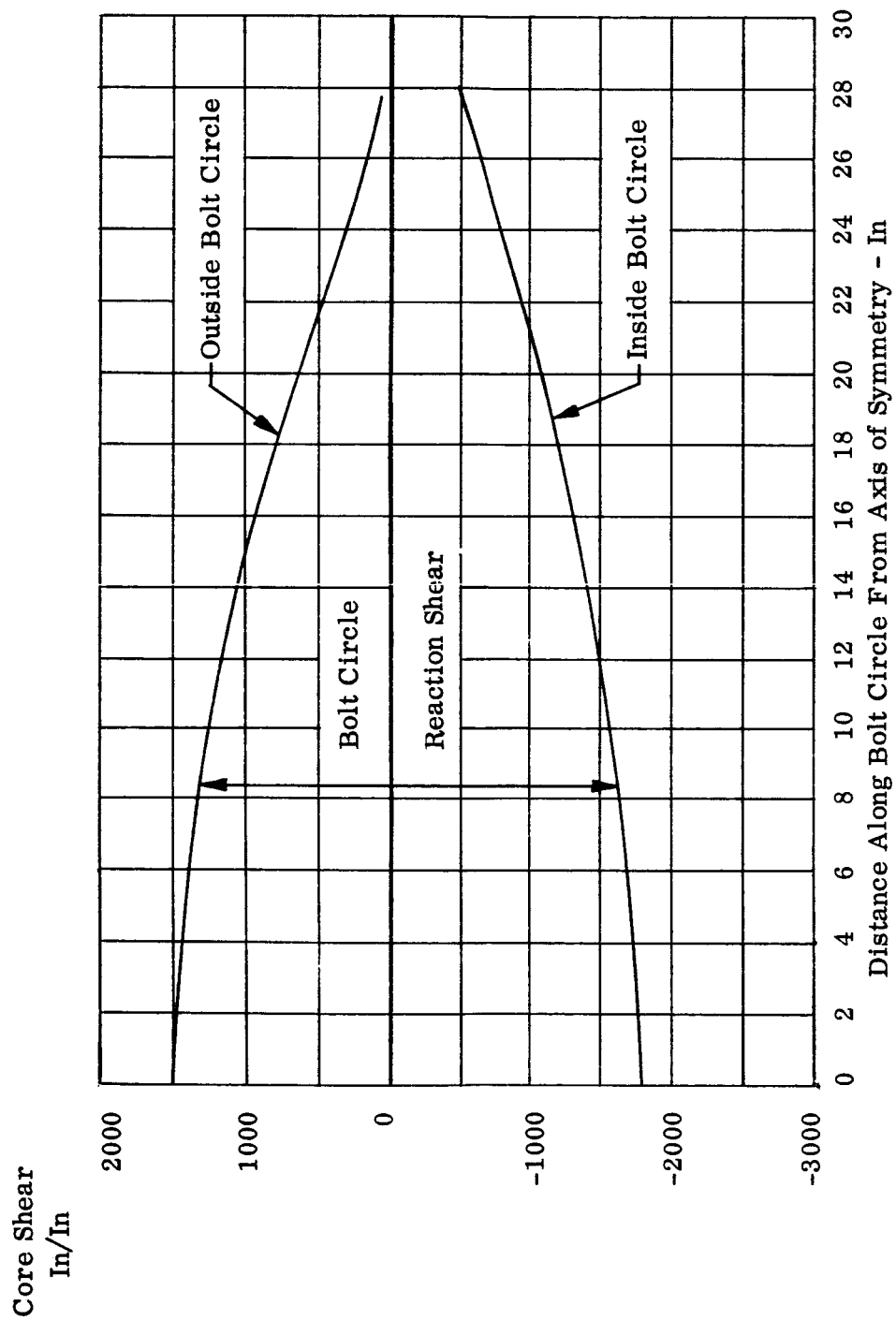


Figure II-19. Shear Along the Bolt Circle $\phi = 15^\circ$, $R = 25$ In

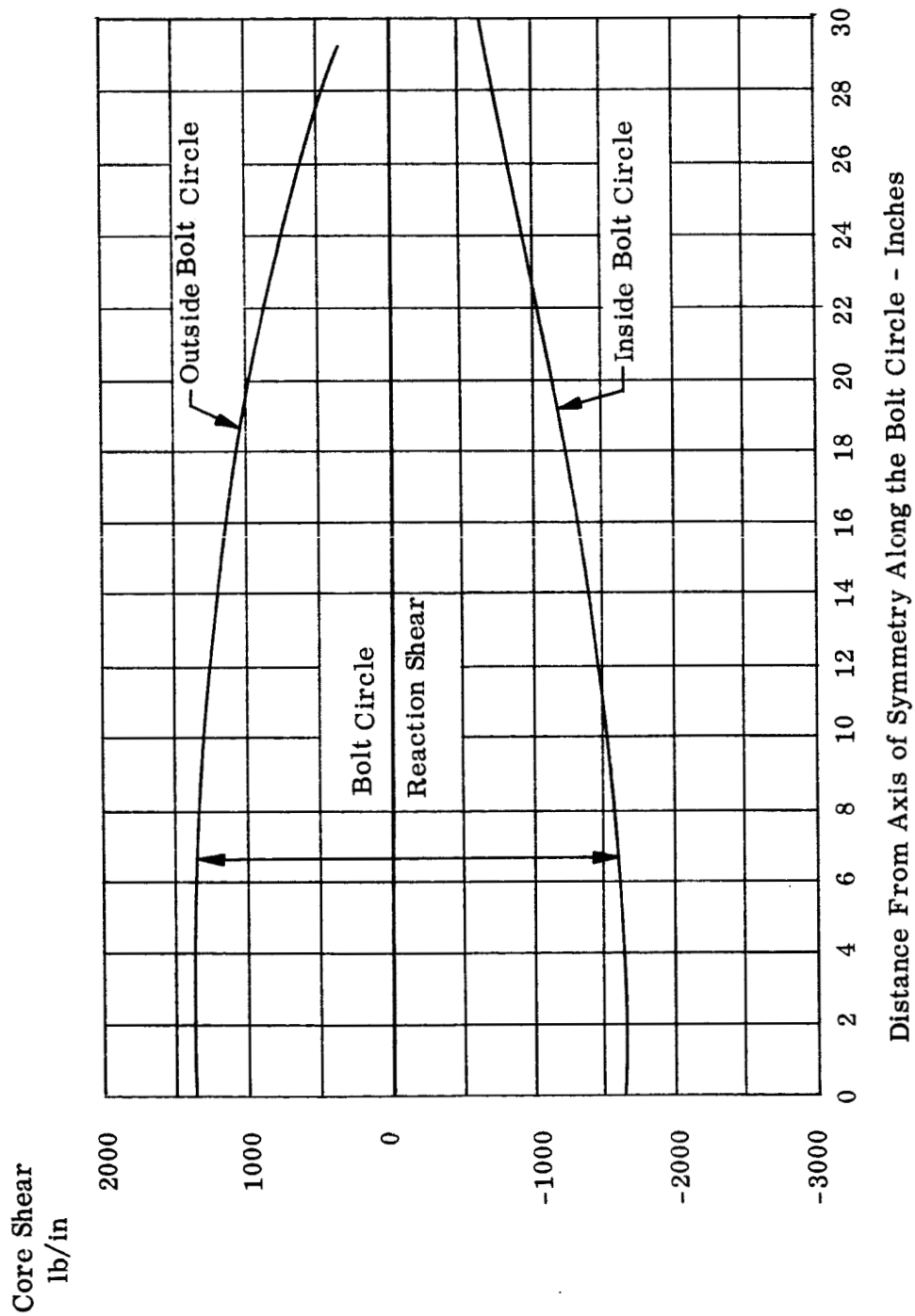


Figure II-20. Shear Along the Bolt Circle $\phi = 15^\circ$, $R = 30$ In.

Core Sheet - lb/in.

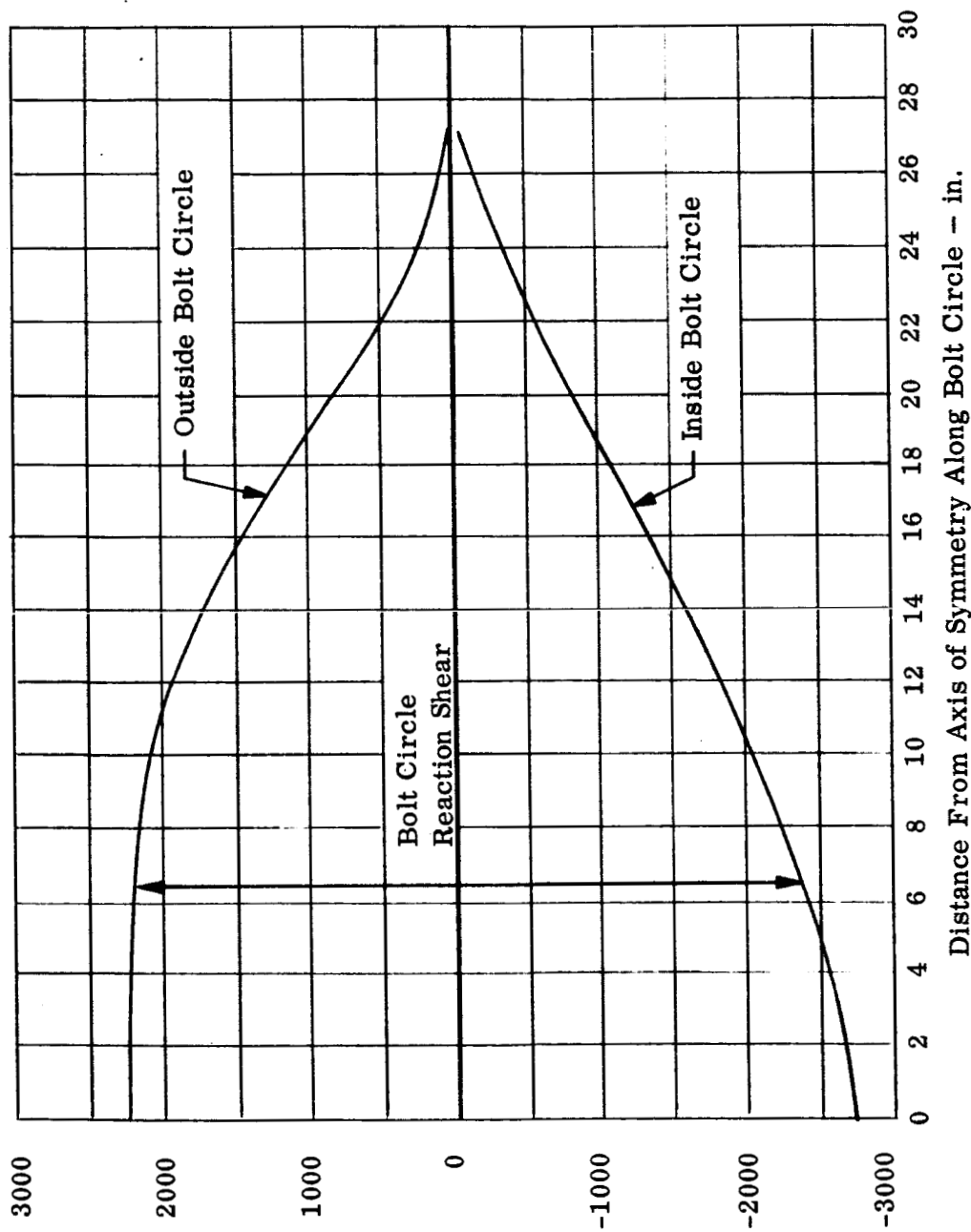


Figure II-21. Shear Along the Bolt Circle $\phi = 20^\circ$, $R = 20$ in.

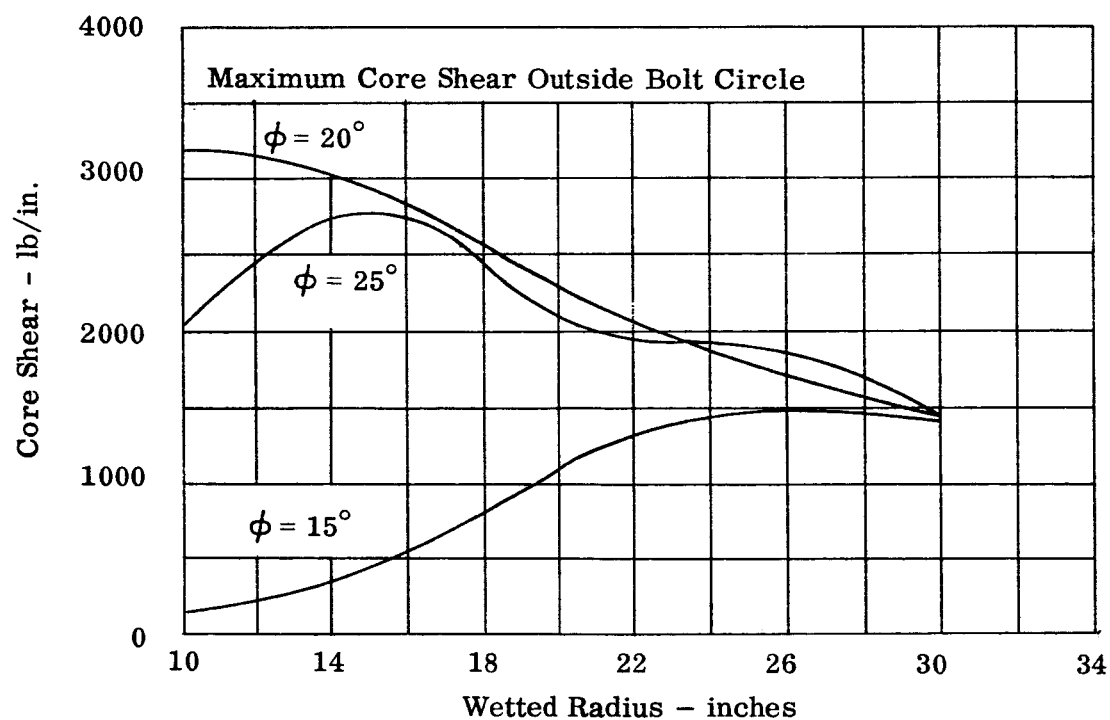
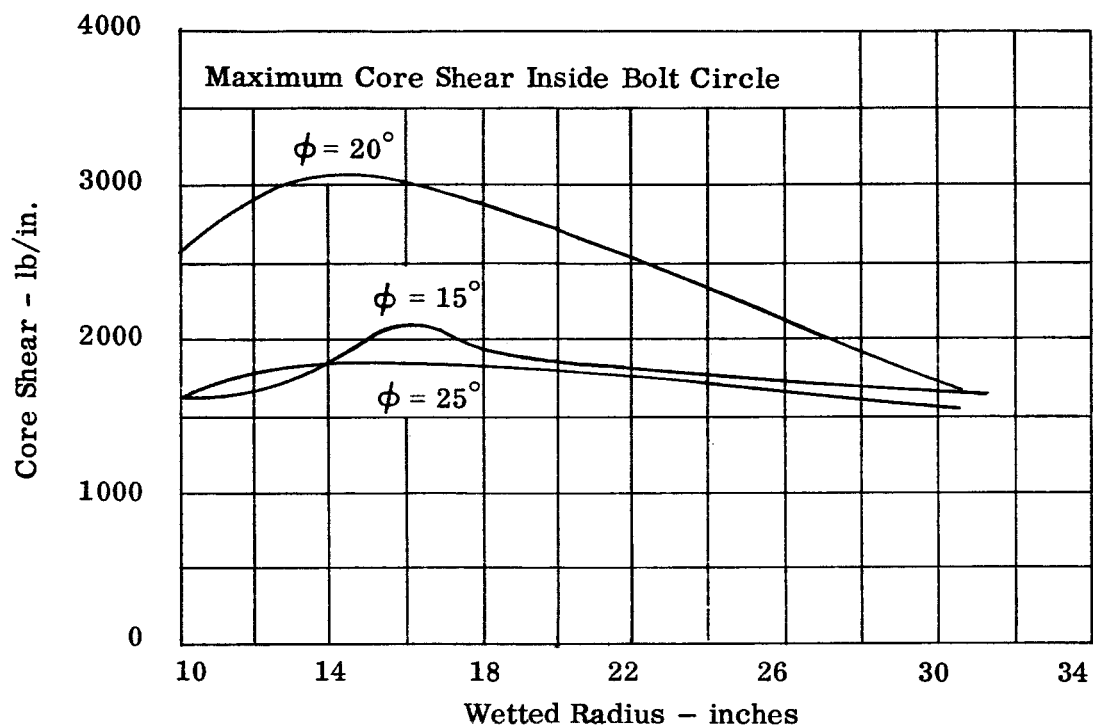


Figure II-22. Maximum Core Shear Inside and Outside the Bolt Circle

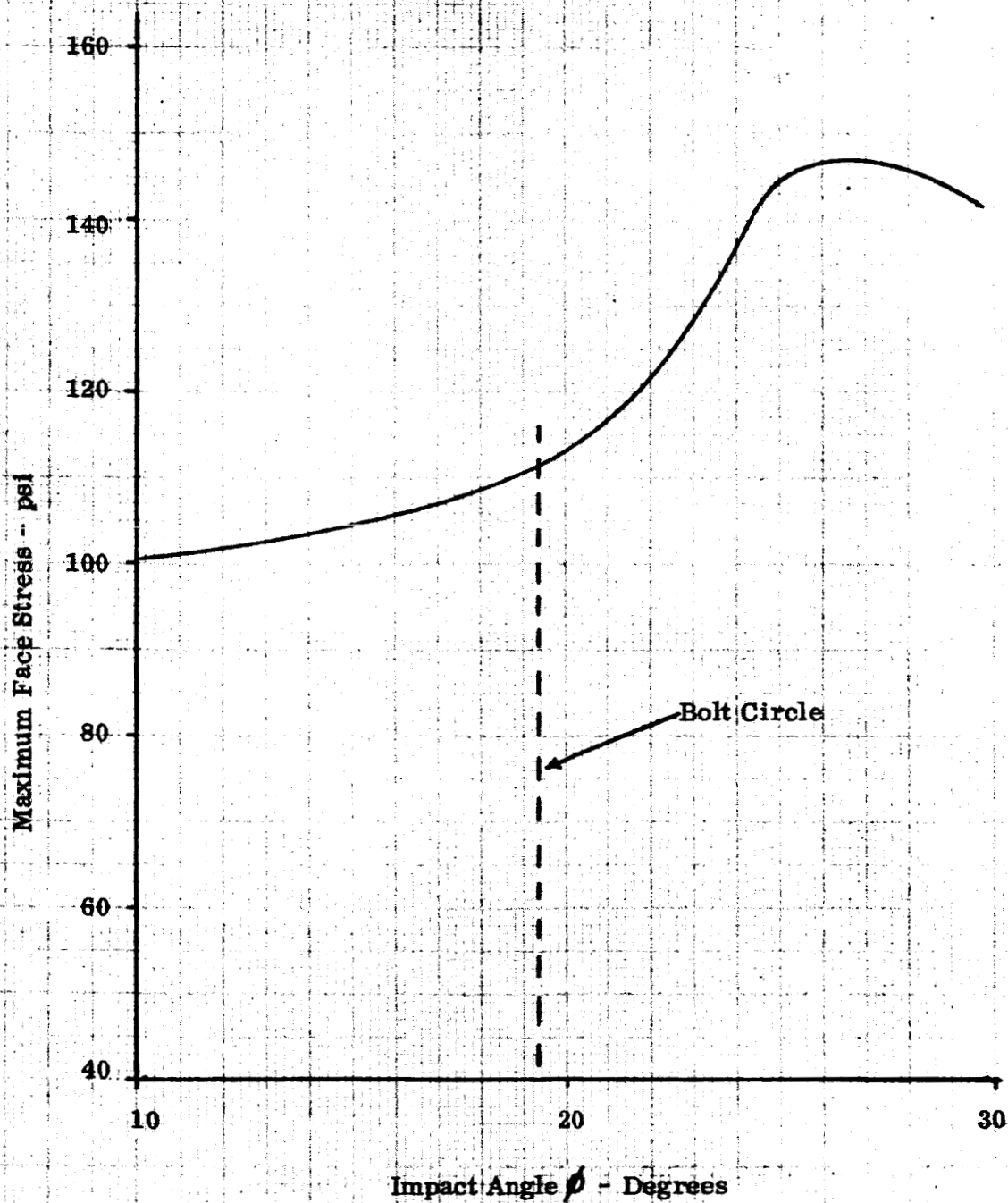


Figure II-23. Variation of Maximum Face Stress with Impact Angle

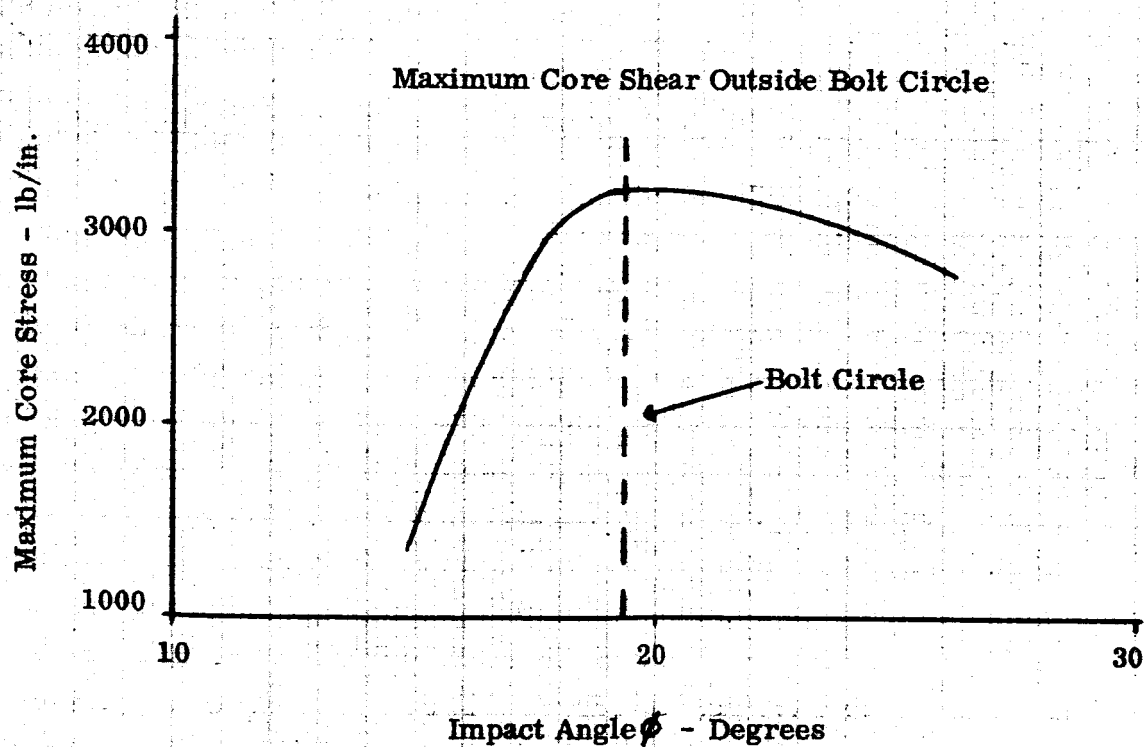
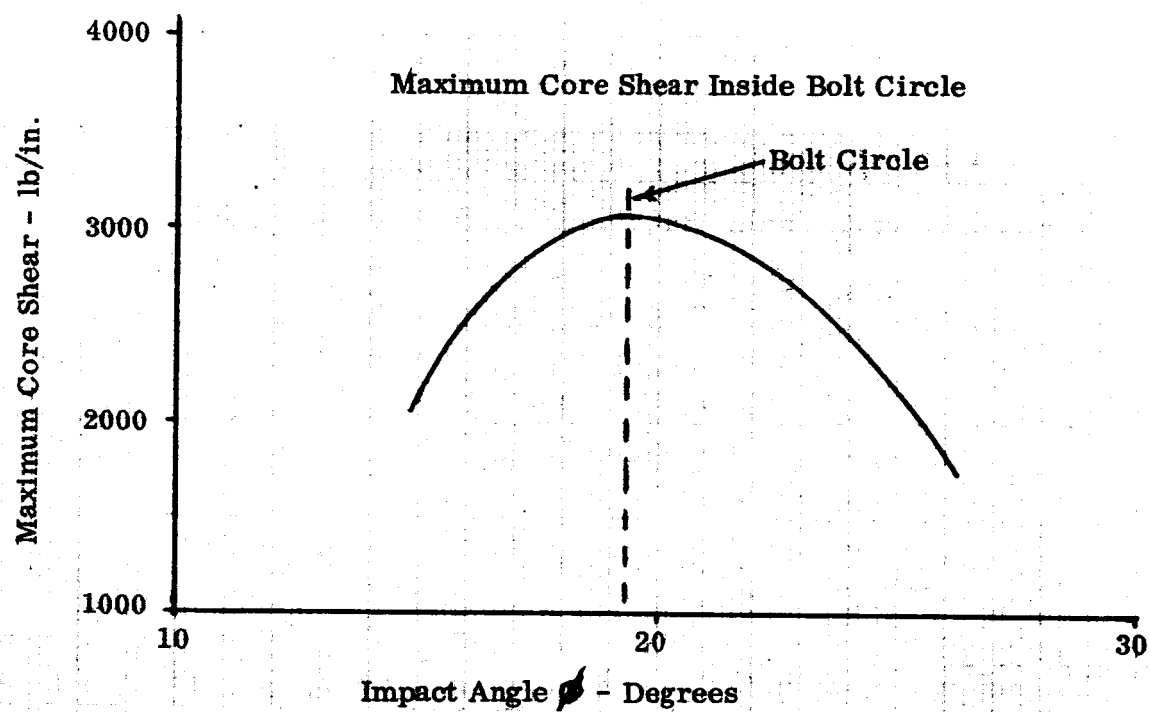


Figure II-24. Variation of Maximum Shear Stress with Impact Angle

G. THERMAL STRESS ANALYSES

Two thermal stress analyses were performed of an idealization of the heat shield in which it is assumed to possess constant face sheets of 0.008 in. The heat shield is assumed to be hinged at the bolt circle, thereby producing a restraint of displacement in the radial direction of the plane of the bolt circle. The gridwork for these analyses appears in Figure II-25. Note that the torus section ("overhang") is included in the analytical representation and that the outer periphery of the torus is hinge supported. The temperature of the structure in the stress free state is specified as 185° F. No external loads are considered in the two analyses described in this section.

The first of the two analyses performed is designated as the "thermal soak" case. In this condition, a stabilized temperature of -150° F throughout the entire structure is realized. Since the ablator and the heat shield are composed of dissimilar materials, the change in temperature produces not only thermal forces but also thermal moments.

The second case is designated as the thermal reentry condition. Here, the temperature varies over the surface of the heat shield. The outer surface of the heat shield. The outer surface of the ablator possesses a constant temperature of 1000° F. This temperature is assumed to vary across the ablator according to a parabolic law, reaching the same temperature as the skin of the sandwich on the other surface. The temperature of the sandwich is constant between the faces, but varies over the surface of the heat shield. This variation, which characterizes the temperature state, is defined by the listed node point temperatures, given in Table III-5.

A determination of thermal forces and moments was necessary for both cases. The formulas for thermal force and thermal moment, per inch, are

$$\text{Thermal Force} \quad \int_0^{d_s} E \alpha T \, dz$$

$$\text{Thermal Moment} \quad \int_0^{d_s} E \alpha T (z - z_0) \, dz$$

where

$$z_0 = \frac{\int_0^{d_s} E \alpha T z \, dz}{\int_0^{d_s} E \alpha T \, dz}$$

The temperature (T) in these equations is the temperature change from the stress free state. A temperature distribution sketch follows.

TABLE II-4
NODE POINT COORDINATES - THERMAL STRESS ANALYSIS GRID

Coordinates

	X	Y	Z		X	Y	Z
1	21.40	0	174.292	38	0	71.980	160.168
2	36.509	0	171.763	39	0	75.050	156.778
3	45.449	0	169.616	40	0	74.640	152.223
4	54.264	0	167.006	41	-8.189	19.771	174.292
5	58.038	0	165.731	42	-13.972	33.730	171.763
6	71.980	0	160.168	43	-17.392	41.989	169.616
7	75.050	0	156.778	44	-20.766	50.133	167.006
8	74.640	0	152.223	45	-22.210	53.620	165.731
9	19.771	8.189	174.292	46	-27.546	66.500	160.168
10	33.730	13.971	171.763	47	-28.720	69.337	156.778
11	41.989	17.392	169.616	48	-28.563	68.958	152.223
12	50.133	20.766	167.006	49	-15.132	15.132	174.292
13	53.620	22.210	165.731	50	-25.816	25.816	171.763
14	66.500	27.546	160.168	51	-32.137	32.137	169.616
15	69.337	28.720	156.778	52	-38.370	38.370	167.006
16	68.958	28.563	152.223	53	-41.039	41.039	165.731
17	15.132	15.132	174.292	54	-50.898	50.898	160.168
18	25.816	25.816	171.763	55	-53.068	53.069	156.778
19	32.137	32.137	169.616	56	-52.778	52.778	152.223
20	38.370	38.370	167.007	57	-19.771	8.189	174.292
21	41.039	41.039	165.731	58	-33.730	13.971	171.763
22	50.898	50.898	160.168	59	-41.989	17.392	169.616
23	53.068	53.068	156.778	60	-50.133	20.766	167.006
24	52.778	52.778	152.223	61	-53.620	22.210	165.731
25	8.189	19.771	174.292	62	-66.500	27.546	160.168
26	13.972	33.730	171.763	63	-69.337	28.720	156.778
27	17.392	41.989	169.616	64	-68.958	28.563	152.223
28	20.766	50.133	167.006	65	-21.400	0	174.292
29	27.210	53.620	165.731	66	-36.509	0	171.763
30	27.546	66.500	160.168	67	-45.449	0	169.616
31	28.720	69.337	156.778	68	-54.264	0	167.006
32	28.563	68.958	152.223	69	-58.036	0	165.731
33	0	21.400	174.292	70	-71.980	0	160.168
34	0	36.509	171.763	71	-75.050	0	156.778
35	0	45.449	169.616	72	-74.640	0	152.223
36	0	54.264	167.007	73	0	0	175.6
37	0	58.036	165.731				



TABLE II-5
REENTRY TEMPERATURES AND ABLATOR THICKNESSES

Node Point	Temperature °F	Ablator Thickness in.	Node Point	Temperature °F	Ablator Thickness in.
1	235	1.65	38	162	1.68
2	291	1.54	39	94	1.64
3	373	1.50	40	80	1.15
4	440	1.49	41	152	1.76
5	460	1.49	42	142	1.76
6	488	1.43	43	138	1.76
7	500	1.14	44	128	1.81
8	200	0.80	45	122	1.83
9	221	1.66	46	110	1.85
10	290	1.56	47	82	1.88
11	350	1.54	48	80	1.37
12	450	1.53	49	143	1.89
13	465	1.52	50	129	1.93
14	447	1.46	51	121	1.99
15	275	1.16	52	112	2.04
16	129	0.84	53	106	2.05
17	211	1.68	54	96	2.07
18	264	1.58	55	82	2.05
19	325	1.56	56	80	1.56
20	408	1.55	57	139	1.98
21	410	1.55	58	120	2.13
22	371	1.50	59	110	2.21
23	151	1.25	60	101	2.31
24	99	0.90	61	97	2.36
25	189	1.70	62	90	2.39
26	220	1.62	63	80	2.20
27	268	1.60	64	80	1.73
28	308	1.59	65	137	2.05
29	305	1.60	66	117	2.21
30	268	1.58	67	107	2.30
31	108	1.45	68	98	2.39
32	86	1.00	69	93	2.44
33	170	1.72	70	86	2.43
34	173	1.67	71	80	2.12
35	180	1.65	72	80	1.80
36	179	1.66	73	185	1.84
37	178	1.67			

TABLE II-6

ELEMENT THERMAL STRESS ANALYSIS DATA

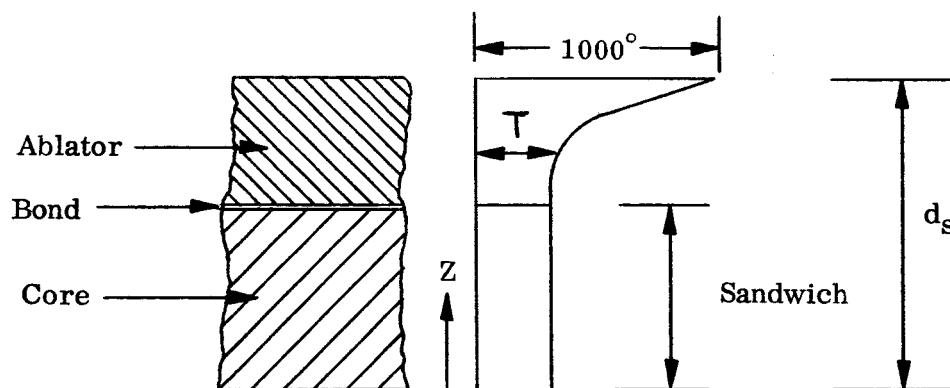
EL# Quads	Thermal Reentry			Cold Soak			M α
	Nodes	t _m	t _b	$\alpha_c (10^{-6})$	M α	t _m	
1	1, 2	0.01599	0.5931	7.7942	73.91	0.02946	10.5144
2	2, 3	0.01580	0.5885	6.9518	66.57	0.02390	10.4484
3	3, 4	0.01554	0.5835	6.9022	62.20	0.02874	10.3788
4	4, 5	0.01537	0.5789	6.6122	51.14	0.02868	10.3668
5	5, 6	0.01533	0.5777	6.3855	49.12	0.02341	10.3136
6	6, 7	0.02341	0.2680	1.5906	19.86	0.03616	9.0068
7	7, 8	0.02404	0.2680	1.7024	17.38	0.03385	8.4692
8	17,18	0.01623	0.5984	9.0518	85.79	0.02960	10.5412
9	18,19	0.01592	0.5915	7.5225	74.69	0.02911	10.4500
10	19,20	0.01507	0.5780	6.6302	64.68	0.02899	10.4264
11	20,21	0.01448	0.5686	6.4830	56.07	0.02893	10.4148
12	21,22	0.01499	0.5751	6.4948	56.41	0.02868	10.3664
13	22,23	0.02412	0.2768	1.5076	28.18	0.03653	9.0780
14	23,24	0.02486	0.2760	1.4292	23.14	0.03403	8.5640
15	17,18	0.01631	0.5994	15.242	83.77	0.02981	10.5792
16	18,19	0.01604	0.5937	8.1065	76.73	0.02424	10.4964
17	19,20	0.01529	0.5829	6.9220	72.28	0.02424	10.4692
18	20,21	0.01463	0.5732	6.7365	65.95	0.02922	10.4456
19	21,22	0.01519	0.5810	6.8742	69.77	0.02909	9.2360
20	22,23	0.02504	0.2887	1.4702	37.98	0.03735	8.7544
21	23,24	0.02573	0.2846	1.3752	26.81	0.03493	10.6276
22	33,34	0.01642	0.6016	9.5492	83.99	0.03007	10.6276
23	34,35	0.01614	0.6082	1.1745	80.50	0.02948	10.5648
24	35,36	0.1757	0.6074	-1.530	81.40	0.02965	10.5568
25	36,37	0.1618	0.5970	-1.643	81.11	0.02969	10.5568
26	37,38	0.01629	0.5990	1.8358	83.75	0.01971	10.5604
27	38,39	0.02578	0.3028	1.3441	45.76	0.03852	9.4436
28	39,40	0.02628	0.2956	1.5525	30.96	0.03624	9.0120
29	33,34	0.01686	0.6012	0.9678	93.48	0.03048	10.6996
30	34,35	0.01822	0.6194	-0.8712	90.34	0.03034	10.6740
31	35,36	0.1829	0.6201	-2.915	88.06	0.03042	10.6868
							-1759.05
							-1685.68
							-1552.04
							-1645.89
							-1608.56
							- 741.26
							- 559.96
							-1778.06
							-1712.85
							-1684.65
							-1676.49
							-1643.86
							- 878.64
							- 603.12
							-1793.33
							-1733.56
							-1717.26
							-1714.54
							-1698.24
							- 978.28
							- 704.34
							-1828.65
							-1782.46
							-1771.60
							-1770.03
							-1779.74
							-1122.21
							- 854.56
							-1882.98
							-1863.96
							-1874.82

TABLE II-6 (CONT)

EL# Quads		Thermal Reentry					Cold Soak				
		Nodes	t _m	t _b	$\alpha_c(10^{-6})$	M α	t _m	t _b	$\alpha_c(10^{-6})$	M α	
32	36,37	45,44	0.01704	0.6133	-2.770	93.54	0.03061	0.8043	10.7184	-1899.28	
33	37,38	46,45	0.01721	0.6163	-4.670	94.66	0.03073	0.3064	10.7400	-1816.24	
34	38,39	47,46	0.02641	0.3192	1.2796	55.08	0.03996	0.52505	9.6784	-1308.45	
35	39,40	48,47	0.02657	0.3083	1.1844	38.67	0.03788	0.4697	9.3124	-1052.54	
36	49,50	42,41	0.01726	0.6186	3.6375	101.60	0.03135	0.8169	10.8436	-1997.05	
37	50,51	43,42	0.01746	0.6220	4.2572	101.08	0.03157	0.8208	10.8788	-2038.91	
38	51,52	44,43	0.01766	0.6256	4.6175	98.76	0.03190	0.8263	10.9296	-2082.37	
39	52,53	45,44	0.01785	0.6289	4.9160	96.70	0.03217	0.8308	10.9720	-2105.69	
40	53,54	46,45	0.01805	0.6324	5.1432	94.96	0.03231	0.8333	10.9956	-2125.33	
41	54,55	47,46	0.01708	0.3359	1.4414	64.92	0.04159	0.5587	9.9280	-1520.92	
42	55,56	48,47	0.01695	0.3216	1.4918	49.33	0.03956	0.5089	9.5996	-1255.88	
43	49,50	58,57	0.01758	0.01758	4.1778	107.84	0.03256	0.8375	11.0348	-2115.25	
44	50,51	59,58	0.01796	0.6342	4.7205	110.32	0.03326	0.8494	11.1276	-2219.57	
45	51,52	60,59	0.01825	0.6399	5.0395	110.88	0.03385	0.8595	11.2220	-2340.29	
46	52,53	61,60	0.01847	0.6448	5.2335	110.48	0.03428	0.8667	11.2808	-2385.27	
47	53,54	62,61	0.01867	0.6486	5.4135	108.07	0.03450	0.8706	11.3108	-2415.65	
48	54,55	63,62	0.02755	0.3554	1.4548	81.48	0.04336	0.6015	10.1736	-1769.90	
49	55,56	64,63	0.02726	0.3355	1.4822	63.32	0.04096	0.5430	9.8204	-1440.22	
50	65,66	58,57	0.01781	0.6234	4.3640	112.66	0.03348	0.8533	11.1720	-2237.42	
51	66,67	59,58	0.01828	0.6424	4.6877	112.60	0.03446	0.8700	11.3108	-2366.77	
52	67,68	60,59	0.01862	0.6499	4.9667	126.92	0.03520	0.8825	11.4092	-2507.42	
53	68,69	61,60	0.01890	0.6567	5.3502	122.98	0.03580	0.8926	11.4856	-2429.45	
54	69,70	63,62	0.01913	0.6608	5.5118	119.58	0.03604	0.8968	11.5168	-2619.19	
55	70,71	63,62	0.02784	0.3670	1.4580	91.79	0.04424	0.6247	10.2900	-1858.66	
56	71,72	64,63	0.01743	0.02743	1.4772	70.96	0.04.59	0.5606	9.9208	-1533.40	

TABLE II-6 (CONT)

EL#	Thermal Reentry					Cold Soak			
	Nodes	t _m	t _b	$\alpha_c (10^{-6})$	M α	t _m	t _b	$\alpha_c (10^{-6})$	M α
Triangles									
1	73, 1, 9	0.016306	0.6016	8.6959	92.267	0.03040	0.8007	10.6816	-1871.18
2	73, 17, 9	0.016418	0.6043	9.8300	91.670	0.03048	0.8021	10.6964	-1882.05
3	73, 17, 25	0.016470	0.6050	21.385	95.440	0.03059	0.8040	10.7160	-1896.53
4	73, 33, 25	0.016536	0.6058	16.0075	92.667	0.03070	0.8058	10.7352	-1911.01
5	73, 33, 41	0.016742	0.6094	1.2680	95.840	0.03086	0.8087	10.7636	-1932.74
6	73, 49, 41	0.016956	0.6134	3.2352	103.793	0.03130	0.8161	10.7816	-1990.69
7	73, 49, 57	0.017028	0.6172	3.7979	103.533	0.03190	0.8264	10.9340	-2067.67
8	73, 65, 57	0.017172	0.6198	3.9819	105.460	0.03237	0.8343	11.0052	-2132.89



The dissimilarity of materials on the cross-section presents a problem in the determination of the proper membrane and flexural stiffnesses for the plate elements. Actually program input requires the plate thickness as the basic parameter with, a single modulus of elasticity and coefficient of thermal expansion pertinent to all determinations. Here, the modulus of elasticity was chosen to be constant at $E_C = 30 \times 10^6$, and the other parameters were derived as follows:

In evaluating the foregoing integrals, the appropriate temperatures, ablator thicknesses, etc., are utilized for each node point. For example, the values obtained at the crown (node point 73) for both analyses are:

	Cold Soak	Thermal Reentry
K_{xy}	$0.94224 (10^6)$	$0.49642 (10^6)$
K_z	$0.262616 (10^9)$	$0.108068 (10^9)$
F_T	-3426.24	55.72
M	-1503.90	101.06
T	-150.0°F	+185.0°F
T_a	1.84 in.	1.84 in.

Using these parameters, equivalent plate thicknesses are calculated. From the determined thermal force, an equivalent coefficient of thermal expansion (α_c) was then derived; retaining the actual temperature difference from the stress free state (ΔT). For node point 73 the equivalent values are:

	Cold Soak	Thermal Reentry
t_m	0.03141	0.01655
t_b	0.8179	0.6084
α_c	$0.2714 (10^{-8})$	$0.1121 (10^{-8})$
M_α	-1503.9	101.06
ΔT	-335°F	1°F

With these equivalent section and material properties, the general purpose program then computes the correct stiffness and thermal forces.

Results of the thermal analyses appear in Figure II-26 and Table II-7 . The figures illustrate the variation of displacement along the axis of symmetry. The specific values of node point displacements upon which these representations are based are given in Table II-7 , as are the displacements at other selected points on the heat shield.

Figures II-27 to II-31 present the variation of meridional and circumferential thermal stresses in the heat shield along the axis of symmetry.

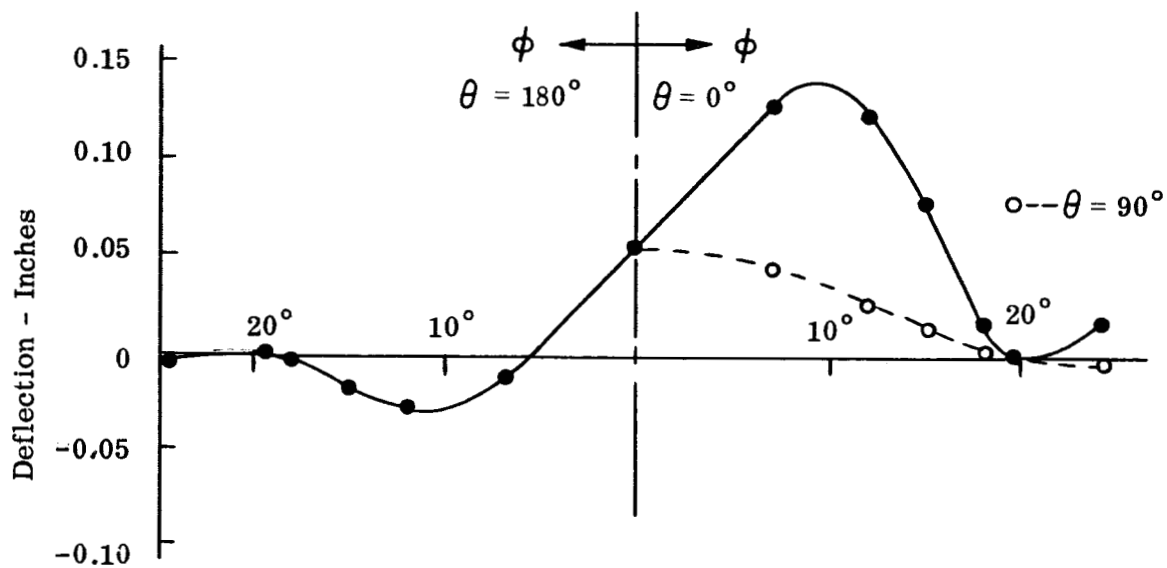
In Figures II-27 to II-30 the stresses in the upper and lower faces of the sandwich are shown for the thermal reentry and cold soak conditions. The peak stress of 122000 psi occurs in the upper face near the bolt circle during the cold soak. This stress, although high, is acceptable.

For the ablator the stress in the upper edge for the cold soak condition (Figure II-31) reveals that the maximum stress is 1050 psi (tensile). This is well above the maximum strength of the ablator material (approximately 600 psi).

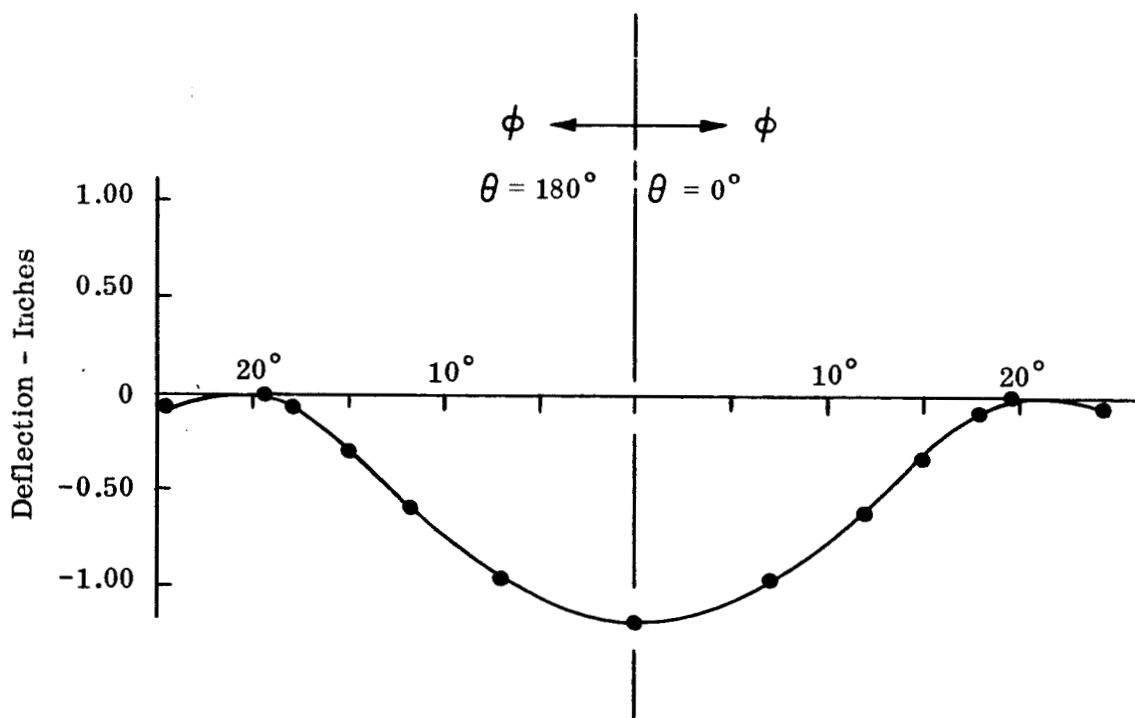
However, in evaluating these results, especially the above ablator stress, the entire thermal stress analysis must be carefully examined. In particular the boundary conditions must be considered. At the bolt circle, it has been assumed that all translational movement was completely restrained. In actual practice, the heat shield is attached to the (non-rigid) internal cabin structure by supports which also exhibit some degree of flexibility. While this assumption may be satisfactory for conditions in which the loading is principally normal to the surface of the shell, in the thermal cases, the radial expansive forces will probably cause appreciable movement at the bolt circle with consequent reduction of the stresses quoted above.

In addition, no account has been taken in the analysis of the built-in thermal stresses which exist in the heat shield. These arise from the fact that although the heat shield zero stress temperature is taken as 185°F (the temperature at which the ablator is attached), the assembly of the complete heatshield to the support structure actually occurs at around 80°F

The thermal stresses obtained above may be regarded as having been derived by a realistic approach to an unrealistic problem. In order to obtain more realistic results it would be necessary to include the inner cabin structure in the analysis. To do this would, in turn, increase the magnitude and complexity of the problem well beyond the limits of the current contract and cannot therefore be considered at present.



a. Thermal Reentry



b. Thermal Soak

Figure II-26. Thermal Displacements

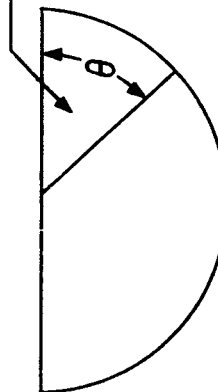
TABLE II-7

TABLE DISPLACEMENT NORMAL TO SURFACE - THERMAL CASES

Thermal Re-entry				Cold Soak			
θ ϕ	0°	90°	180°	θ ϕ	0°	90°	180°
0°	0.059	0.059	0.059	0°	-1.1829	-1.1829	-1.1829
7°	0.129	0.044	-0.013	7°	-0.9621	-0.9619	-0.9580
12°	0.125	0.025	-0.029	12°	-0.5972	-0.5931	-0.5830
15°	0.078	0.014	-0.019	15°	-0.3105	-0.3055	-0.2971
18°	0.017	0.003	-0.004	18°	-0.0591	-0.0568	-0.0537
19.3°	0.0	0.0	0.0	19.3°	0.0	0.0	0.0
24.2°	0.020	-0.002	-0.007	24.2°	-0.0545	-0.0594	-0.0668

Values Tubulated are Displacements in inches

{ High Temperatures
Thin Ablator



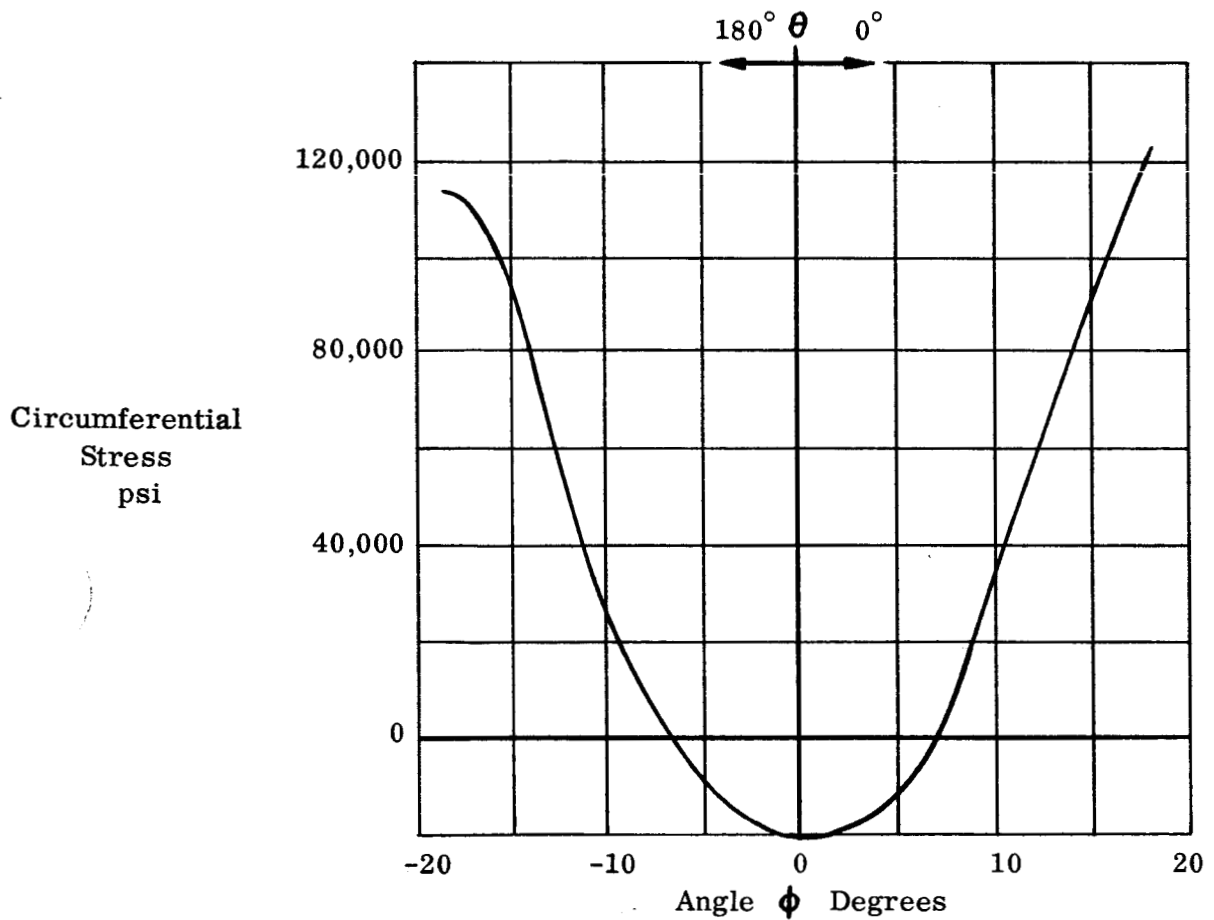
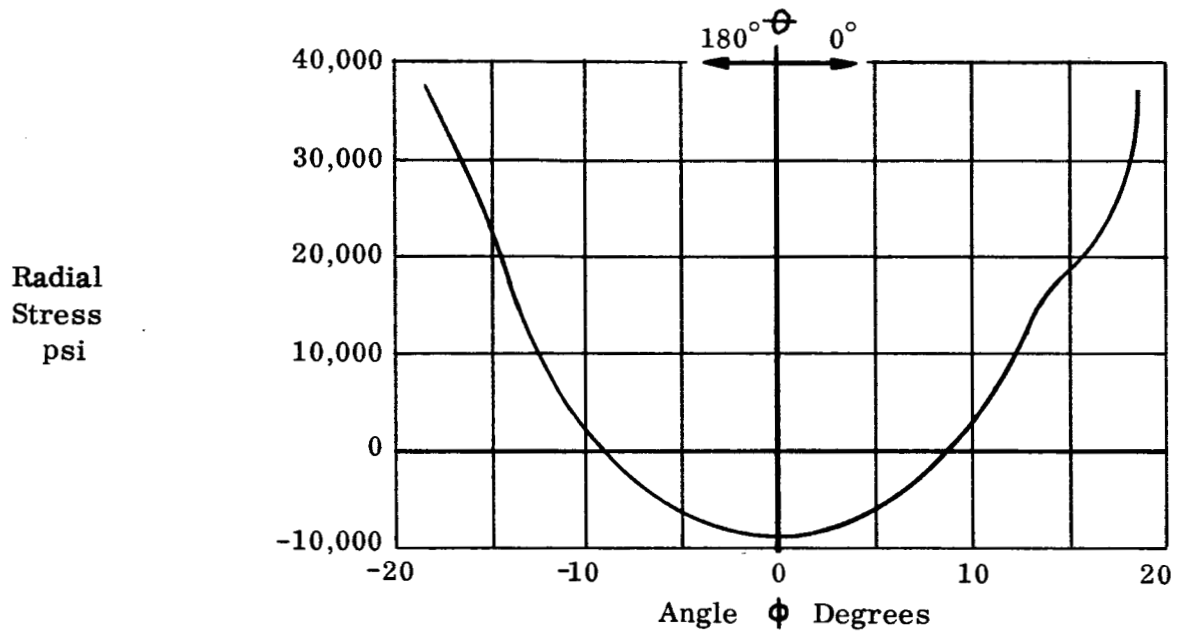
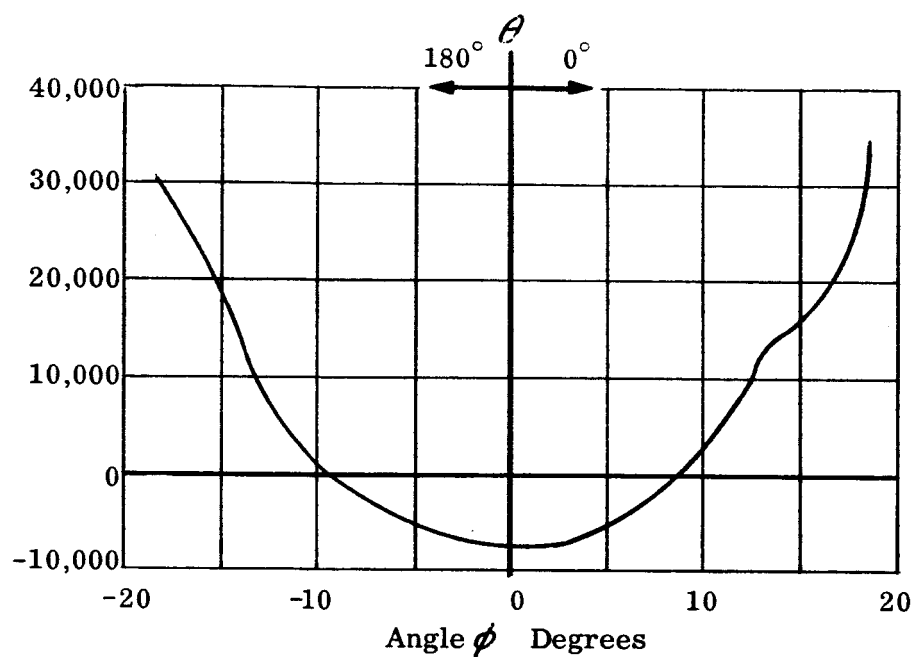


Figure II-27. Thermal Stresses in Upper Sandwich Face
Cold Soak Condition

Radial
Stress
psi



Circumferential
Stress
psi

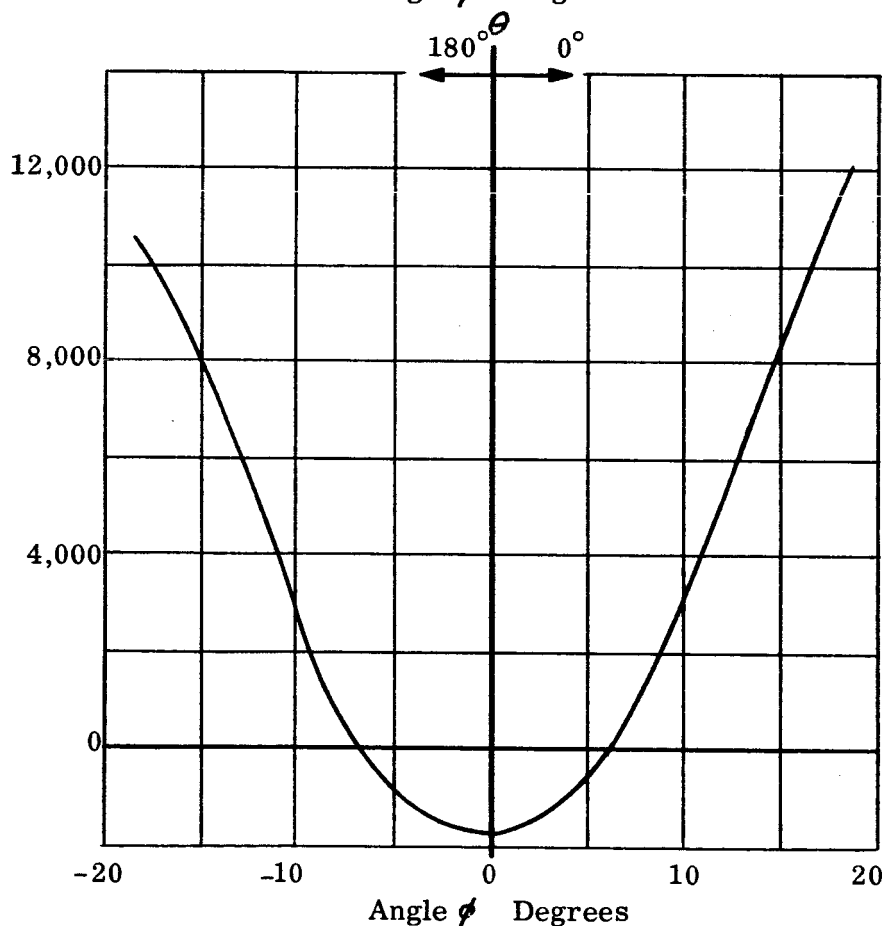


Figure II-28. Thermal Stresses In Lower Sandwich Face Cold Soak Thermal Condition

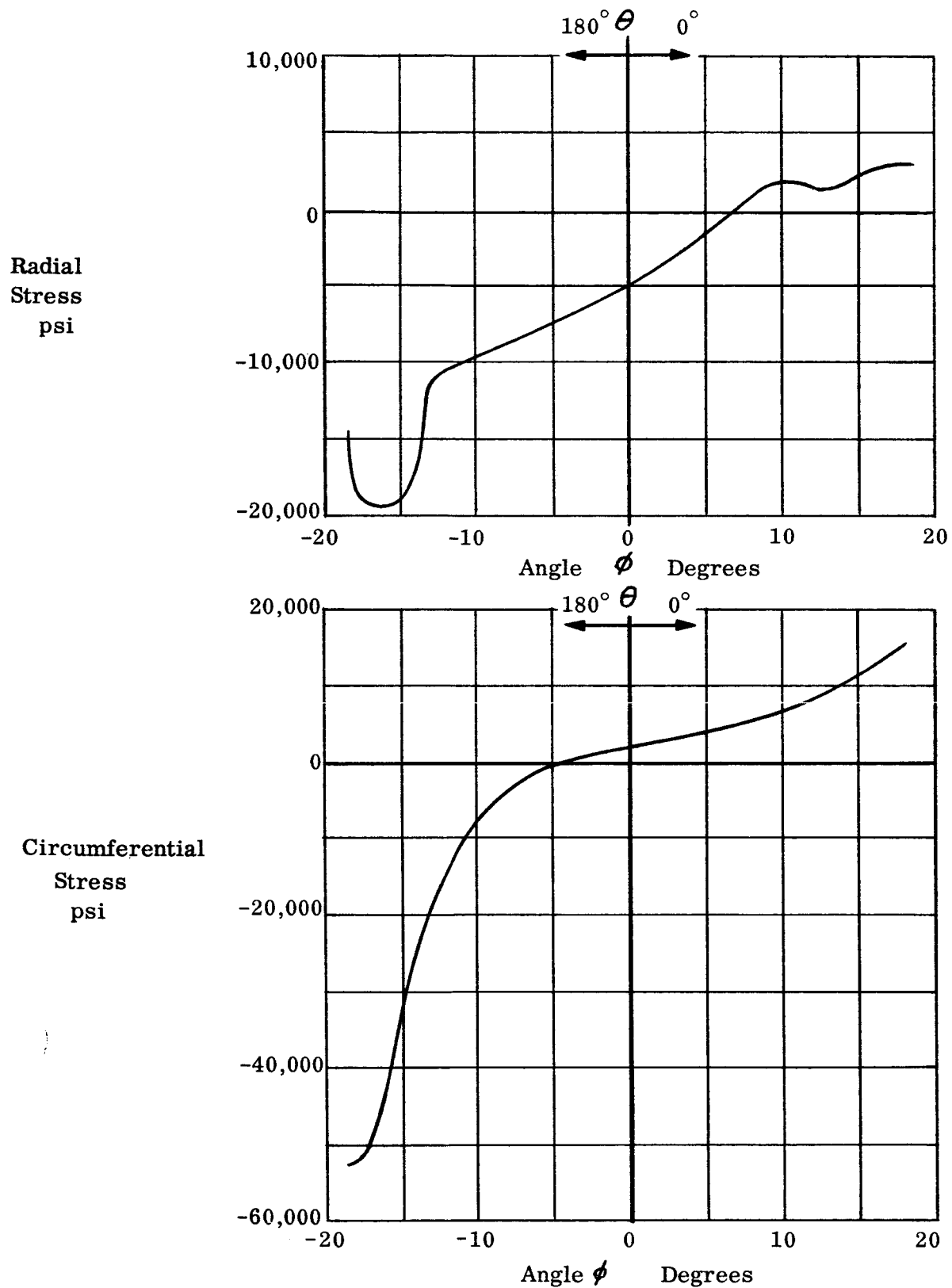
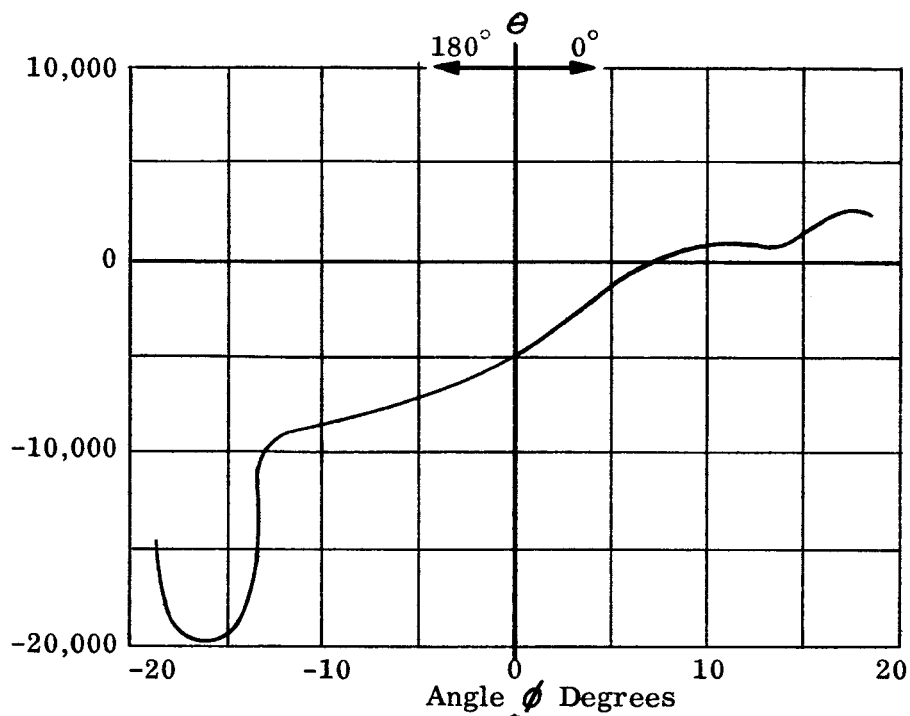


Figure II-29. Thermal Stresses in Lower Sandwich Face
Thermal Reentry Condition

Radial
Stress
psi



Circumferential
Stress
psi

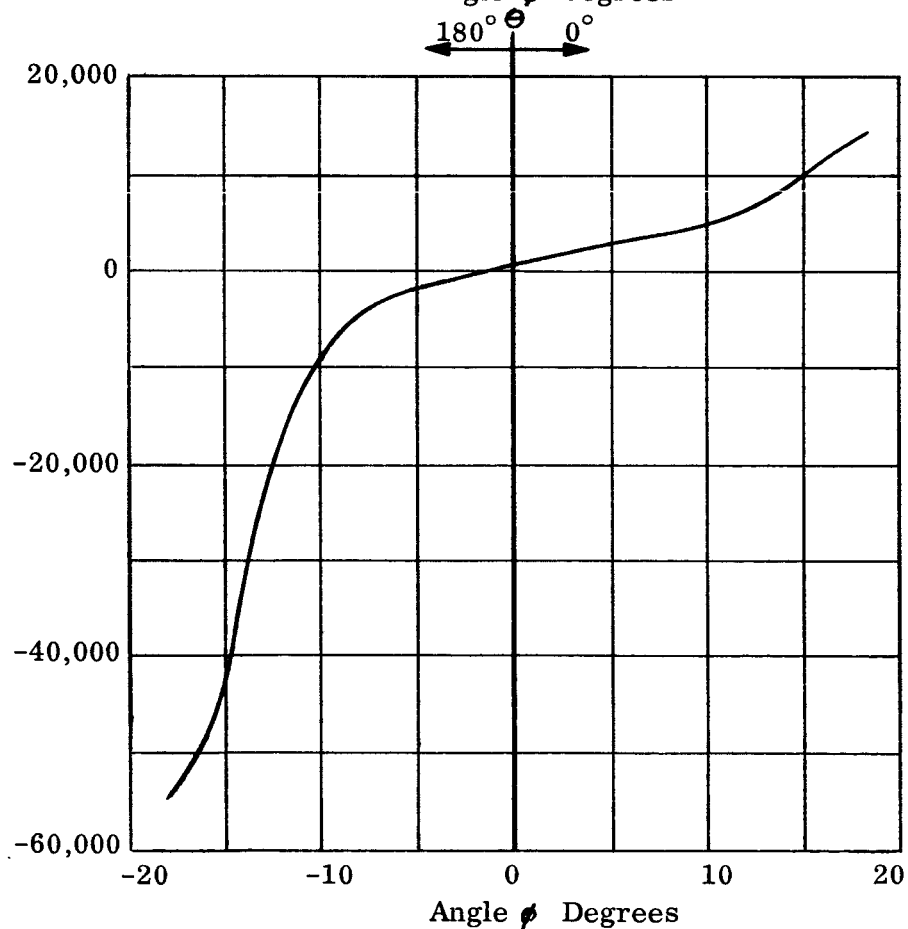


Figure II-30. Thermal Stresses in Upper Sandwich Face Thermal Reentry Condition

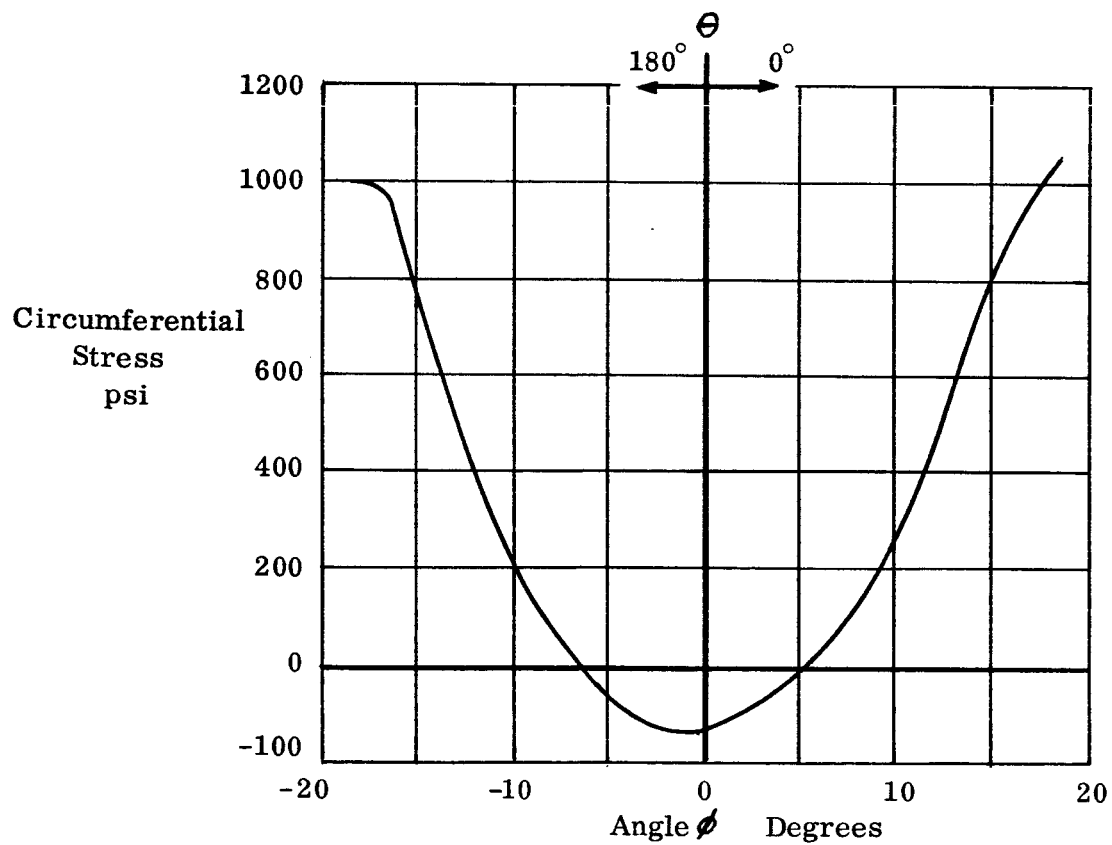
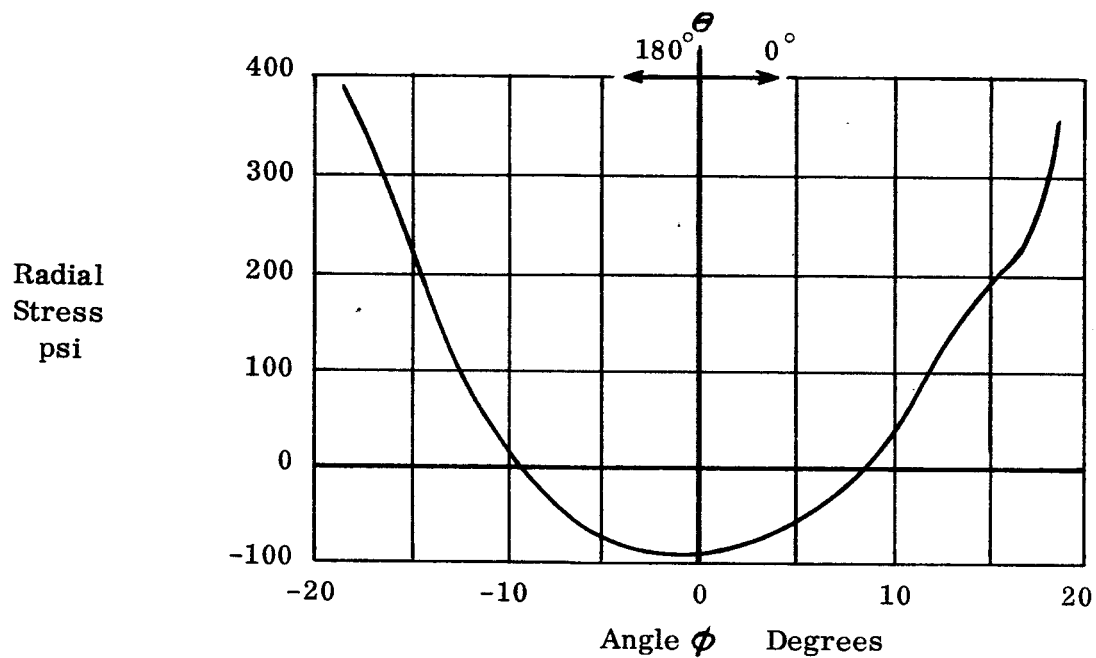


Figure II-31. Thermal Stresses in Top Surface of the Ablator Cold Soak Thermal Condition

III. DYNAMIC RESPONSE

A. INTRODUCTION

The basic design analyses described in the previous chapter have been performed on a purely static basis, utilizing very refined gridworks. The deflection curves, which have been obtained for various radii of wetted areas corresponding to points of the water impact pressure-time history do not include dynamic effects. Since the times involved are very small (< 0.05 sec), inertial and dynamic response effects may have an appreciable significance. Analyses in which the effects of dynamic response have been neglected generate results which are expected to be conservative. It is desirable to obtain some quantitative estimate of the degree of conservatism, if any, involved in the previous static analyses. For this purpose, the dynamic response of the Apollo heat shield due to water impact was determined, and the results are compared with those obtained from the static design analyses in this section.

The items of work covered by the complete dynamic response analyses program were as follows:

- (1) After review of the results of the static analyses, loading cases and an idealization for the heat shield were defined.
- (2) Using the gridwork selected, an analysis was performed to determine the displacement influence coefficient matrix. A mass matrix for the heat shield was also derived.
- (3) For the selected analysis conditions and structural idealization, load-time histories, $F(t)$, were developed for all loading points.
- (4) Dynamic analyses were then performed using the forcing functions defined previously.
- (5) Estimates were made of the significance of dynamic, as compared with static, behavior with regard to stresses.

Each of the above items of work is discussed in the following sections. A detailed explanation of the theory and procedures underlying these dynamic analyses appears in Appendix B.

B. STRUCTURAL IDEALIZATION

The chosen idealization appears in Figure III-1. In this idealization, a total of 97 grid points on the surface (or middle surface) of the heat shield are free to displace. Although five degrees of freedom at such points appear in the determination of stiffness, only one degree of freedom at each point – that which is normal to the surface – is considered in dynamic response analysis.

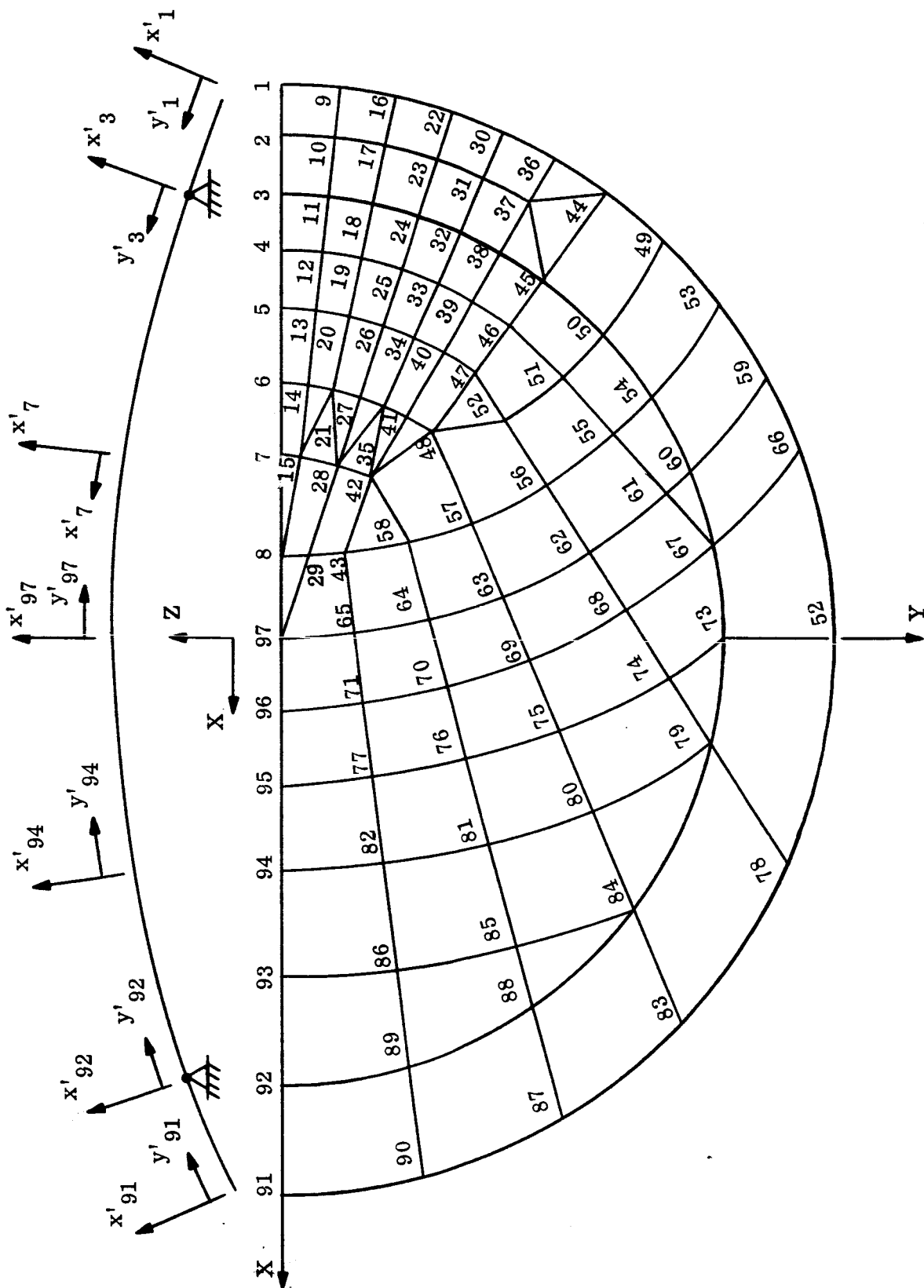


Figure III-1. Heat Shield Structural Idealization Grid

The procedure for obtaining the desired flexibility characteristics is as follows. The stiffness matrix for the structure is constructed by the Bell General Purpose Structural Analysis Program in the form

$$\begin{Bmatrix} P_x \\ P_y \\ P_z \\ M_\phi \\ M_\theta \end{Bmatrix} = \begin{bmatrix} k_{xx} & & & & \\ & k_{yy} & & & \\ & & k_{zz} & & \\ & & & k_{\phi\phi} & \\ & & & & k_{\theta\theta} \end{bmatrix} \begin{Bmatrix} u \\ v \\ w \\ \phi \\ \theta \end{Bmatrix} \quad (\text{Symmetric}) \quad (\text{III-1})$$

where x , y and z are coordinate directions in and normal to the tangent planes at the respective points and ϕ and θ are angular displacements in the x and y directions. Inversion of the above stiffness matrix yields

$$\begin{Bmatrix} u \\ v \\ w \\ \phi \\ \theta \end{Bmatrix} = \begin{bmatrix} \delta_{xx} & & & & \\ & \delta_{yy} & & & \\ & & \delta_{zz} & & \\ & & & \delta_{\phi\phi} & \\ & & & & \delta_{\theta\theta} \end{bmatrix} \begin{Bmatrix} P_x \\ P_y \\ P_z \\ M_\phi \\ M_\theta \end{Bmatrix} \quad (\text{Symmetric}) \quad (\text{III-2})$$

where the δ 's are flexibility influence coefficients. The desired flexibility coefficients, however, are only those which relate the P_x 's to the u 's, i.e. δ_{xx} .

In the Bell General Purpose Structural Analysis Program, instructions are provided which allow the assignment of the complete inverted stiffness matrix to tape storage. The analyst then designates the rows and columns to be recalled and thereby constructs the desired flexibility matrix, in this case δ_{xx} .

The idealization shown in Figure III-1 was also used to determine the mass properties of the heat shield. Initially the surface area subtended by sets of grid points was calculated, such as the area bounded by points 11, 12, 19, and 18. One-quarter of this area was assigned to each corner grid point. In this manner the surface area assigned to each grid point is found. Next, the ablator, face sheet and

core thicknesses were determined for the assigned area resulting in assigned volumes for each of these structural elements. These volumes were multiplied by the proper density values to obtain weights. Table III-1 lists the assigned areas, structural element weights and total weight.

The mass matrix $[M]$, to be used in the dynamic response study is easily constructed from Table III-1 by placing the pertinent weight, divided by g , for each grid point on the main diagonal of this matrix. This approach, commonly labeled the "mass lumping technique," results in zero-valued off diagonal terms.

C. LOAD-TIME HISTORIES

Forcing functions or load-time histories, $F(t)$, were developed for each grid point. Each loading curve is based on the impact pressure-time and wetted radius-time histories shown in Figure III-2 for a chosen impact angle of $\phi = 15^\circ$ and vertical impact velocity of 35 ft/sec. A particular grid point load-time history was constructed by determining the time, t_p , at which the grid point was "wetted" through use of the wetted radius-time history curve and grid point coordinates. The pressure-time history curve is entered at t_p to find the pressure decay for the grid point. Load time histories are easily determined by multiplication of the grid point pressure-time history by the pertinent surface area. Typical results are shown in Figures III-3 and III-4 for grid points 7 and 57 respectively. These results are conservative in nature since the heat shield is to be subjected (theoretically) to a peak force which is greater than that obtained if the actual rate of wetted grid point area were considered. In the latter instance a monotonic increase of force with time would occur starting at some $t_1 < t_p$ and peaking at some $t_2 > t_p$. The peak value would be less than that shown due to the pressure decay. This phenomenon is of negligible importance for grid points near the impact point where the radius of wetted area changes rapidly with time.

The forcing function data are prepared as input to the dynamic response program by providing the coefficients of the exponential function

$$F(t) = A e^{Bt+C} \quad (\text{III-3})$$

These coefficients were determined by a "least-squares" technique applied to the basic pressure decay curve of Figure III-2. The most accurate results were obtained by fitting exponentials to the time regions $0.001 \leq t \leq 0.010$ and $0.010 < t \leq 0.05$. These are shown on Figure III-2. The coefficient A in Equation III-3 represents the assigned grid point area. It is noted that Equation III-3 is only used in the time region $t \geq t_p$. For $t < t_p$ $F(t)$ is set equal to zero.

TABLE III-1
NODE POINT COORDINATES - REVISED GRID

(See Figure III-1 for Layout)

	X	Y	Z		X	Y	Z
1	-72.21	0	160.066	41	-29.012	16.75	172.375
2	-65.155	0	163.065	42	-20.785	12.0	173.952
3	-58.100	0	165.710	43	-11.184	9.083	175.008
4	-51.00	0	168.031	44	-58.419	42.444	160.066
5	-43.0	0	170.254	45	-47.004	34.150	165.710
6	-33.500	0	172.375	46	-41.260	29.977	168.031
7	-24.000	0	173.952	47	-34.788	25.275	170.254
8	-10.550	0	175.238	48	-27.102	19.691	172.375
9	-71.814	7.548	160.066	49	-51.634	50.480	160.066
10	-64.798	6.810	163.065	50	-39.527	42.582	165.710
11	-57.781	6.073	165.710	51	-34.077	37.240	168.188
12	-50.721	5.331	168.031	52	-28.481	29.784	170.696
13	-42.764	4.495	170.254	53	-44.153	57.139	160.066
14	-33.316	3.502	172.375	54	-32.046	48.463	165.710
15	-23.868	2.509	173.952	55	-27.086	43.461	167.967
16	-70.632	15.013	160.066	56	-20.555	34.759	170.894
17	-63.731	13.546	163.065	57	-15.672	25.368	173.050
18	-56.830	12.080	165.710	58	-12.981	17.663	174.227
19	-49.886	10.603	168.031	59	-34.336	65.524	160.066
20	-42.060	8.940	170.254	60	-22.228	53.680	165.710
21	-32.768	6.965	172.375	61	-19.205	50.474	167.089
22	-68.676	22.314	160.066	62	-11.619	40.366	170.502
23	-61.966	20.134	163.065	63	-5.948	29.460	173.009
24	-55.256	17.954	165.710	64	-2.823	20.512	174.375
25	-48.504	15.760	168.031	65	-0.736	10.546	175.282
26	-40.895	13.288	170.254	66	-24.163	68.047	160.066
27	-31.860	10.352	172.375	67	-12.055	56.836	165.710
28	-22.825	7.416	173.952	68	-3.514	45.456	169.578
29	-10.643	3.458	175.243	69	2.872	33.174	172.415
30	-65.967	29.370	160.066	70	6.392	23.094	173.957
31	-59.522	26.501	163.065	71	8.741	11.877	174.980
32	-53.077	23.631	165.710	72	0	72.210	160.066
33	-46.591	20.744	168.031	73	0	58.100	165.710
34	-39.282	17.490	170.254	74	5.212	50.928	167.972
35	-30.604	13.625	172.375	75	12.365	37.170	171.176
36	-62.536	36.105	160.066	76	16.309	25.877	172.915
37	-56.426	32.578	163.065	77	18.941	13.309	174.067
38	-50.316	29.050	165.710	78	29.260	66.016	160.066
39	-44.167	25.500	168.031	79	13.935	56.404	165.710
40	-37.239	21.500	170.254	80	21.858	41.167	169.301

TABLE III-1 (CONT)

	X	Y	Z
81	26.266	28.659	171.250
82	29.141	14.471	172.537
83	49.343	52.721	160.066
84	34.734	46.574	165.710
85	39.672	32.431	167.958
86	42.971	16.678	169.442
87	61.121	38.451	160.066
88	46.797	34.433	165.710
89	55.115	18.383	165.710
90	69.278	20.368	160.066
91	72.210	0	160.066
92	58.100	0	165.710
93	44.135	0	169.964
94	30.170	0	172.989
95	19.870	0	174.437
96	9.570	0	175.339
97	0	0	175.6

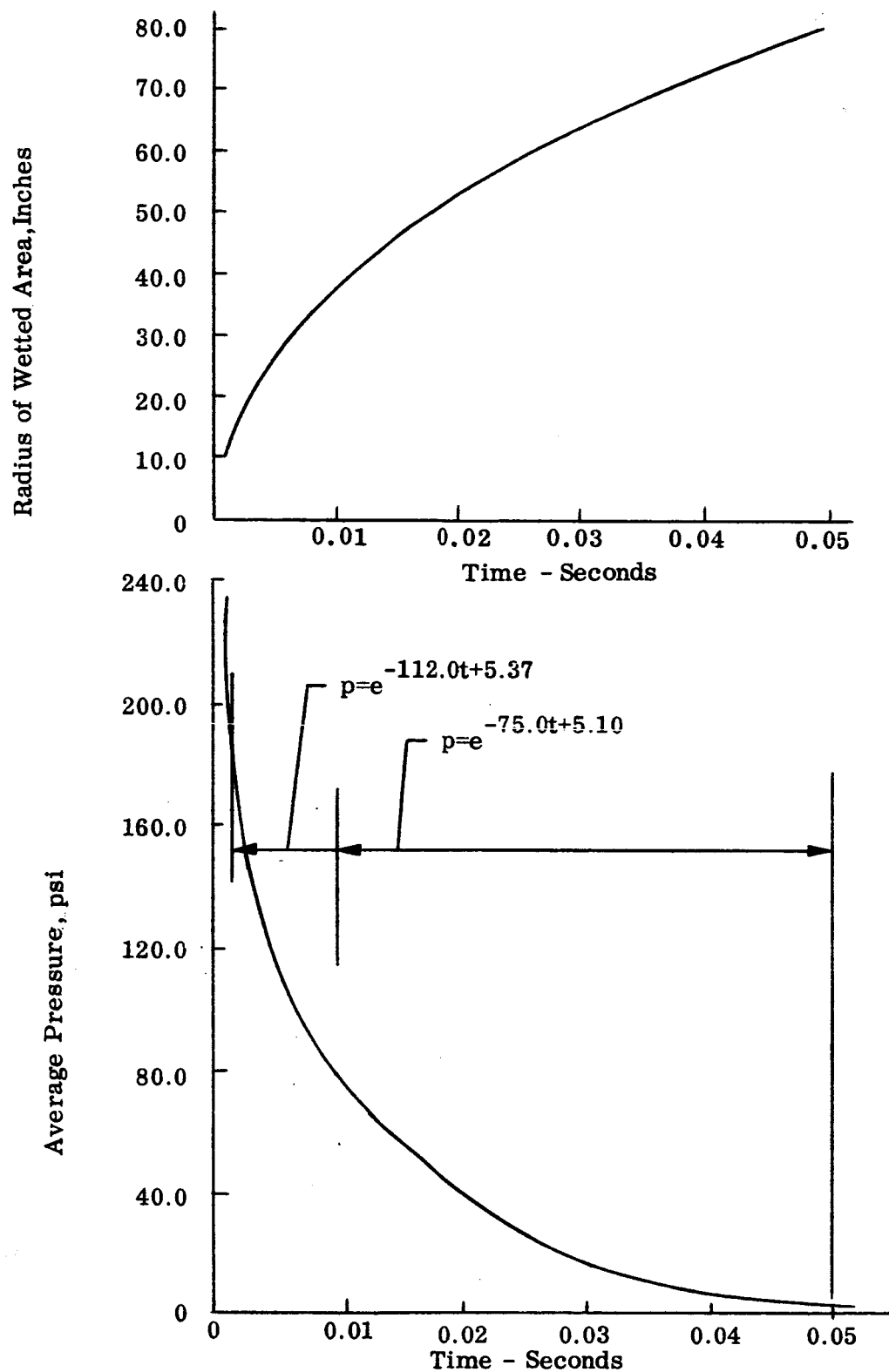


Figure III-2. Pressure and Radius Time Histories
 $\phi = 15^\circ$, $V_v = 35.0$ ft/sec

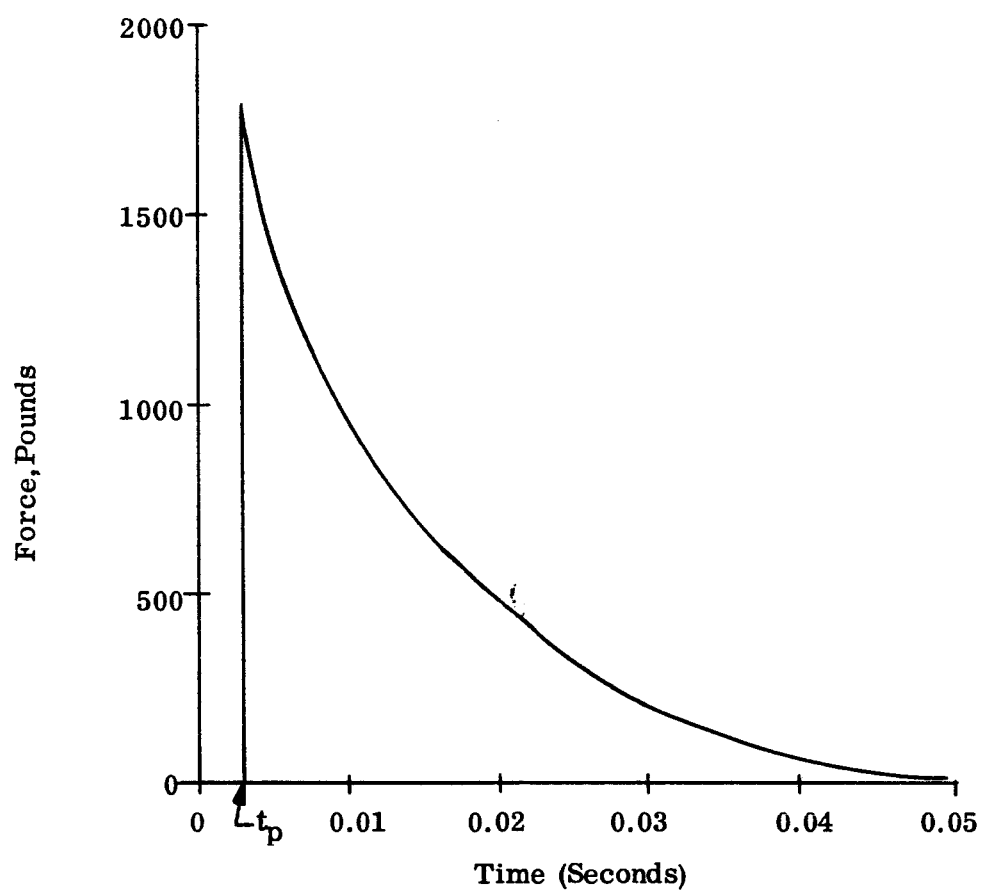


Figure III-3. Forcing Function - Grid Point 7

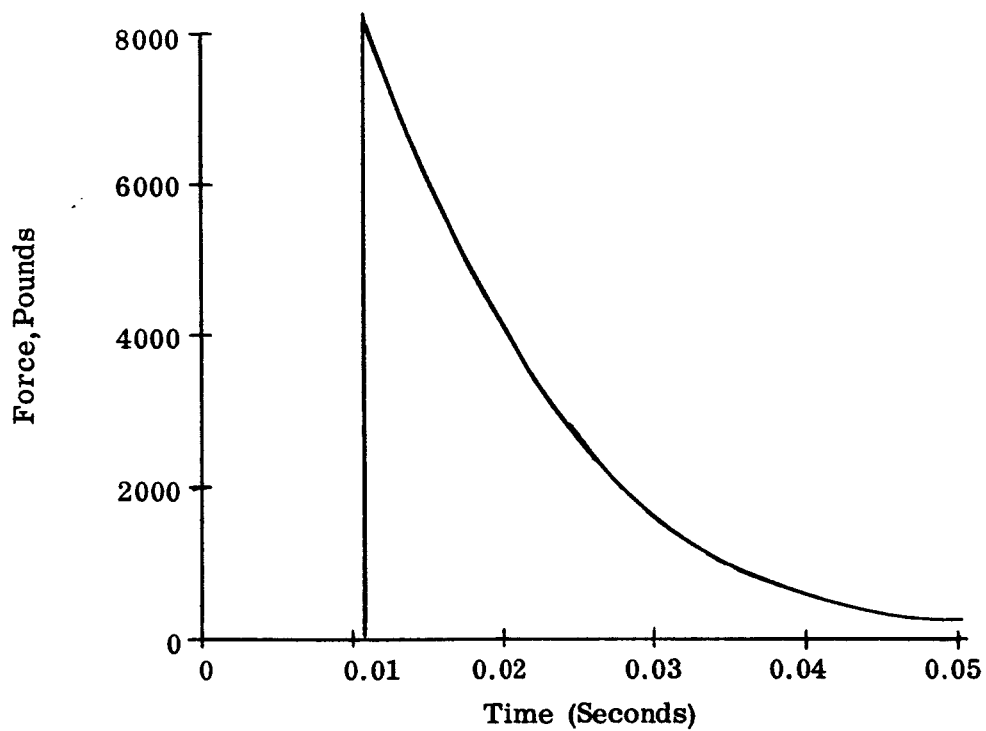


Figure III-4. Forcing Function - Grid Point 57

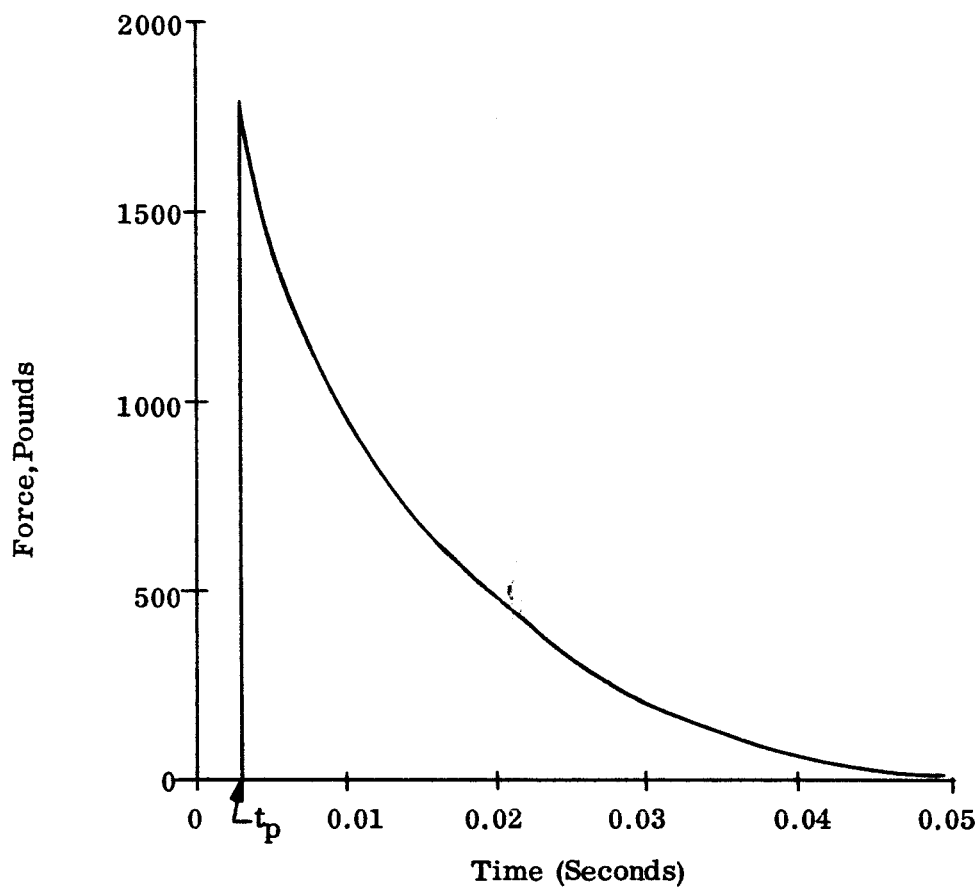


Figure III-3. Forcing Function - Grid Point 7

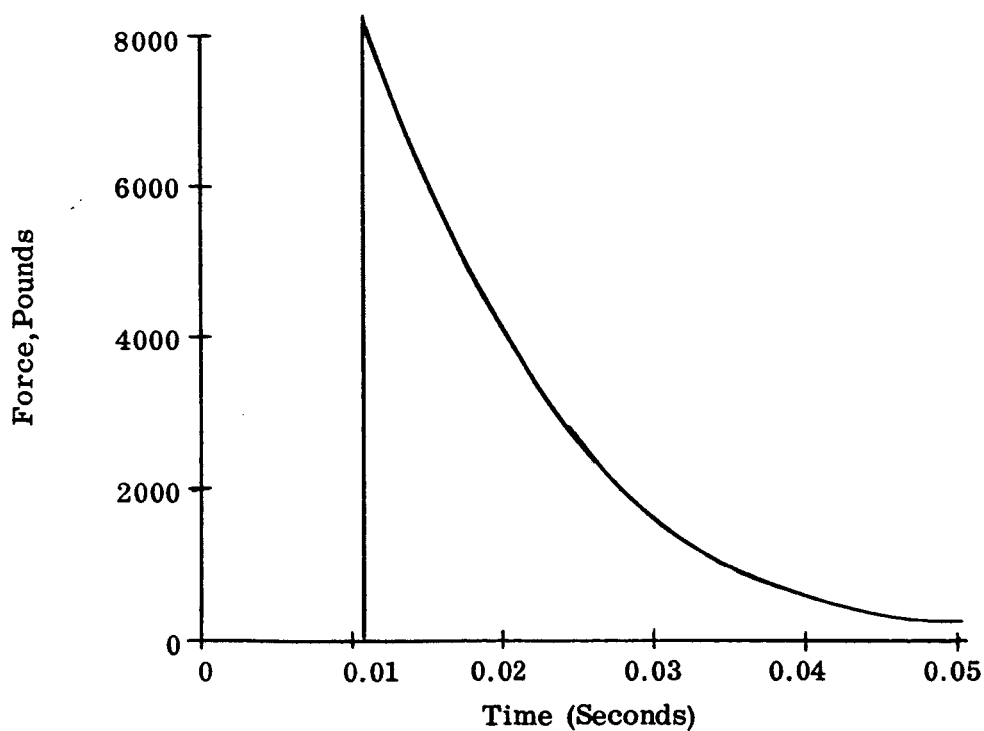


Figure III-4. Forcing Function - Grid Point 57

D. DYNAMIC RESPONSE

The dynamic response of the Apollo heat shield was determined by use of the techniques described in Appendix B. This technique utilizes the natural modes and frequencies of vibration of the subject structure.

A matrix iteration technique was used to determine the vibrational characteristics. Mathematically, the eigenvalues (natural frequencies) and eigenvectors (mode shapes) of the following matrix equation must be found.

$$[\delta_{xx}] [M] \{u\} = \frac{1}{\omega^2} \{u\} \quad (\text{III-4})$$

The matrix $[\delta_{xx}]$ is the set of flexibility influence coefficients described by Equation (III-4). $\{u\}$ is a column of displacements and $[M]$ is the diagonal mass matrix constructed from the total weight column shown in Table III-1. The flexibility matrix is reduced to 80th order by virtue of the boundary conditions along the centerline of the heat shield and bolt circle support points. The mass matrix is also of this order. The first ten modes and frequencies were obtained from Equation (III-4) and these are tabulated in Table III-2. Additional mode shapes are given in Reference

. The mode shapes for the first two modes are shown in Figures III-5 and III-6 where negative modal values at each grid point are shown by the cross-hatched areas. Relative amplitudes for the centerline grid points, using grid point 97 as the normalizing station, are shown in the upper portion of each figure. Approximate node line locations (points of zero displacement) are also shown. Examination of these figures shows that only modes symmetrical about the heat shield centerline are obtained. This is due to the fact that the flexibility matrix $[\delta_{xx}]$ was constructed on the basis of symmetric loadings being applied to the subject structure. The associated modal deflection pattern is reflected in the boundary conditions consistent with the applied loadings. The calculated frequencies associated with each mode are shown in Table III-2.

TABLE III-2
VIBRATION MODE AND FREQUENCY DATA

Mode	Frequency (rad/sec)	Generalized Mass	Generalized Stiffness	Generalized Damping
1	592.0	19.80	6.94×10^6	100.41
2	657.6	47.50	20.56×10^6	297.55
3	683.6	12.10	5.67×10^6	82.04
4	750.6	51.30	28.92×10^6	418.45
5	813.9	187.00	123.84×10^6	1719.94
6	848.7	0.10	0.07×10^6	1073.55
7	869.9	4.30	3.28×10^6	47.49
8	941.6	42.17	37.39×10^6	540.96
9	984.1	0.68	0.66×10^6	9.54
10	1112.0	128.39	158.76×10^6	227.29

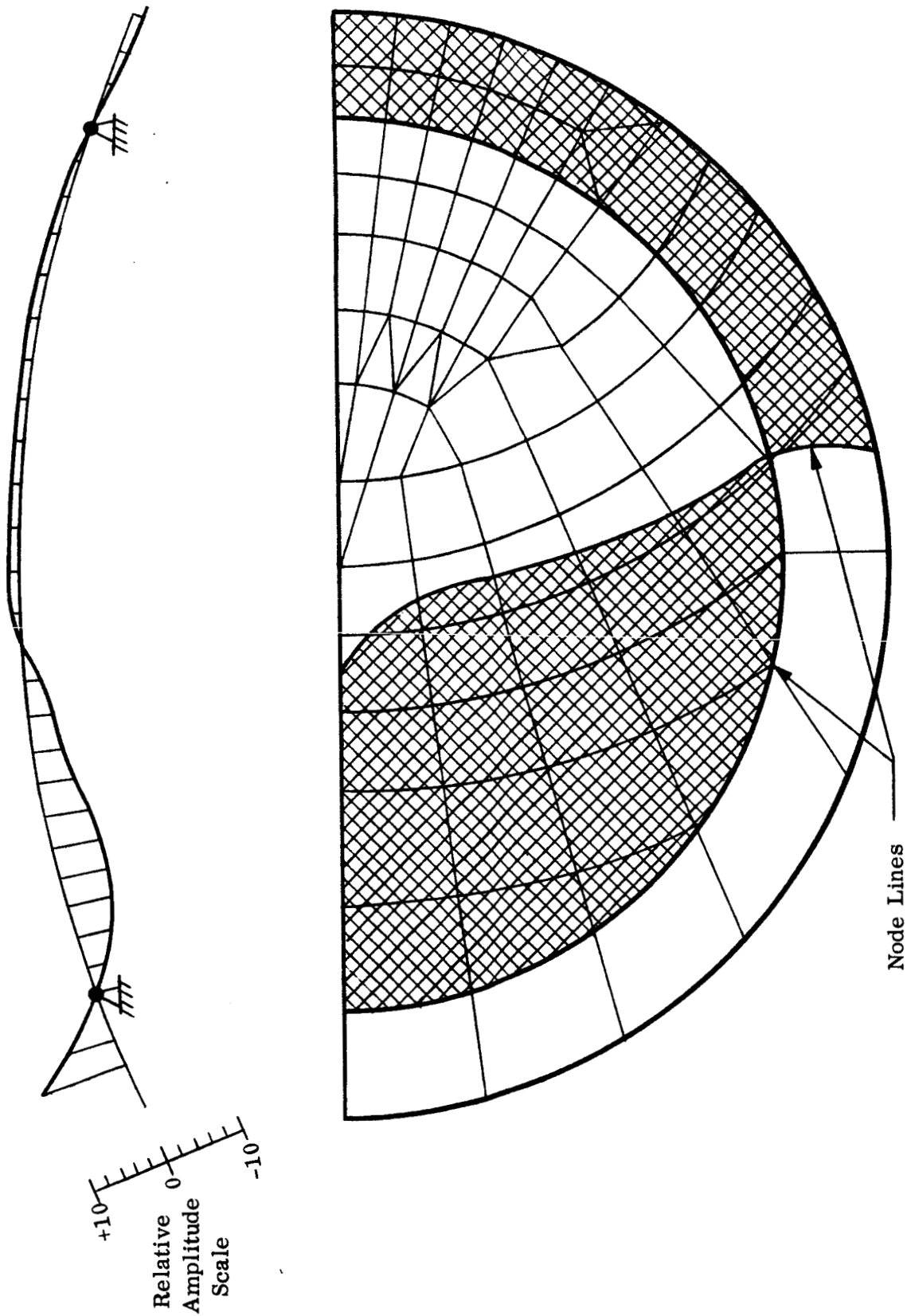


Figure III-5. Heat Shield First Vibration Mode Shape ($f_1 = 94.26$ cps)

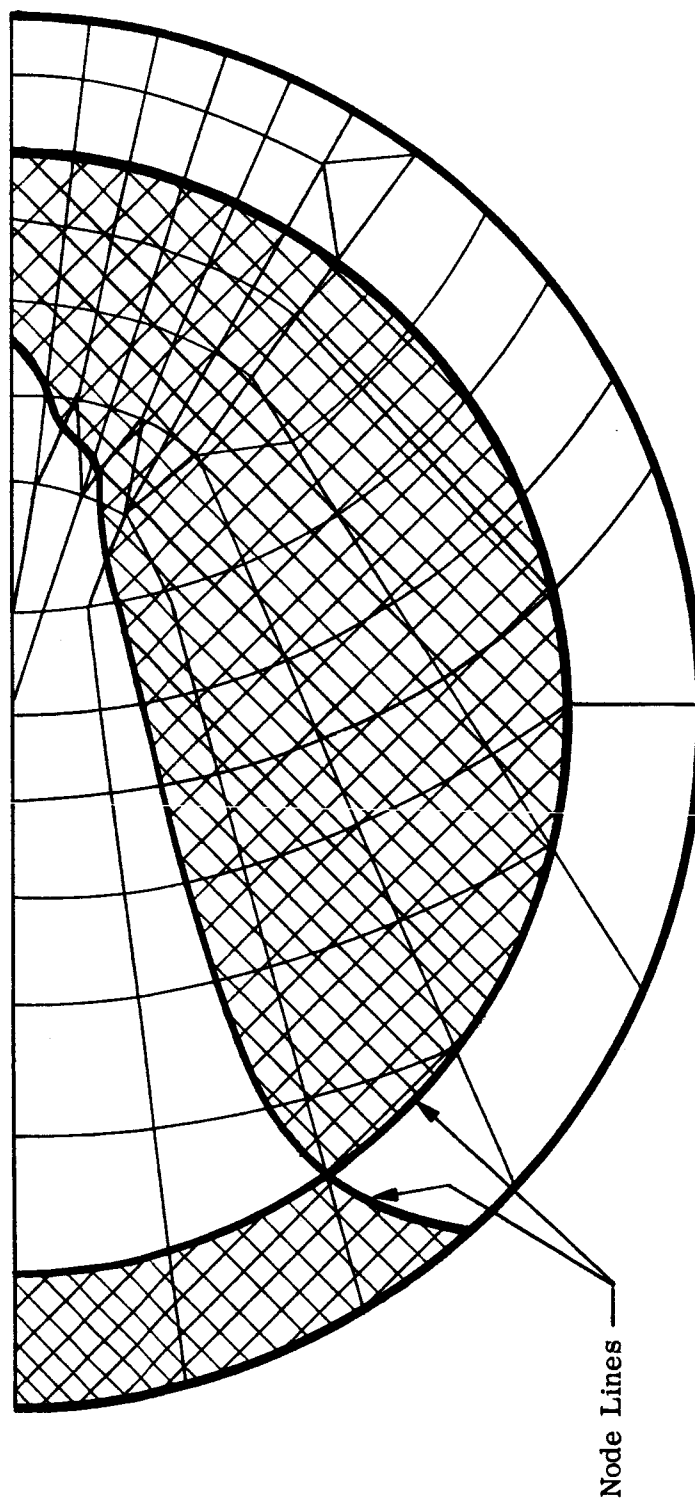
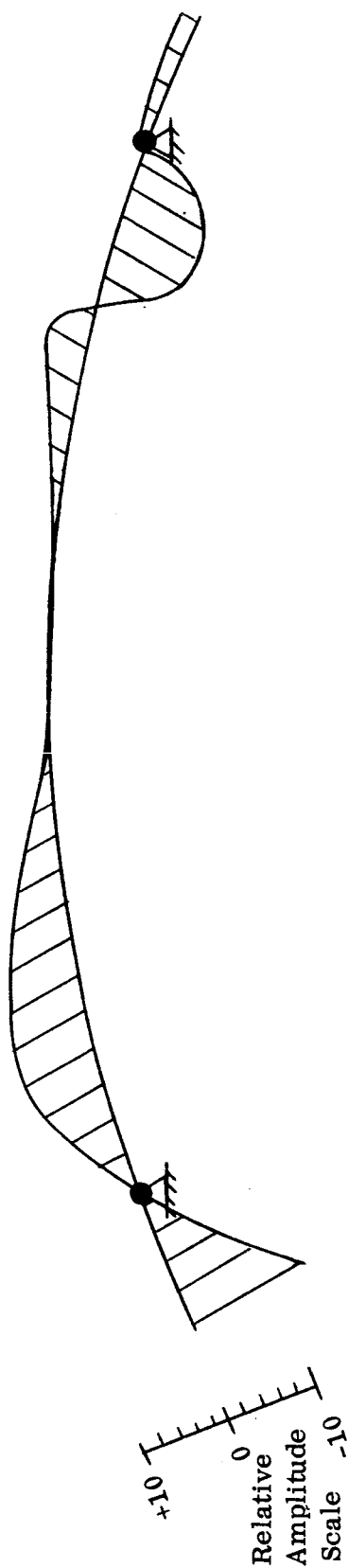


Figure III-6. Heat Shield Second Vibration Mode Shape ($f_2 = 104.74$ cps)

The frequencies range from 592 rad/sec (94.3 cps) to 1112 rad/sec (178.5 cps).

The method of solution for dynamic response as described in Appendix B assumes that the displacement of any grid point due to a dynamic load can be obtained by a summation of products of mode shapes (relative displacements) and generalized coordinates. That is

$$u(x_i, y_i, t) = \sum_{j=1}^{\infty} \bar{u}_j(x_i, y_i) \xi_j(t) \quad (\text{III-5})$$

where $\bar{u}_j(x_i, y_i)$ is the j th normalized vibration mode shape evaluated at the i th point and $\xi_j(t)$ is the generalized coordinate in the j th mode. Use of Equation (III-5) leads directly to generalized mass, stiffness and damping terms defined as follows

$$M_j = \sum_{i=1}^N m_i [\bar{u}_j(x_i, y_i)]^2 \quad (\text{III-6})$$

$$K_j = \omega_j^2 M_j \quad (\text{III-7})$$

$$D_j = \frac{g_j \omega_j^2 M_j}{\omega} \quad (\text{III-8})$$

In the present application the summations extend from $i = 1$ to 80, $j = 1$ to 10. Generalized mass, stiffness, and damping values associated with each mode are listed in Table III-2. These values form the elements of the diagonal mass, stiffness and damping matrices in the equations of motion. (See Equation B-23, Appendix B.)

Although formation of the generalized mass and stiffness terms is straightforward, some discussion of the damping terms is needed. The coefficient g_j in Equation (III-8) is defined to be the damping coefficient associated with each vibration mode and is expressed in terms of critical damping as

$$g_j = \frac{2c_j}{c_c} \quad \text{where} \quad c_c = 2\sqrt{K_j M_j} \quad (\text{III-9})$$

In the present application g_j was assumed to be equal for all modes. The parameter ω in Equation (III-8) is the frequency response of each generalized coordinate and is unknown at the outset of the analysis. This frequency is easily estimated however by averaging the response frequencies for the undamped case. For the present analyses, ω was assumed to be 110.0 cps.

The matrix equations of motion (Equations B-23 , Appendix B) were solved by the use of the Bell Matrix Iteration Time History Program. Program output consists of time histories of the generalized coordinates and total grid point displacements. Typical results are shown in Figures III-7 to III-10 (additional results are displayed in Reference 2). The generalized responses shown are to be expected since the ratio of the period of the generalized force to natural period ranges from five to nine approximately. Upon removal of the exciting forces at $t = 0.050$ seconds each generalized mass-spring system oscillates at its natural frequency. The effect of structural damping upon maximum displacement is negligible for $g = 0.01$ as shown by the open circular symbols on Figures III-7 and III-8. An extreme case of damping, $g = 0.40$, shows a substantial decrease in amplitude and for ξ_5 the motion is entirely damped-out before the excitation pulse has vanished.

Total grid point displacements for zero damping are shown in Figures (III-9) for the centerline grid points 4 and 97. These are typical of the results obtained and additional grid point time histories are presented in Reference 5. Examination of the results showed that the frequency response during excitation varied between 100 and 140 cps approximately. During the period $0.05 \leq t \leq 0.080$, when the external forces are assumed to be zero, the frequency response is approximately 125 cps for all grid points.

A comparison between static and dynamic response is shown in Figures III-10 and III-11 at selected time intervals for the centerline grid points. These figures show that the deflections obtained by static response, in most instances, is greater than that obtained by dynamic response analyses. Of particular interest is the fact that as time increases the dynamic and static responses on the lower half of the heat shield (negative coordinate) become closer in agreement. Thus, the dynamic effects represent stress levels lower than the levels predicted in a static analysis. This conclusion lends justification to the performance of static analyses and loadings of the maximum acceleration, rather than for the apparently more critical loadings earlier on impact.

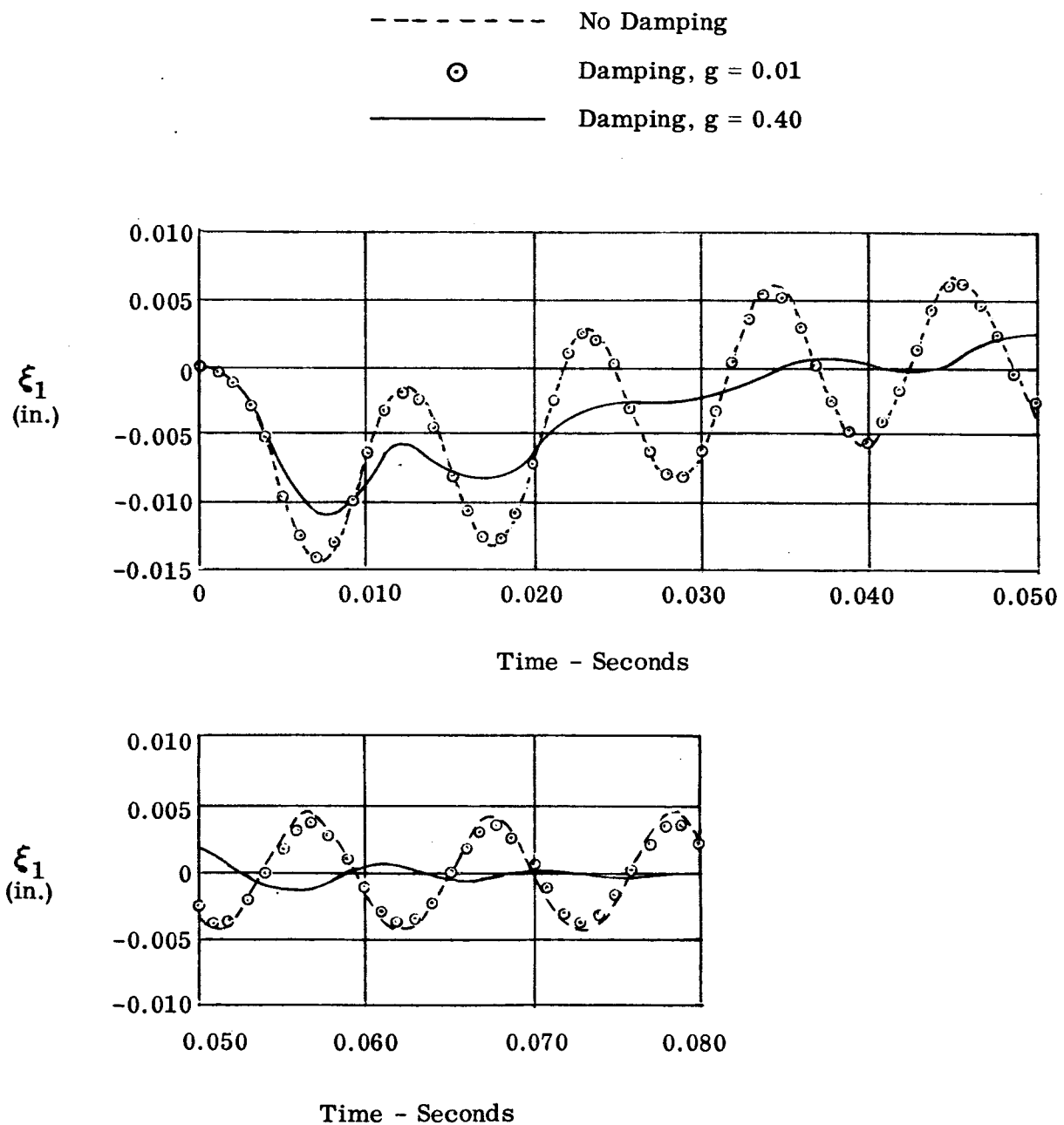
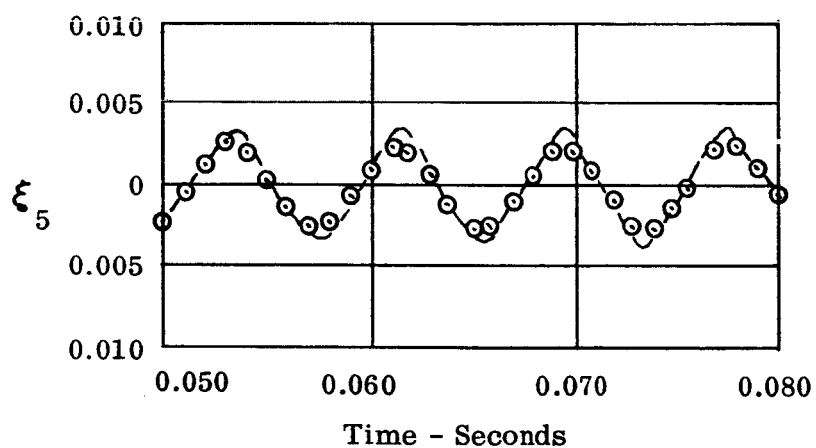
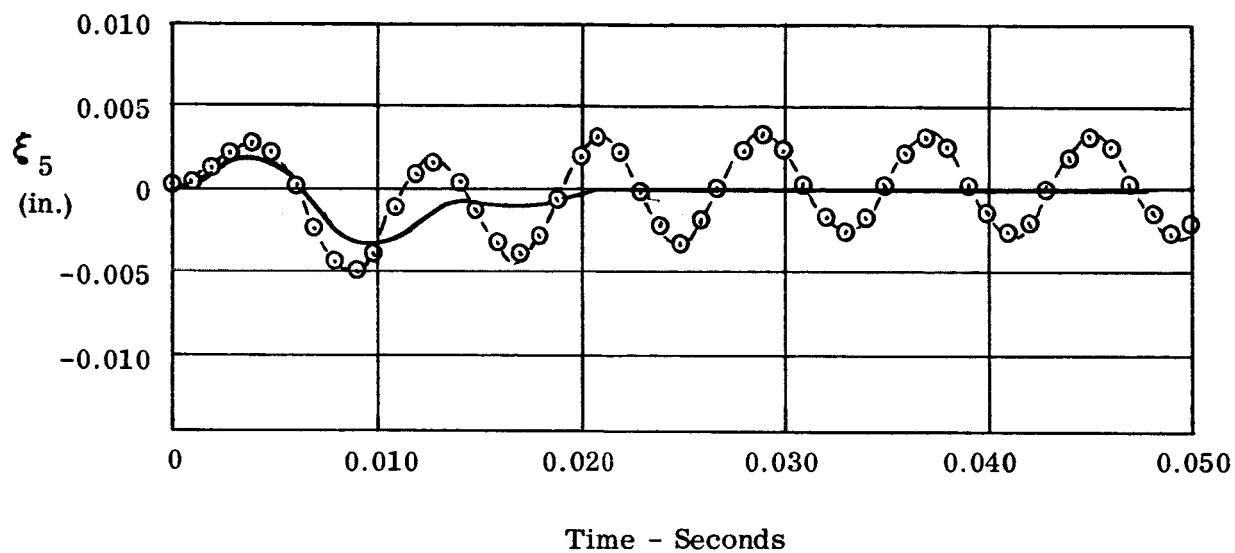


Figure III-7. Generalized Coordinate Versus Time



No Damping - - - -
 Damping, $g = 0.010$ \odot
 Damping, $g = 0.40$ ———

Figure III-8. Generalized Coordinate Versus Time

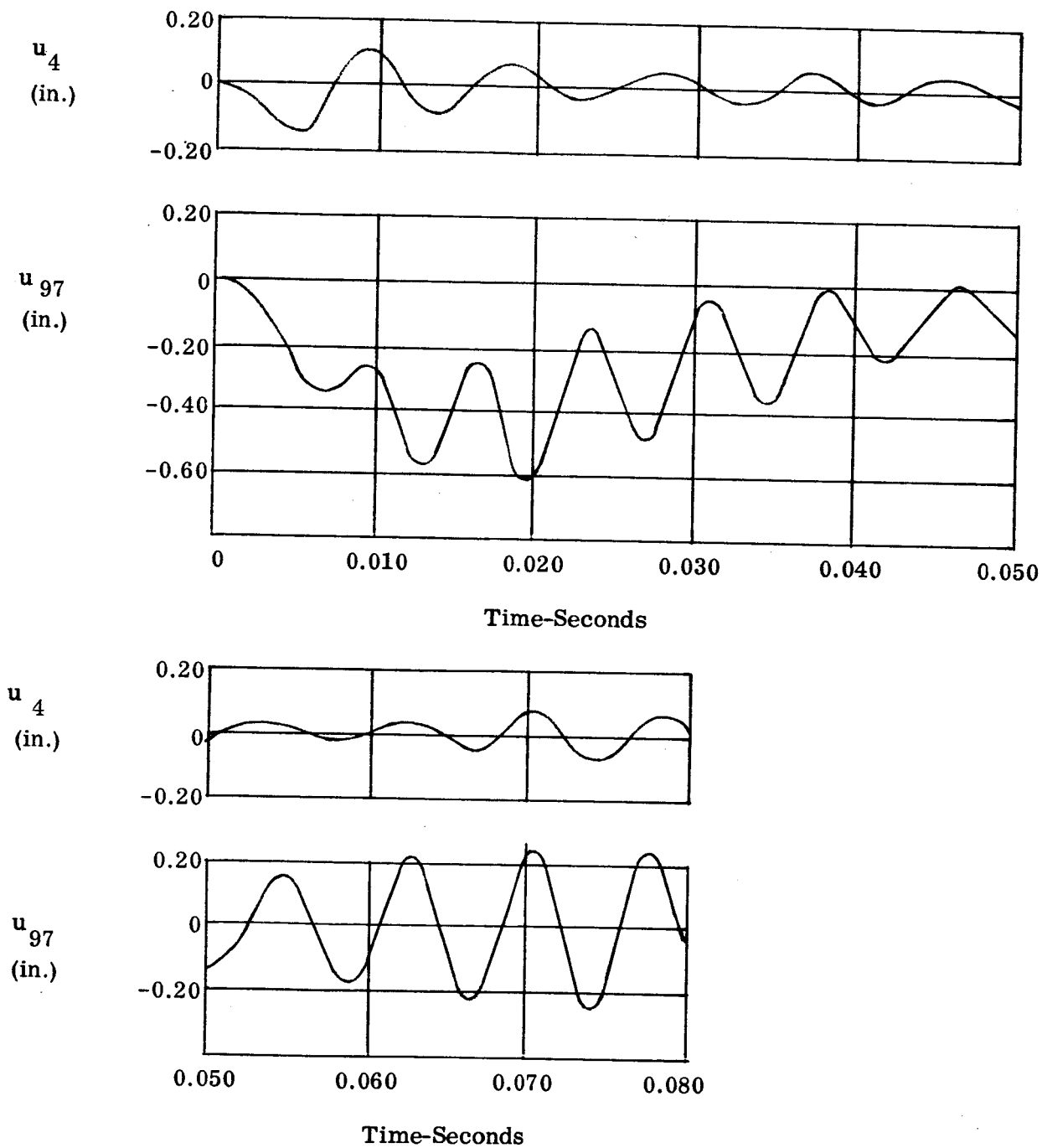
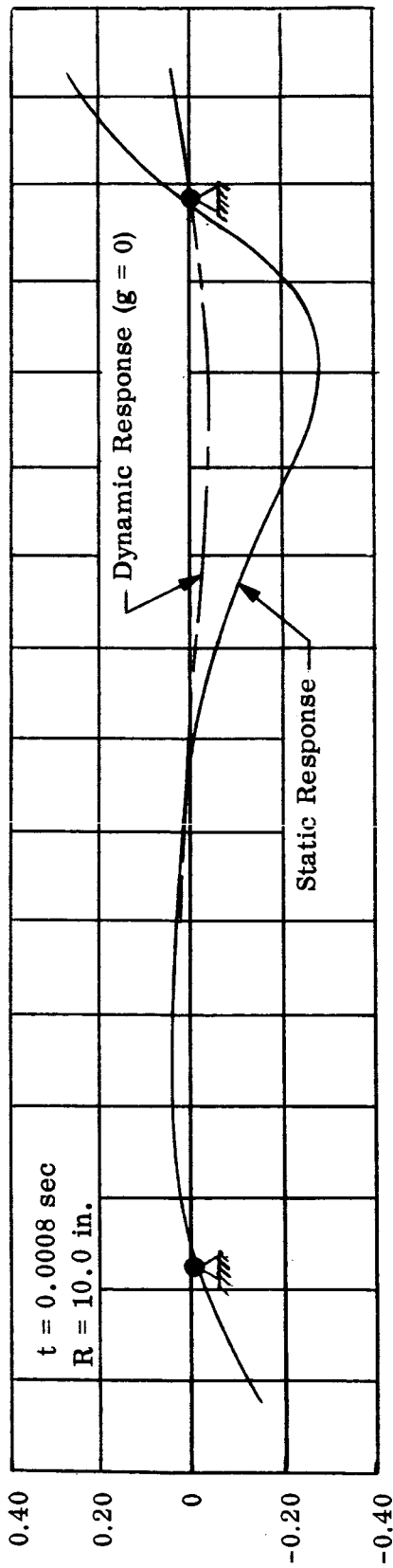


Figure III-9. Total Displacement Versus Time

Displacement - Inches



Displacement - Inches

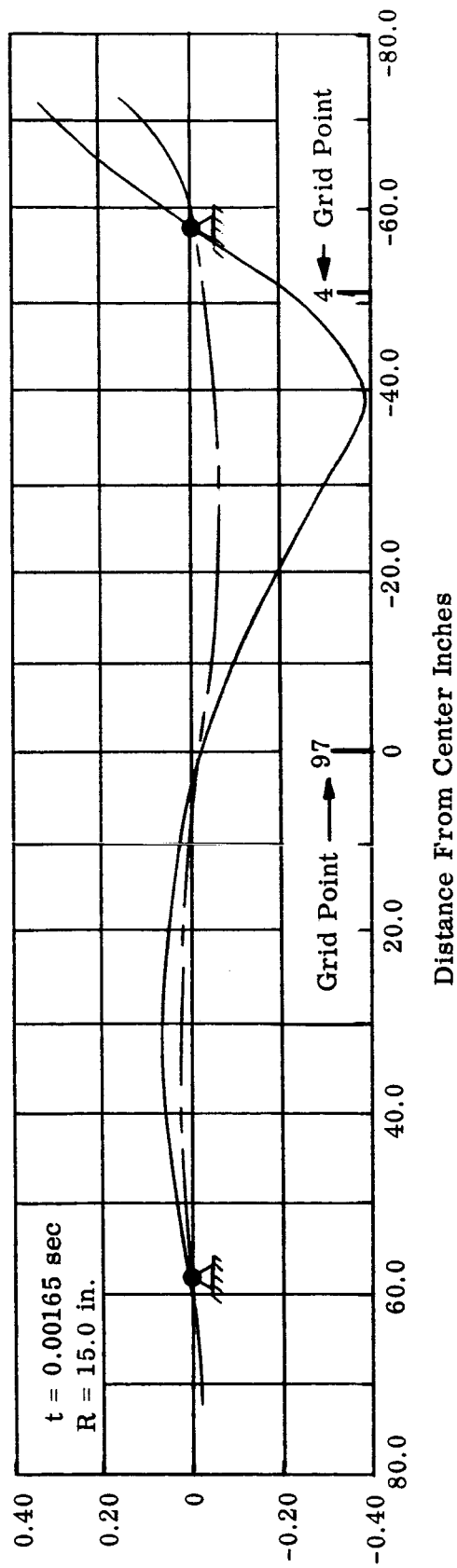


Figure III-10. Displacement Along Load Axis of Symmetry
 Impact Angle $\Phi = 15^\circ$

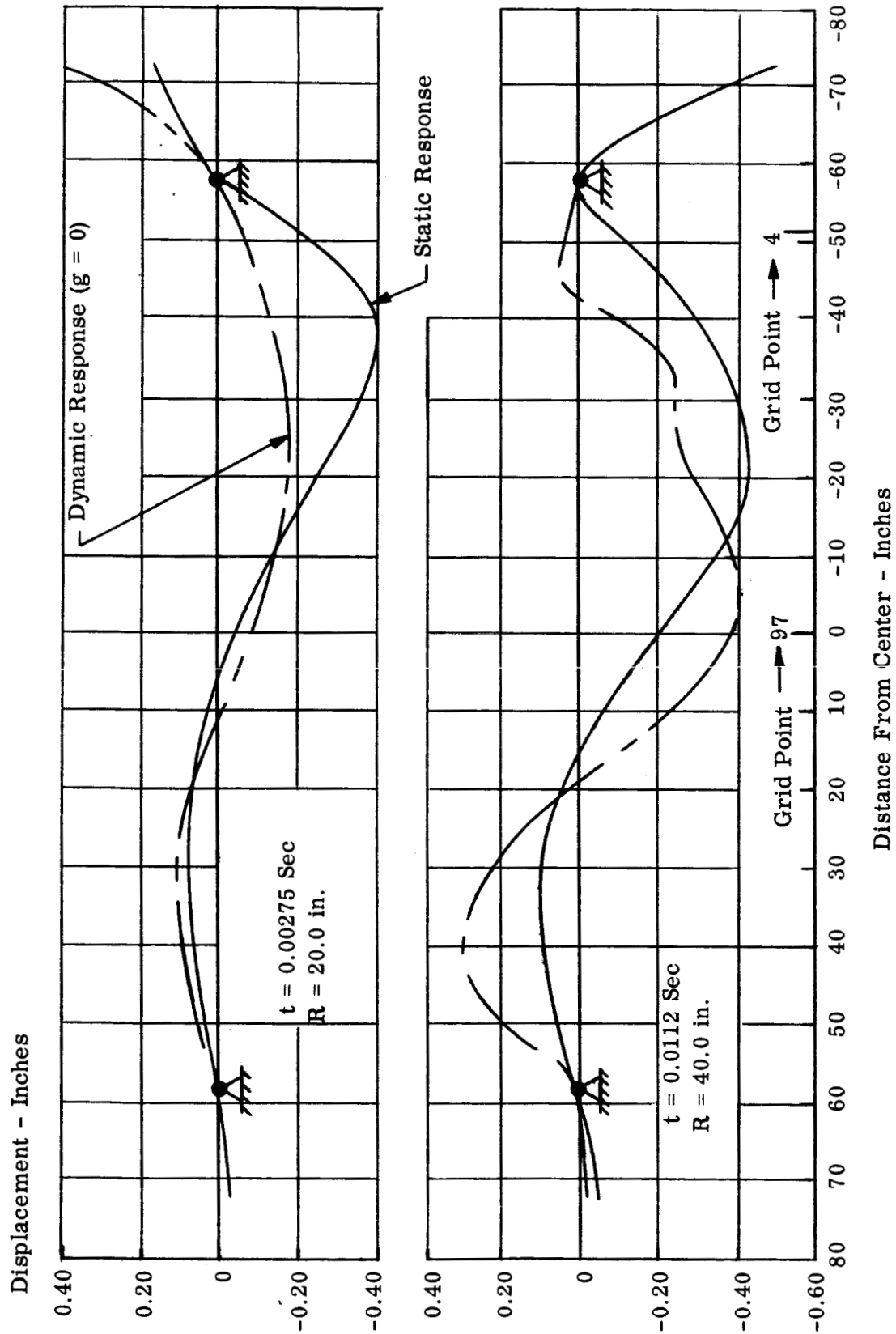


Figure III-11. Deflection Along Load Axis of Symmetry
Impact Angle $\phi = 15^\circ$

IV. INSTABILITY ANALYSES

A. OBJECTIVES

The water impact condition produces membrane stresses throughout the heat shield and it is conceivable that these stresses could be large enough to produce a failure of the heat shield in an elastic instability mode. The objectives of the work described in this section were to obtain the critical values of applied load for the water impact design condition based on a discrete element approach to linear instability analysis, modified by empirical correction factors.

The problem of determining elastic instability effects on the behavior of the scalloped heat shield during the water impact phase is one which cannot be solved through use of classical techniques with the expenditure of modest amounts of time and effort. Developments of the matrix displacement method, however, permit an engineering solution of this problem within the framework of this study.

The detailed work items in this area were as follows:

1. Perform instability analyses of a non-scalloped heat shield configuration for fixed support at the bolt circle under a uniform load condition.
2. Define available classical solution to the above case.
3. Compare results of discrete element and classical solutions.
4. Perform analyses of scalloped heat shield for water impact design conditions.

Item (4) was conducted for the case of a 10° impact angle and wetted radii of 10, 20, and 40 inches, respectively. A description of these efforts is given in the following paragraphs.

B. DESCRIPTION OF PROCEDURE

A detailed development of the present approach to elastic instability analysis is given in Appendix C. The following is a review of the basic concepts of this approach and its illustration by means of a simple problem.

It is possible to define, in connection with elastic instability phenomena, a hierarchy of sophistication in achieving solutions. This hierarchy is as follows:

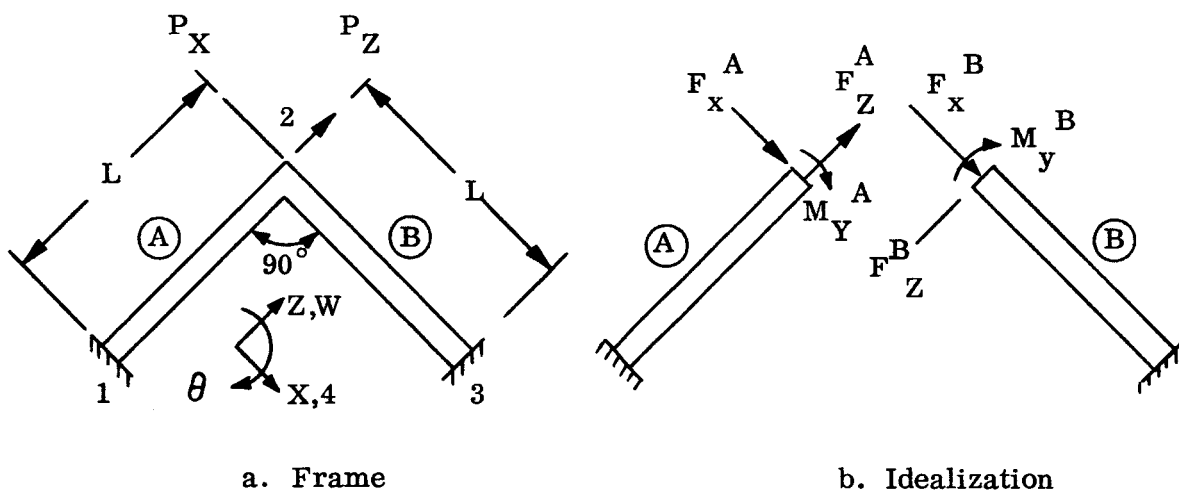


Figure IV-1. Simple Frame for Illustration of Instability Analysis Procedure

From Equilibrium

$$P_X = F_X^A + F_X^B, \quad P_Z = F_Z^A + F_Z^B, \quad M_Y = M_Y^A + M_Y^B \quad (\text{IV} - 2)$$

so that

$$\begin{Bmatrix} P_X \\ P_Z \\ M_Y \end{Bmatrix} = \begin{bmatrix} \frac{AE}{L} + \frac{12EI}{L^3} & 0 & -\frac{6EI}{L^2} \\ 0 & \frac{AE}{L} + \frac{12EI}{L^3} & -\frac{6EI}{L^2} \\ -\frac{6EI}{L^2} & -\frac{6EI}{L^2} & \frac{8EI}{L} \end{bmatrix} \begin{Bmatrix} u_1 \\ w_1 \\ \theta \end{Bmatrix} \quad (\text{IV} - 3)$$

and, solving

$$\begin{Bmatrix} u_1 \\ w_1 \\ \theta \end{Bmatrix} = \frac{1}{(H)} \begin{bmatrix} \left(\frac{AE}{L} + \frac{12EI}{L^3} \right) \frac{8EI}{L} - \left(\frac{6EI}{L^2} \right)^2 & (\text{SYMMETRIC}) \\ \left(\frac{6EI}{L^2} \right)^2 & \left[\left(\frac{AE}{L} + \frac{12EI}{L^3} \right) \frac{8EI}{L} - \left(\frac{6EI}{L^2} \right)^2 \right] \\ \left(\frac{AE}{L} + \frac{12EI}{L^3} \right) \frac{6EI}{L^2} & \left(\frac{AE}{L} + \frac{12EI}{L^3} \right) \frac{6EI}{L^2} & \left(\frac{AE}{L} + \frac{12EI}{L^3} \right)^2 \end{bmatrix} \begin{Bmatrix} P_X \\ P_Z \\ M_Y \end{Bmatrix} \quad (\text{IV} - 4)$$

- (1) The middle surface direct stresses are evaluated in a membrane analysis. This approach is common to "classical" methods of instability analysis. It is not adopted in the discrete element approach because:
 - (a) The middle surface direct forces are as conveniently determined in an analysis which includes flexure as in one which does not.
 - (b) It is possible for a singular stiffness matrix to be associated with a purely membrane model of a structure which is designed to carry bending moments.
 - (c) It is not convenient to input predetermined values of the internal forces into the existing Bell buckling analysis program.
 - (d) In certain cases, the membrane stresses are significantly affected by flexure.
- (2) The middle surface stresses are determined in an analysis that includes both flexure and axial behavior, but excludes finite deflection effects. (The axial strain-displacement equations do not include strains due to flexure.)
- (3) The determination of middle surface stresses stems from an analysis which includes finite deflection effects.

Procedure (2) is perhaps clarified by the problem shown in Figure IV-1a, which is a simple frame. It can also be regarded, however, as the two-dimensional counterpart of the shell problem. Figure IV-1b shows the discrete element idealization. Only point 2 is free to move so that stiffness equations need be written only for that point. Since instability effects are at first disregarded, in determining the axial force distribution, we can write these equations as follows:

$$F_x^A = \frac{12EI}{L^2} u_1 - \frac{6EI}{L^2} \theta$$

$$F_x^B = \frac{AE}{L} u_1$$

$$F_z^A = \frac{AE}{L} w_1$$

$$F_z^B = \frac{12EI}{L^3} w_1 - \frac{6EI}{L^2} \theta$$

$$M_y^A = -\frac{6EI}{L^2} u_1 + \frac{4EI}{L} \theta$$

$$M_y^B = -\frac{6EI}{L^2} w_1 + \frac{4EI}{L} \theta$$

(IV-1)

This may not always be the case, however. Furthermore, the above simple problem represents the hemisphere, rather than the shallow spherical shell. To examine this more closely, a series of analyses was conducted for the structure shown in Figure IV-2 (with the same cross-sectional properties as before) and the accompanying table was constructed to indicate the % improvement over axial loads computed from "membrane theory"

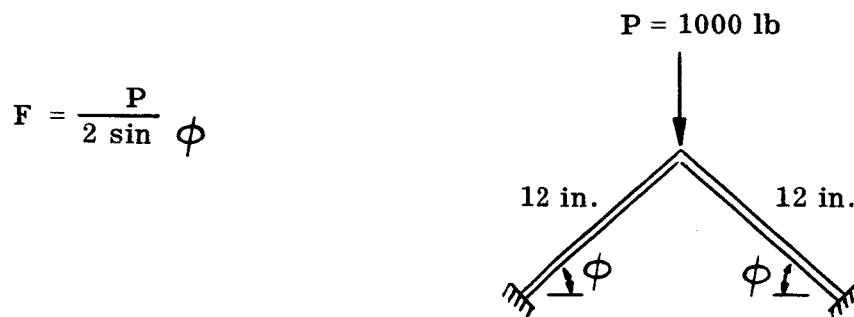


Figure IV-2. Frame for Numerical Analysis

TABLE IV-1
EXAMPLE FRAME RESULTS

Degrees	Uncoupled Membrane Flexure Behavior	Coupled Membrane Flexure Behavior	% Difference
45	707.0	702.2	0.8%
30	1000.0	980.0	2.0%
15	1932.0	1761.0	8.9%
5	5737.0	3008.0	47.5%

where

$$\textcircled{H} = \left(\frac{AE}{L} + \frac{12EI}{L^3} \right) \left[\left(\frac{AE}{L} + \frac{12EI}{L^3} \right) \frac{8EI}{L} - 2 \left(\frac{6EI}{L^2} \right)^2 \right] \quad (\text{IV} - 5)$$

Let us examine the improvement in the predicted element membrane forces which is realized by utilization of the above formulation rather than the "membrane" theory which is represented by

$$F = \frac{P}{2 \sin \phi} \quad (\text{IV} - 6)$$

Consider the case defined by

$$P_x = 1000 \text{ lb}$$

$$P_z = 0$$

$$M_y = 0$$

$$\phi = 45^\circ$$

From Equation IV-6 we have $F_x^B = 1000 \text{ lb}$. Alternatively, using the previously derived equations, we have

$$F_x^B = \frac{AE}{L} u_1$$

$$F_x^B = \frac{AE}{\Delta L} \left[\left(\frac{AE}{L} + \frac{12EI}{L^3} \right) \frac{8EI}{L} - \left(\frac{6EI}{L^2} \right)^2 \right] P_x$$

$$F_x^B = \frac{\left(1 - \frac{9I}{2\lambda AL^2} \right) P_x}{\left(\lambda - \frac{9I}{AL^2} \right)} \quad (\text{IV} - 7)$$

where

$$\lambda = \left(1 + \frac{12I}{AL^2} \right)$$

With $L = 12$ inches and with a square cross section, 1×1 , the result is

$$F_x^B = 995.7$$

Hence, the difference between this and the membrane solution is not significant. (0.5%)

Interpretation of these results for the elementary frame structure enables general conclusions to be drawn regarding the nature of discrete element idealizations of practical structures. Of primary interest is the demonstrated need for the consideration of membrane-flexure coupling. The importance of this consideration for shallow configurations of the example structure is apparent from the percentage error data shown in Table IV-1. Accordingly, interelement coupling of membrane and flexure behavior was incorporated in the instability analyses conducted for the Apollo heat shield structure. A detailed description of the instability analysis method developed is presented in Appendix C.

C. EVALUATION ANALYSES

Two classical problems have been solved with the subject discrete element approach to elastic instability analysis in order to verify its accuracy. One of the problems involves the prediction of the buckling pressure for a uniformly loaded circular arch. The other is concerned with the prediction of the deflections and the linear buckling of a pressurized spherical cap.

The first problem is illustrated in Figure IV-3. A circular arch, subtending an angle of 120° , is subjected to a uniform normal pressure (p , lb/in.). The arch is fully fixed at the ends and possesses a cross-sectional area A , a moment of inertia I , and is made of a material with a modulus of elasticity, E .

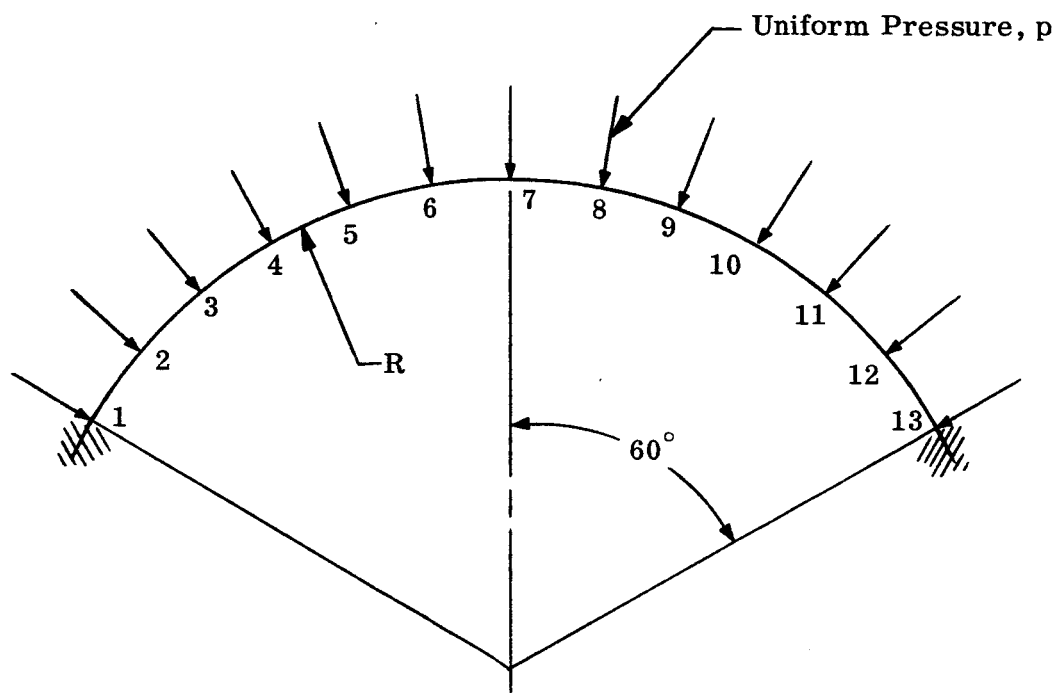
The arch was idealized as a system of 12 beam-column elements (Figure IV-3). The eigenvalue was computed to be

$$P_{cr} = 19.58 \frac{EAZ}{R}$$

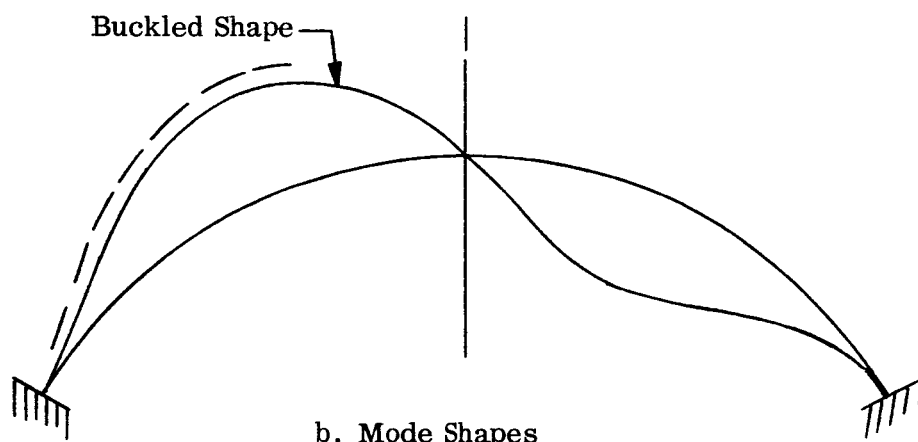
while the corresponding buckling mode was of the nonsymmetric form shown in Figure IV-3b.

This problem was solved by Wempner and Kesti, using classical techniques, in Reference 3. They obtain the solution

$$P_{cr} = 19.4 \frac{EAZ}{R}$$



a. Problem Data



b. Mode Shapes

Figure IV-3. Deep Arch - Uniform Pressure

which differs from the computed solution by less than 1%. Also, Wempner and Kesti predict a mode shape which is essentially identical with that shown in Figure IV-3b.

The close agreement between the numerical and theoretical results in this case indicates that the linearized discrete element method used here is indeed applicable to this class of problem. In this case, where the subtended angle is relatively large, the effects of large deflections (as characterized by terms of the type $1/2 \left(\frac{dw}{dx} \right)^2$) have only a secondary effect, and thus the linear theory is applicable. In very shallow arches, these large deflection terms, can assume dominant importance and an analysis disregarding such effects may yield a very poor approximation.

In order to check the validity and applicability of the discrete element method in the prediction of the buckling behavior of shallow spherical caps similar to the Apollo heat shield, experimental results obtained by Kaplan and Fung (Reference 4) were examined. They conducted a series of tests on shallow spherical caps subjected to uniform hydraulic or pneumatic pressure. In these tests, not only the critical pressures were obtained, but also the deflected shapes were measured in a number of cases up to collapse.

Their Specimen 21 was employed for the purposes of comparison. The principal dimensions and properties are indicated in Figure IV-4b. The cap is fully fixed at the edge and subject to air pressure.

In the numerical analysis, only one quadrant of the cap is considered. The gridwork used is shown in Figure IV-4b. For this shell, the critical pressure has been determined experimentally to be 34.40 psi. The deflected shape has been measured and is presented in Reference 4 for a pressure of $0.581 P_{cr}$. Thus, in the numerical analysis the loading has been taken as

$$0.581 \times 34.4 = 19.98 \text{ p.s.i.}$$

Using this pressure, the deflected form shown in Figure IV-4b was determined. The comparison between the experimental and theoretical results is excellent. In the same analysis an apparent buckling pressure of 63.1 psi was determined by an eigenvalue routine. Classical linear shell buckling theory yields a critical pressure

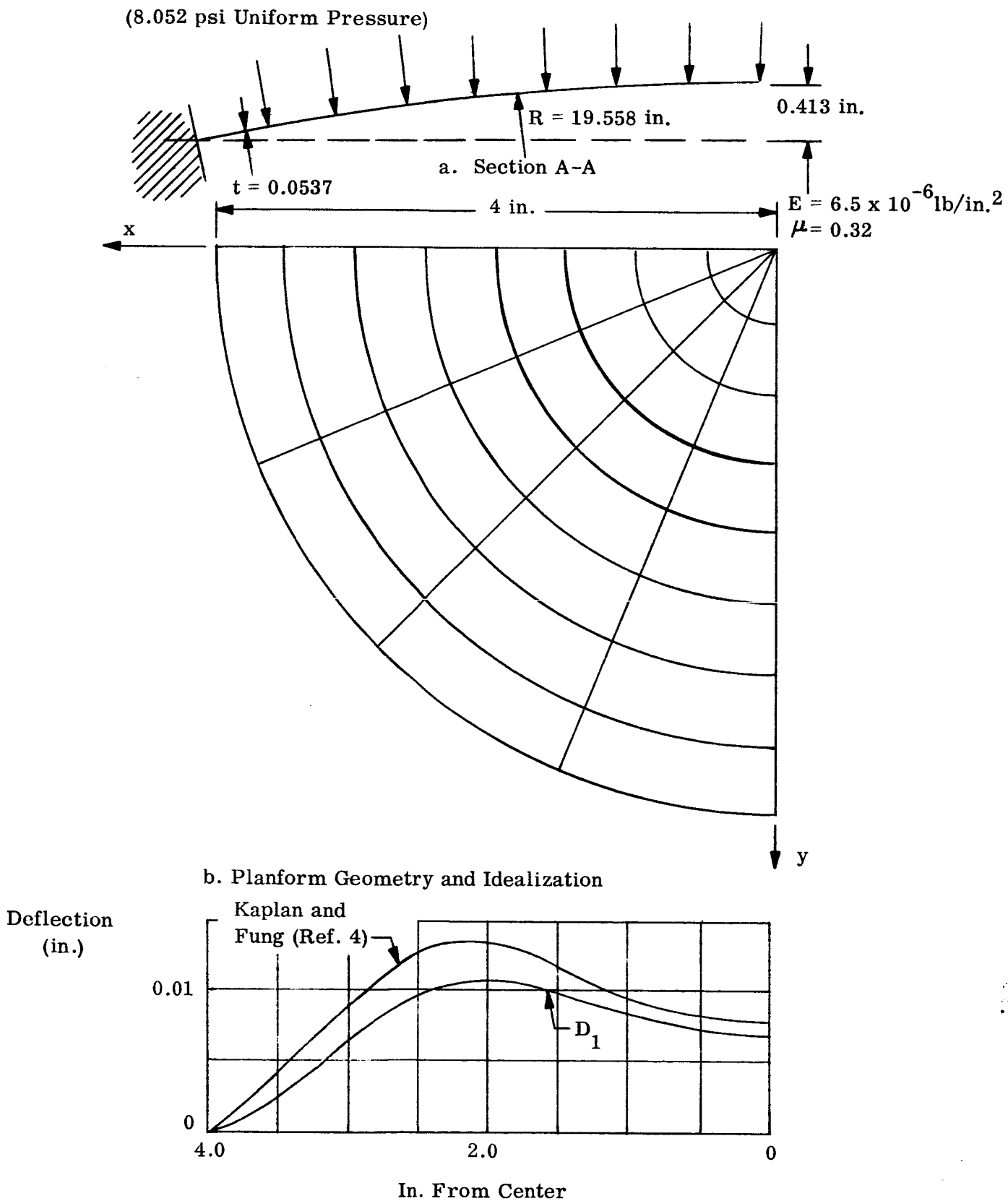


Figure IV-4. Spherical Cap - Uniform Pressure

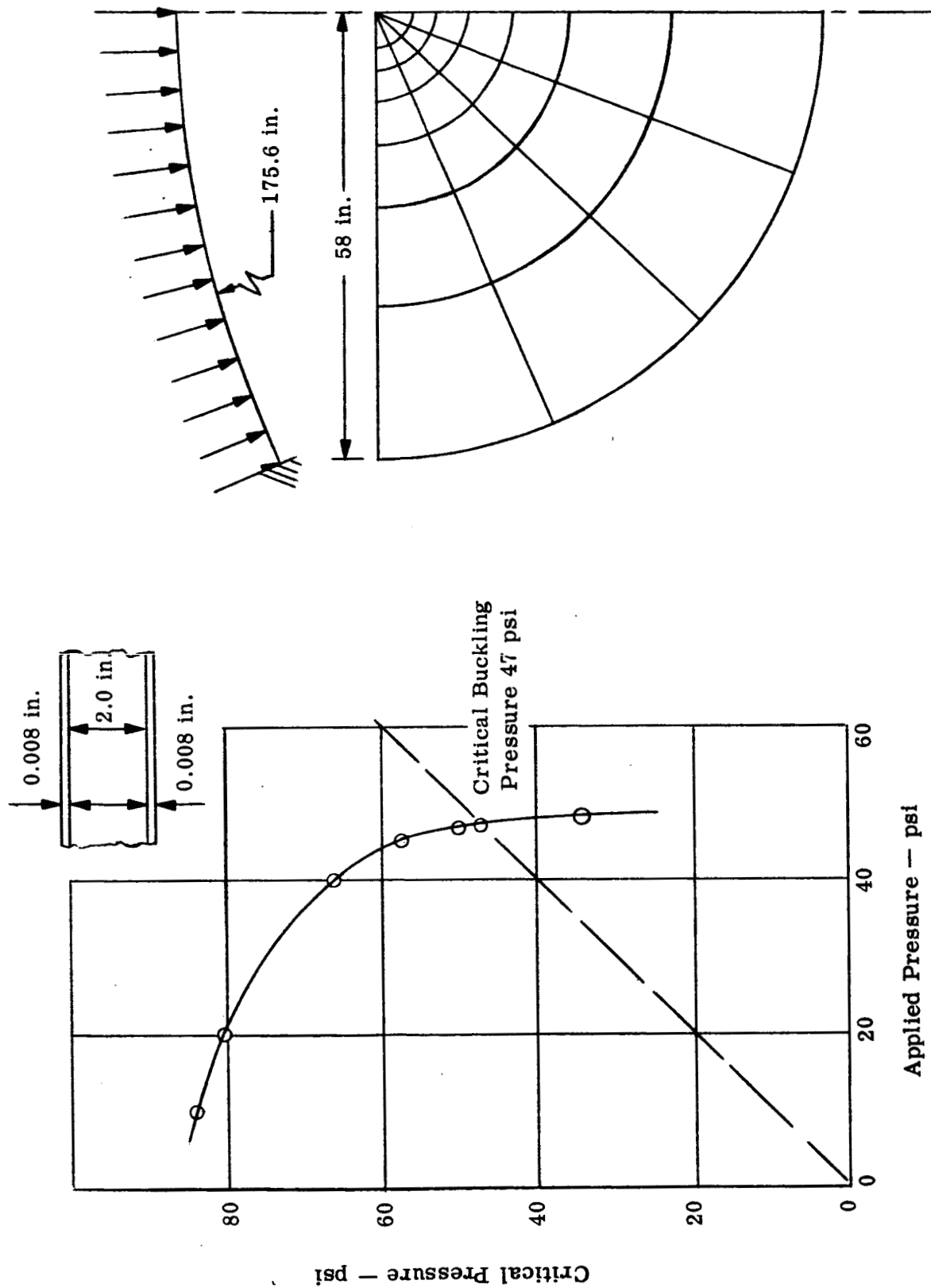


Figure IV-5. Heat Shield With Constant Face Thickness Uniform Pressure

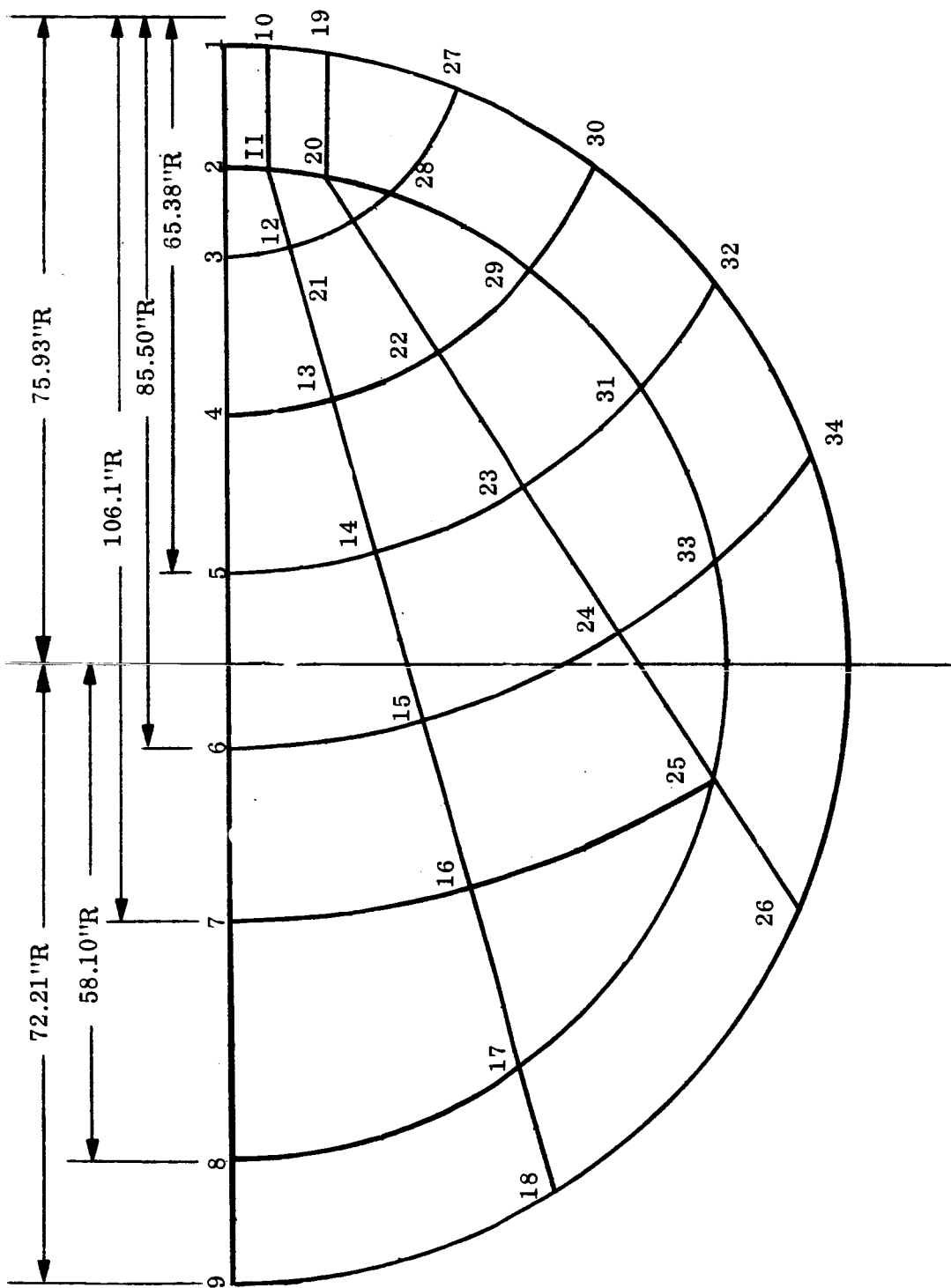


Figure IV-6. Gridwork for Instability Analyses of Heat Shield With Scalloped Faces

Gerard and Becker (Reference 5) have examined the comparison between experimental results and classical linear theory for this class of problem. Based upon the available test data, it is demonstrated that, due to the effects of initial imperfections and large deflections, the classical factor of 1.2 must be reduced. The amount of the reduction is dependent upon the R/t ratio, and for the present case of $R/t = 362$, the reduction factor is approximately 0.42. When the case of the sandwich heat shield is considered subsequently, a similar reduction factor is applied to the values obtained by the linearized numerical analysis to account for the effects of large deflections and initial imperfections.

D. ANALYSIS RESULTS

1. Idealized Heat Shield - Uniform Pressure

The first instability analysis, which was performed upon a structure representative of the actual Apollo heat shield, was intended to determine the critical uniformly distributed pressure which causes buckling of a spherical sandwich cap. The cap has the same dimensions, etc., as the heat shield except that the sandwich face sheets have a uniform thickness of 0.08 in. For the purposes of this analysis only one quadrant of the cap was considered. Full details of the cap and the gridwork are given in Figure IV-5.

The use of the matrix instability analysis concepts described in Appendix C take into account the simultaneous action of membrane and flexural stress systems, but the effects of flexural deformations on the element membrane strain-displacement equations are neglected. If then, in a problem, the membrane stress state undergoes a simple linear change in magnitude, but is not redistributed as the external applied load is varied linearly, then the critical buckling load of a system may be estimated reliably (ignoring large deflection terms) by factoring any applied load by an eigenvalue determined for that load level.

In the case of the spherical cap, the bending deformations cause redistributions of the membrane stresses. The redistributed membrane stresses alter the

bending stiffness, and thus it is necessary to iterate at each load level to determine the actual stress distributions. In order to find the actual value of the buckling load, it is therefore necessary to reach the situation in which the eigenvalue is unity; i.e., no extrapolation is required. The applied load is then the buckling load.

This condition may be reached by simple trial-and-error, but a more sophisticated approach is desirable. For the present case, a simple graphical technique was used initially, and based upon these results a mathematical approach was developed.

When the spherical cap was subjected to a uniform pressure of 10 psi, the apparent buckling load was computed as 84 psi (see Figure IV-5). Application of 20 psi yielded 81 psi, etc. The curve in Figure IV-5 shows the various applied loads. The intersection of the curve and the line $\lambda = 1$ indicates the critical value of the applied pressure as 47.0 psi. As discussed previously, this value must be reduced by a suitable factor to take account of large deflection effects. Curves giving this factor, presented in Reference 9 are based upon the radius-to-thickness ratio. For a sandwich panel, however, the definition of the thickness presents a problem, since face, core, or effective bending thicknesses may be used. Fortunately, in the region covered by these parameters, the curve of the reduction factor of Reference 4 is relatively flat and a mean value of approximately 50% may be selected. The critical uniform pressure for the idealized heat shield then becomes

$$p_{cr} = 0.5 \times 47.0 \approx 23.5 \text{ p.s.i.}$$

2. Actual Heat Shield - Water Impact Cases

In view of the iterative nature of the instability analysis it was decided to consider initially only three actual water impact cases. These are all for an impact angle of $\phi = 10^\circ$ and for the three radii of wetted area: $r = 10''$, $20''$, and $40''$. As discussed previously, the instability analyses utilize a considerably coarser gridwork than that used for the basic design analyses. The modified gridwork, which is shown in Figure IV-6, is based upon the polar grid of the design analyses (c.f., Figure III-5) and has approximately 150 degrees of freedom - the limit of the current instability program.

Figures IV-7 to IV-9 present the results of the three instability analyses. The buckling pressures determined from these curves are as follows:

Radius	10"	20"	40"
Pressure (psi)	1179.0	396	210

In the previous section, the concept of a reduction factor which accounts for the large deflection effects not included in the above analyses was introduced. The precise value of the factor is questionable but from data given in Reference it is estimated to be 0.5. From MSC data for the case of 35 ft/sec water impact velocity the pressures experienced at the appropriate radii can be compared with the above values after factoring by 0.5.

	<u>10"</u>	<u>20"</u>	<u>40"</u>
Factored Pressures	589.5	198.0	105.0
Estimated Pressure (MSC)	273.0	151.0	80.0
Safety Factor	2.16	1.31	1.31

From these figures it may be seen that an overall instability failure of the Apollo heatshield is not predicted.

E. FINITE DISPLACEMENT CONSIDERATIONS

Extension of the instability analysis to include finite deformation and finite displacement effects could be expected to improve significantly the prediction of shell behavior for certain shallow configuration and applied loading situations. Such an extension could be effected within the framework of the instability analysis procedure developed herein.

The behavior of a structure idealized as an assembly of discrete elements is characterized by the nature of the discrete element representations. Accordingly, in the development of a nonlinear formulation, attention may be focused on the derivation of appropriately nonlinear discrete element representations.

A nonlinear mathematical representation for a structural discrete element is most easily derived using the principle of stationary potential energy in conjunction

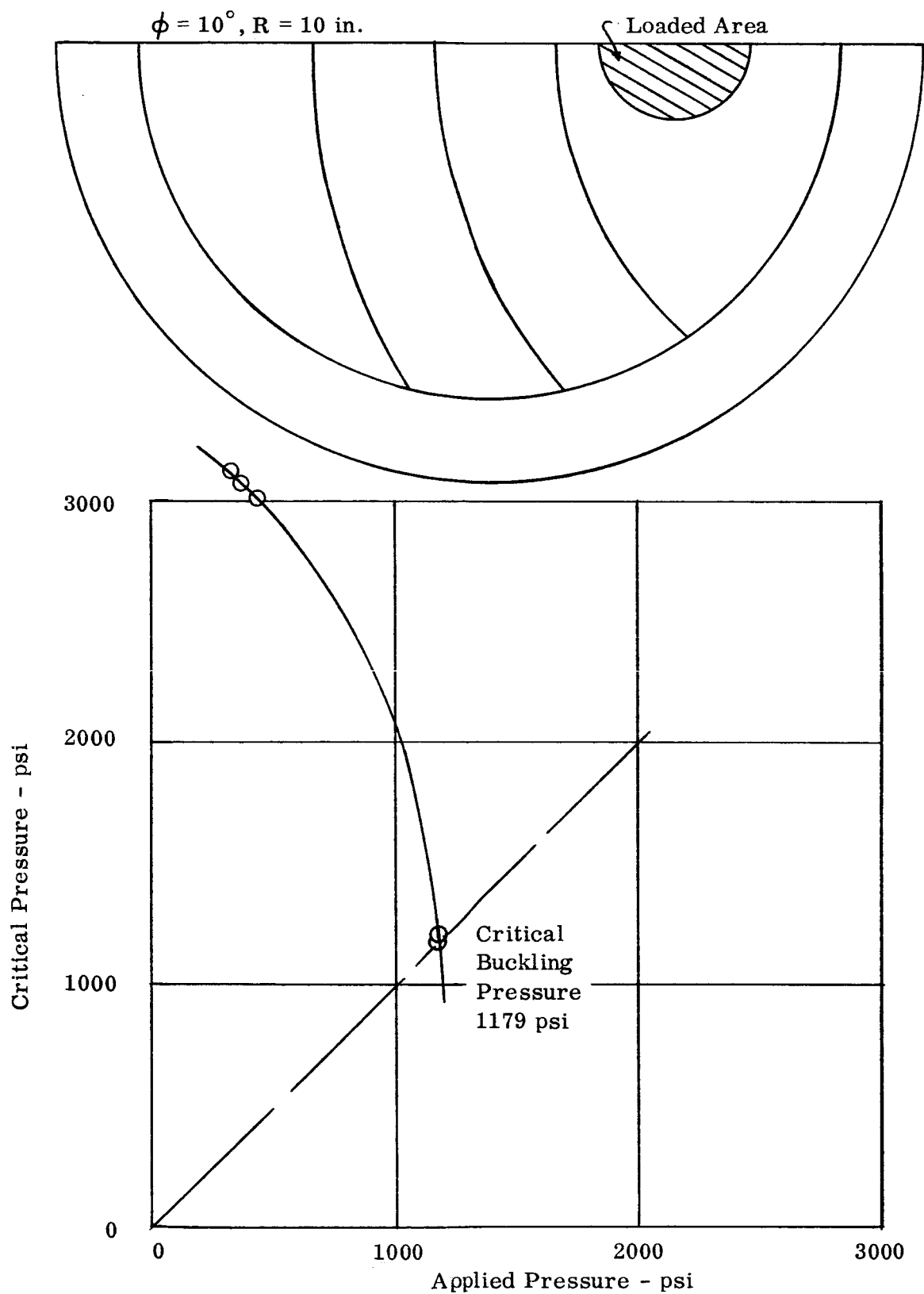


Figure IV-7. Heat Shield with Scalloped Face Thickness, 10 in. Radius Loaded Area, $\phi = 10^\circ$

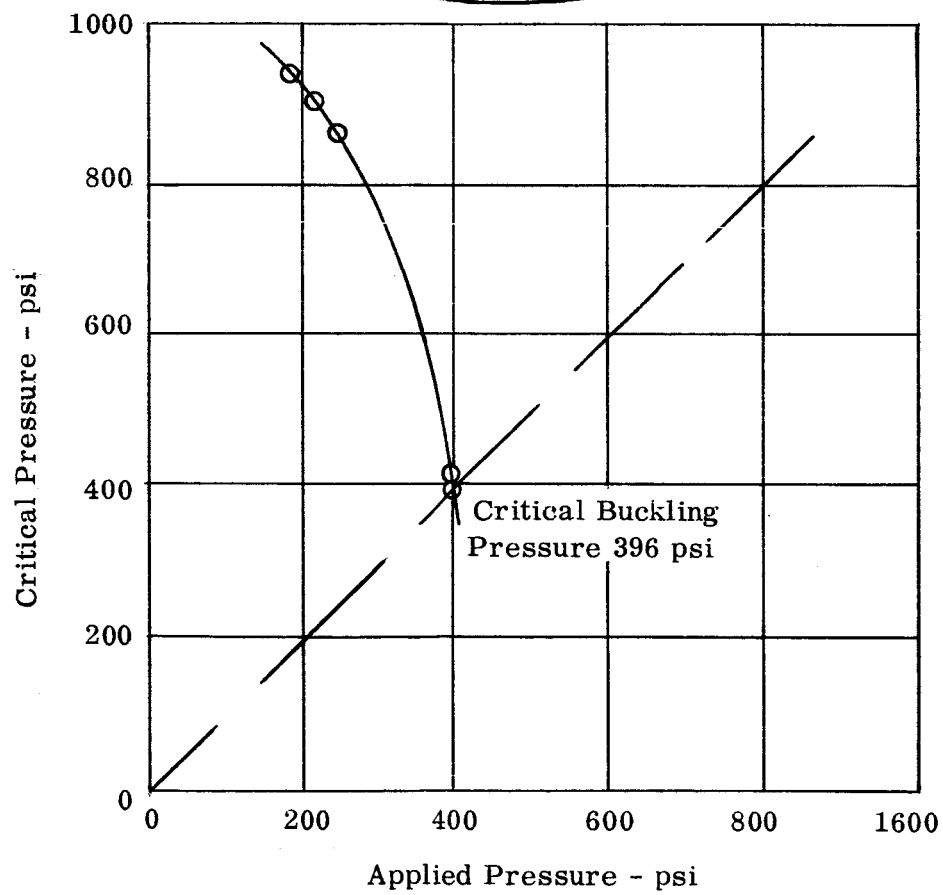
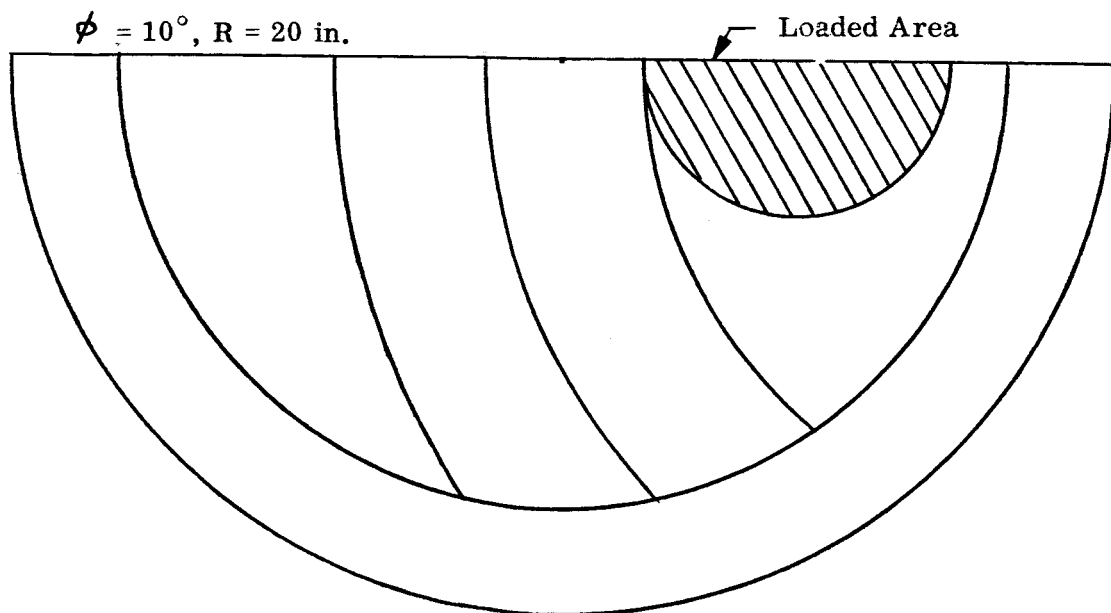


Figure IV-8. Heat Shield with Scalloped Face Thickness, 20 in. Radius Loaded Area $\phi = 10^\circ$

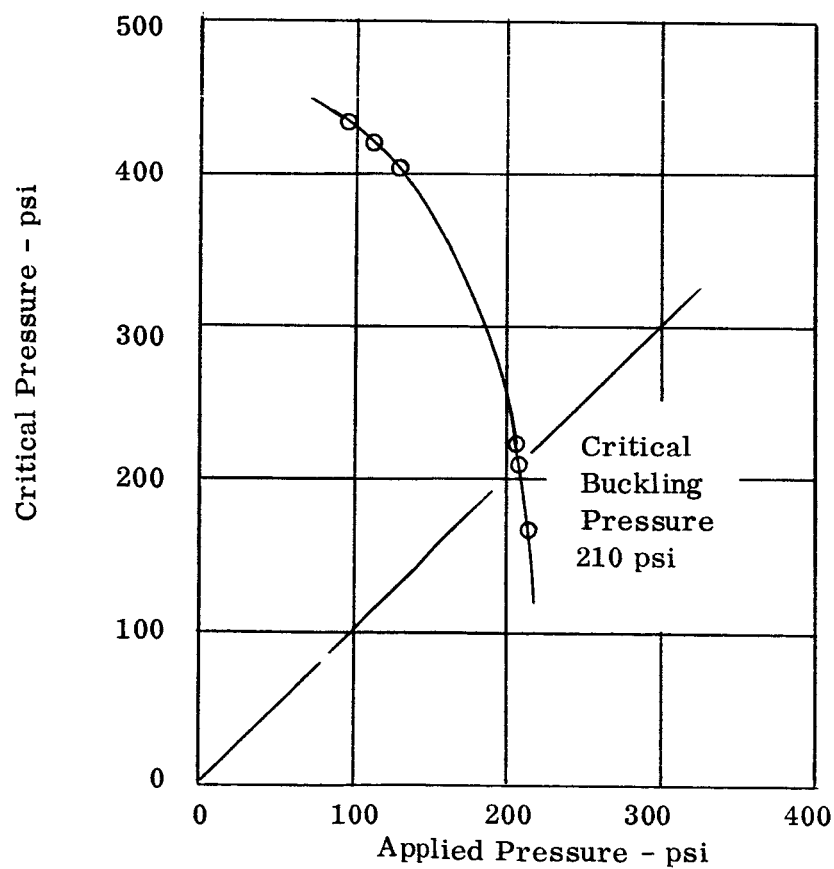
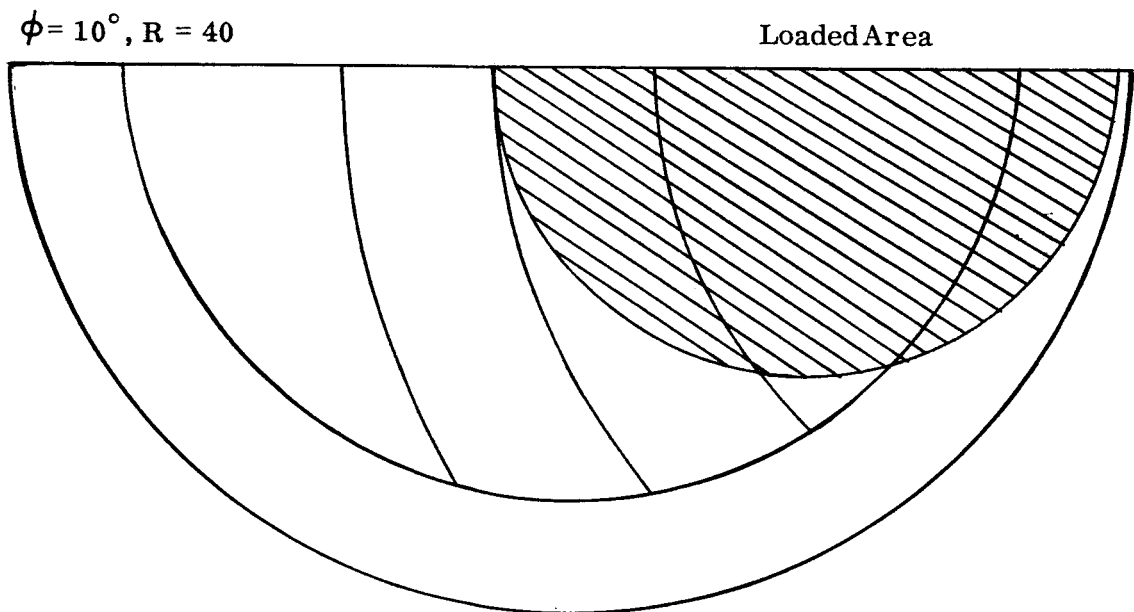


Figure IV-9. Heat Shield With Scalloped Face Thickness, 40 in. Radius
Loaded Area, $\phi = 10^\circ$

with the Rayleigh-Ritz procedure. In order to account for finite deformation and finite displacement effects, it is necessary to retain selected nonlinear terms in the element strain-displacement relations. For thin shell and slender prismatic structural components it suffices to include second order terms in the transverse displacement functions. The retention of quadratic terms in the strain-displacement relations results in a quartic potential energy functional. Construction of displacement functions in accordance with the Rayleigh-Ritz procedure and execution of the variation of the quartic potential energy yields a discrete element representation in the form of a set of nonlinear algebraic equations which may be written as:

$$\{F_e\} = [k_e]\{\Delta_e\} + [n_{1e}]\{\Delta_e\} + [n_{2e}]\{\Delta_e\}$$

where

$\{F_e\}$ is the vector of forces applied to the element at the node points.

$\{\Delta_e\}$ is the corresponding vector of node point displacements.

$[k_e]$ is the familiar element stiffness matrix.

$[n_{1e}]$ is defined as the "first order element incremental stiffness matrix". Its elements are linear functions of the element node point displacements.

$[n_{2e}]$ is defined as the "second order element incremental stiffness matrix". Its elements are quadratic functions of the element node point displacements.

It is instructive to exhibit the incremental stiffness matrices for a frame discrete element appropriate to the elementary frame structure considered previously (Figure IV-2).

$$[n_{1e}] = EAL \begin{bmatrix} 0 & \frac{3}{5L^3}w_a - \frac{\theta_a}{20L^3} & \frac{3w_a}{5L^3} & -\frac{w_a}{20L^2} + \frac{\theta_a}{15L} \\ -\frac{w_a}{20L^2} + \frac{\theta_a}{15L} & \frac{3w_a}{5L^3} & -\frac{w_a}{20L^2} & \frac{w_a}{15L} \end{bmatrix}$$

Symmetric

$$[n_{2e}] = EAL \begin{bmatrix} 0 & \frac{18}{25L^4}w_a^2 - \frac{3}{25L^3}w_a\theta_a + \frac{3}{100L}\theta_a^2 & \frac{3}{100L}w_a^2 - \frac{w_a\theta_a}{75L} + \frac{\theta_a^2}{125} \\ 0 & -\frac{3}{50L^2}w_a^2 + \frac{3}{50L}w_a\theta_a - \frac{\theta_a^2}{150L} & \frac{3}{100L}w_a^2 - \frac{w_a\theta_a}{75L} + \frac{\theta_a^2}{125} \\ 0 & -\frac{3}{50L^2}w_a^2 + \frac{3}{50L}w_a\theta_a - \frac{\theta_a^2}{150L} & \frac{3}{100L}w_a^2 - \frac{w_a\theta_a}{75L} + \frac{\theta_a^2}{125} \end{bmatrix}$$

The approach to incorporating finite deformation and finite displacement effects outlined above is readily applicable to the thin shell elements appropriate to the heat shield analysis as well as the frame element considered here. A further important feature of this method is that the numerical algorithm required for the prediction of behavior is conceptually unchanged though revisions might be necessary to obtain favorable convergence characteristics.

In a review of the work described earlier, Budiansky and Sanders (Reference 18), strongly urge the performance of nonlinear deflection analyses and present a theoretical extension of discrete element concepts to accomplish this end. Their suggestions parallel the above procedures to a significant extent.

V. DISCRETE ELEMENT PROPERTIES

A. HISTORICAL BACKGROUND

In order to place this portion of the study in proper perspective, a brief historical review is given of the development of the discrete element approach to structural analysis.

The concept of physically idealizing complex structures as assemblies of discrete structural elements has been known and utilized for over 100 years, in the form of procedures for truss and frame analysis. The potential value of this approach as a means for the analysis of structural continua such as plates and shells remained unrecognized until the early 1950's. Then, a large number of papers, were published which clarified and refined the concept of discrete element structural idealization and generalized the analysis procedures associated with such concepts. A landmark paper in this connection is that by Turner, et al (Reference 6). Numerous development efforts were initiated to construct discrete element formulations suitable for realistic idealization of a wide variety of practical structures.

Many mathematical models were derived for a number of discrete structural elements using several distinctly different approaches. The single aspect common to the various investigations was a general inattention to the convergence characteristics of the discrete element representations put forward. Most element representations were found to exhibit satisfactory convergence while others proved useless in the absence of favorable convergence characteristics. Through a heuristic process, general analysis capabilities of broad applicability were developed by building up computer program libraries of the best discrete elements.

In 1963, Melosh (Reference 7), laid down guidelines, based on established principles of structural mechanics, for achieving convergent discrete element representations. The definition of procedures for developing element representations within the confines of these guidelines proved to be an elusive goal. As a consequence, the huge strides made in the development of additional and improved discrete element representations continued to stem from the heuristic process.

Only recently, in October of 1965, several investigators (8, 9, 10) have presented preliminary reports defining general systematic procedures for deriving convergent representations for a broad class of discrete structural elements. Those which are pertinent to heat shield analysis will be discussed subsequently.

B. SANDWICH ELEMENT

Prior to the initiation of this study, stiffness equations for the triangular sandwich element (Figure V-1) had been formulated at Bell Aerosystems Company. This element consists simply of upper and lower faces which are the conventional triangle in plane stress (Reference 6), separated by a core which carries only vertical shear stress. By combining these components to form a single element, including the condition that normals at a corner point remain normal during deformation, one obtains the desired stiffness properties.

Since the heat shield is indeed a sandwich structure, it would appear that this element would furnish a superior representation to that given by the isotropic plate elements. In order to test this conjecture, analyses of a quadrant of the heat shield were performed for two gridworks as shown in Figure V-2, a coarse mesh consisting of 28 sandwich elements and possessing 64 degrees of freedom, and a refined mesh consisting of 66 triangular sandwich elements and 156 degrees of freedom. This heat shield representation is assumed to have fixed support around the periphery along the bolt circle.

In both analyses, the face thickness was 0.008 in. and the core thickness was 2.00 inches. The modulus of elasticity for the faces was 30×10^6 psi while the core shear modulus, G_c , was taken as 1.8×10^4 psi.

For comparison purposes, a refined gridwork analysis was performed utilizing quadrilateral and triangular plates, in the same manner as was described in Section II. A comparison of the results of all three analyses is shown in Figure V-3, in the form of the centerline radial displacement profiles.

Since the conventional plate representation is known to yield essentially convergent results for the heat shield for this degree of gridwork refinement, it is

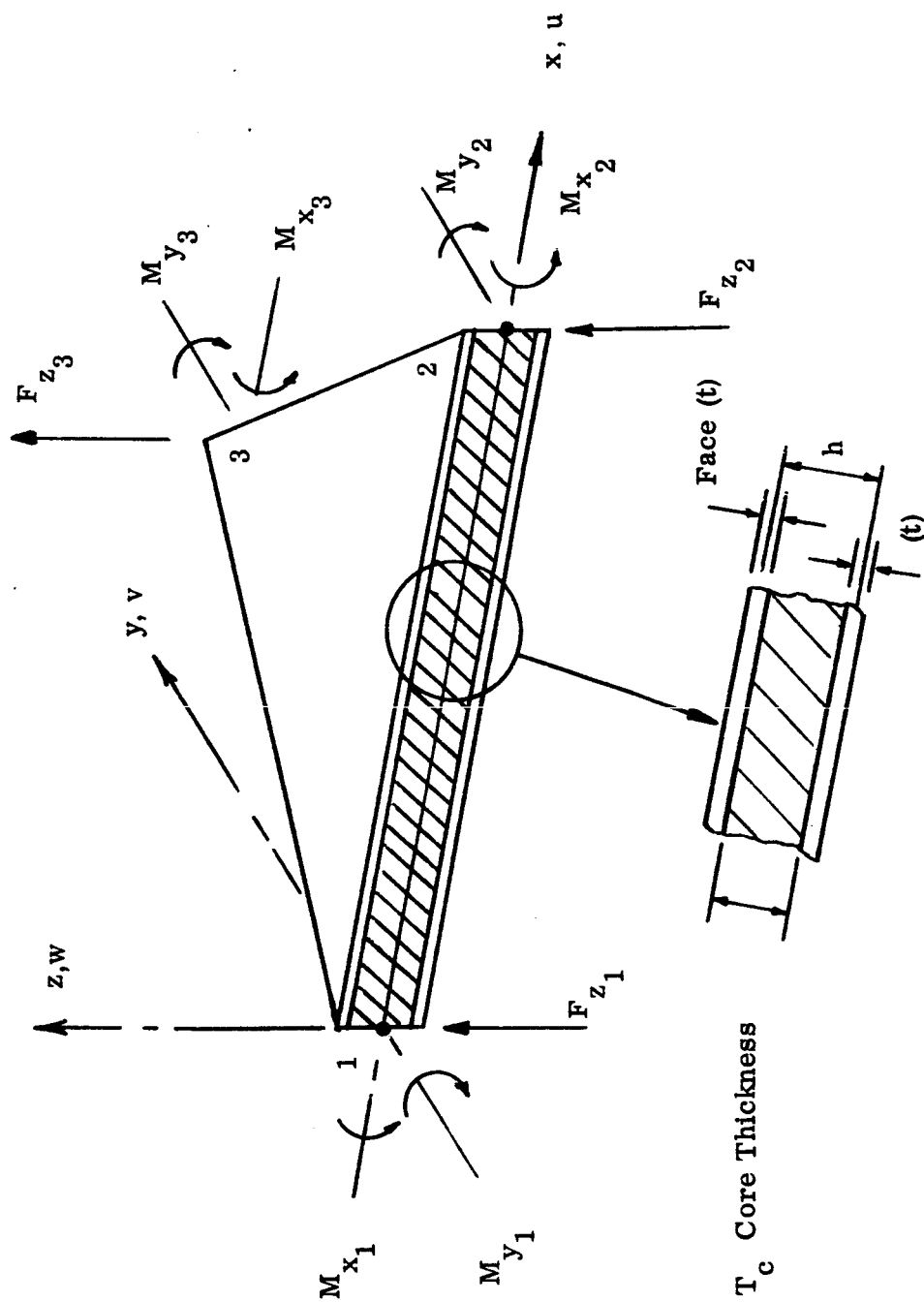
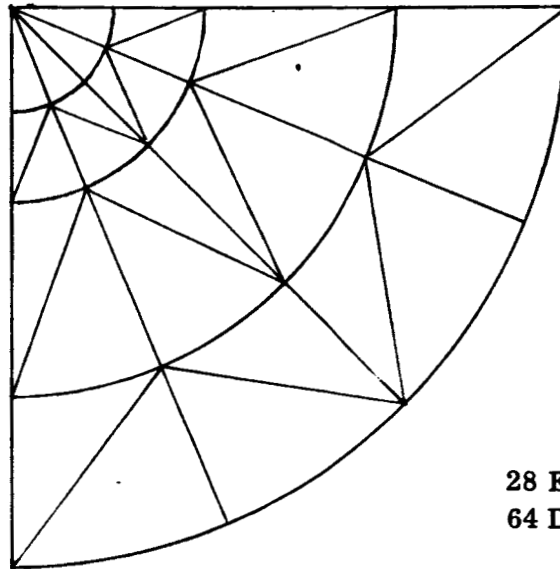
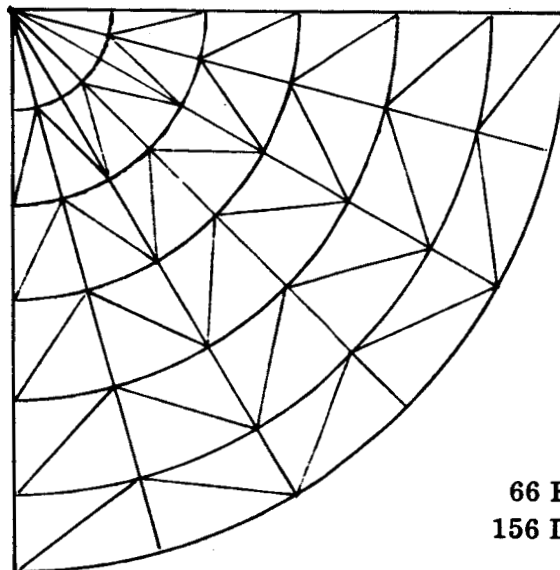


Figure V-1. Triangular Sandwich Plate Element



28 Elements
64 Degrees of Freedom

A. Coarse Gridwork



66 Elements
156 Degrees of Freedom

B. Fine Gridwork

Figure V-2. Heat Shield Quadrant Triangular Sandwich Panel

apparent from Figure V-3 that a significant improvement is yet to be gained, through gridwork refinement, in the triangular sandwich element representation. On the other hand, the substantial improvement obtained by advancing the gridwork from coarse to fine indicates that the triangular sandwich element will be capable of yielding accurate results with sufficient refinement.

The triangular sandwich element differs from the conventional plate element principally in the inclusion of a transverse shear flexibility. Consequently, the foregoing results prompted an examination of the relationship between core shear rigidity, G_1 , and gridwork size for a known solution. The problem chosen for examination was the simply-supported, uniformly loaded square plate shown in Figure V-4. The faces are taken to be 0.005 in. with a modulus of elasticity of 10^7 psi. The core depth is assumed to be 1.0 in.

Due to symmetry, only a quadrant of the plate need be analyzed. Three gridworks of elements have been utilized - 4, 16, and 64 elements. Analyses were performed for three values of core shear rigidity: 34,000 psi, 500,000 psi, and 3000 psi. The lowest value is the magnitude to be anticipated of conventional forms of sandwich construction. The high value is representative of an isotropic shape.

The results of the analyses, in the form of the center deflection, are plotted as a function of gridwork refinement. Also shown are results obtained by means of the classical solutions derived in Reference 11. It is seen from these results that a good level of agreement exists for the weak core shear rigidity, while the agreement is very poor in the modeling of an isotropic plate. Agreement for the latter is improved by refinement of the gridwork but whether or not the refinement will lead to a solution convergent upon the analytical solution is uncertain. Clearly, convergence will occur with only an inordinate degree of refinement.

Thus, it is seen from the foregoing results that the triangular sandwich element furnishes workable results for a reasonable number of elements when the structure indeed evidences sandwich behavior. A sandwich form of construction may or may not evidence "sandwich behavior", i.e., significant shear deformation, depending upon the span, loadings, etc.

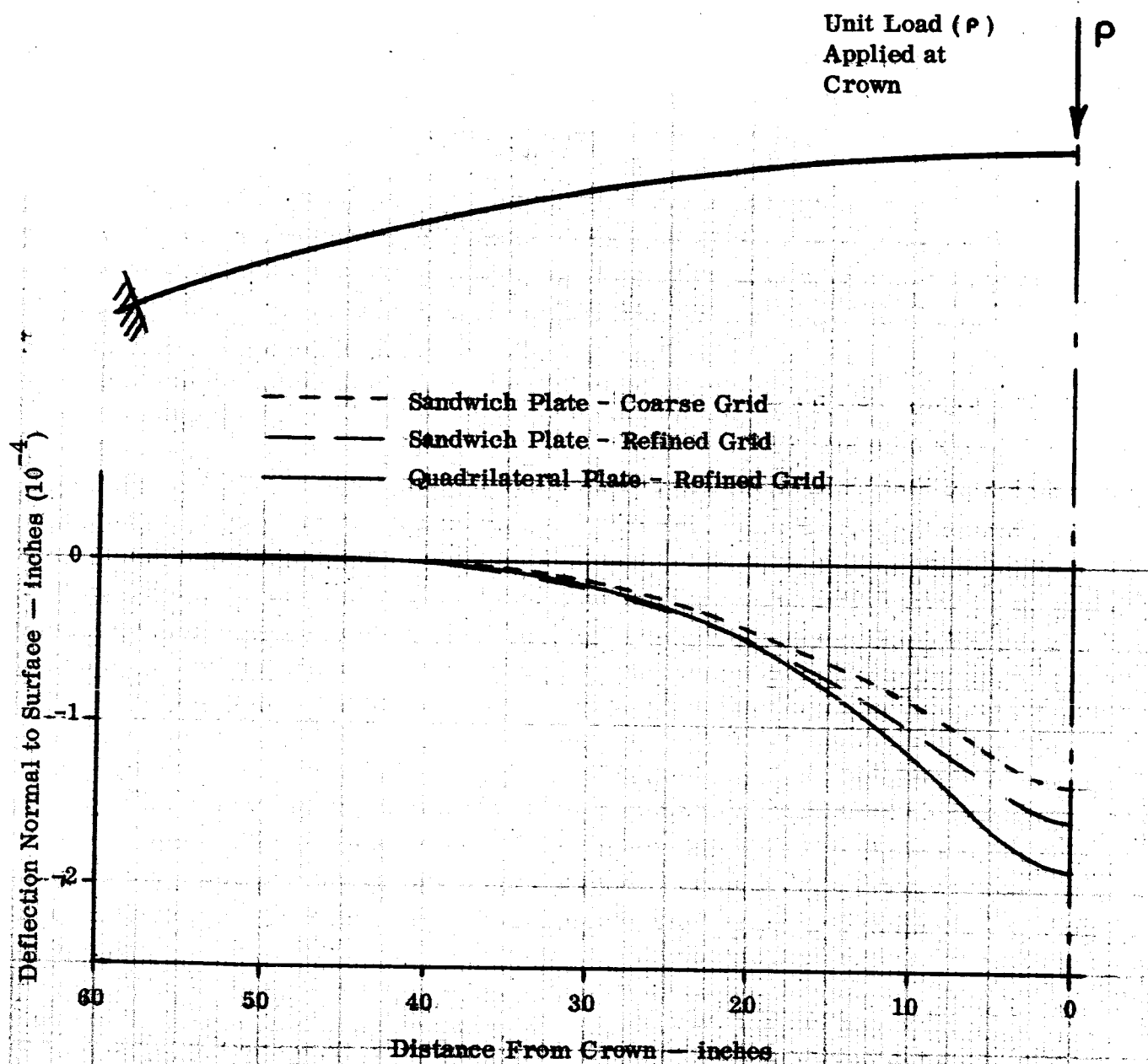


Figure V-3. Comparison of Results - Deflection Along Centerline Due to a Unit Load Applied at the Crown

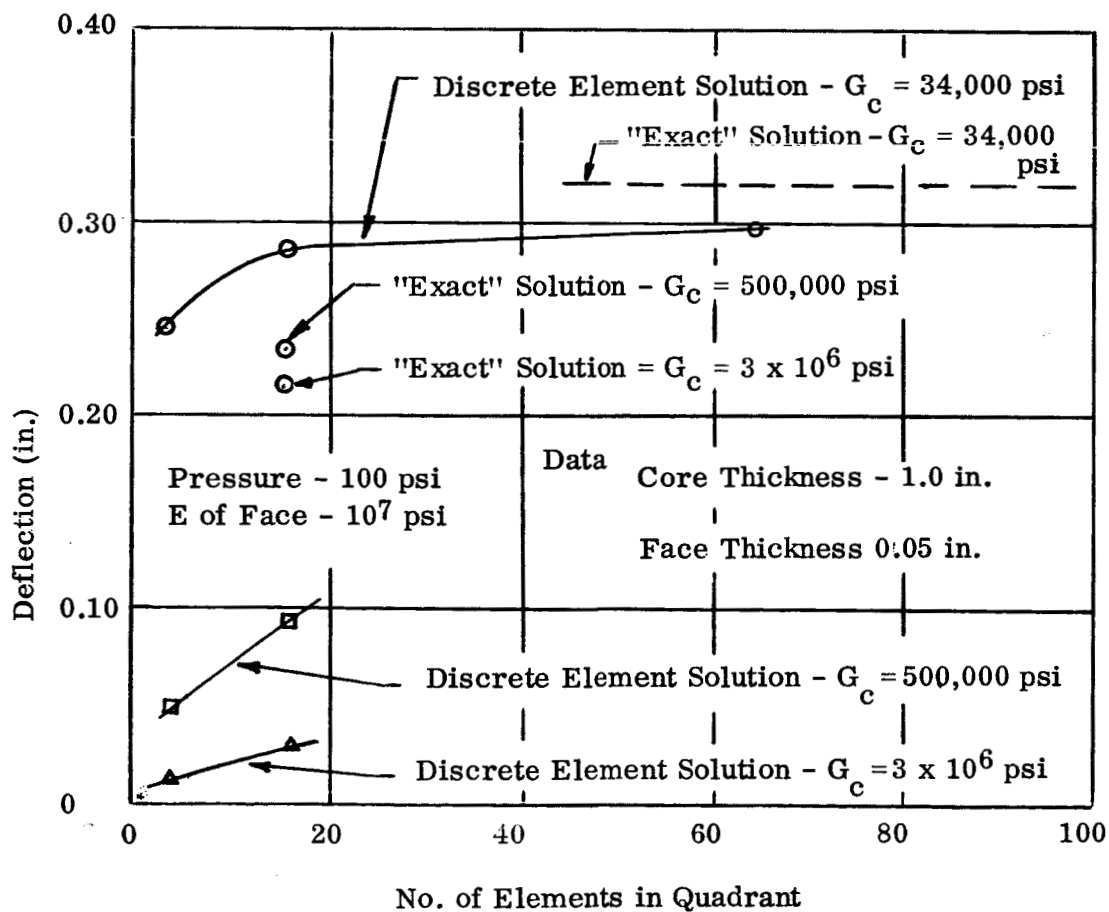
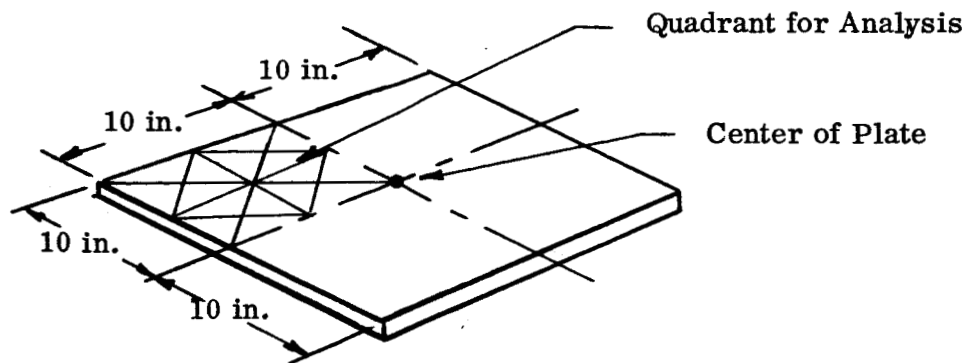


Figure V-4. Deflection Predictions versus Gridwork Refinement for Various Core Shear Rigidities

The use of plate elements based on conventional isotropic plate flexure theory, which neglects shear deformation, has been justified by the view that the Apollo Aft Heat Shield has a relatively rigid core and a large span, so that the shear deformations are negligibly small when compared with those due to bending. In order to provide a quantitative estimate of the error produced by these assumptions, the case of a square sandwich plate was examined. The cross-sectional dimensions are taken to be similar to those of the Apollo Aft Heat Shield and are given in Figure V-5. Using curves generated in Reference 12 for rectangular sandwich panels, the maximum (central) deflections for square panels of various sizes were obtained and compared with the classical values for isotropic plates having the same bending stiffness. The percentage error is plotted in Figure V-5.

For the heat shield, which is equivalent to a square plate of about 100 inches side length, the error is approximately 0.5%.

A convenient rule is to regard the error as negligible for $D_p' > 100$ where

$$D_p' = \frac{b^2 D_4}{12^2 D_5}$$

D_4 = shear stiffness

D_5 = flexural stiffness

b = panel width

The curve of D_p' for various panel widths is plotted on Figure V-7. It can be seen that for $D_p' = 100$ the error is approximately 2%.

C. INTERELEMENT COMPATIBLE ELEMENTS

As noted previously, rapid strides are being made in both the development of discrete element stiffness properties and in the definition of appropriate bases and concepts for the development of these properties. It is felt that these activities point towards idealization concepts which meet all of the needs of heat shield analysis. The numerical evaluation and coding of these elements, however, has not advanced sufficiently far at this time to permit analysis of the Apollo Aft Heat Shield.

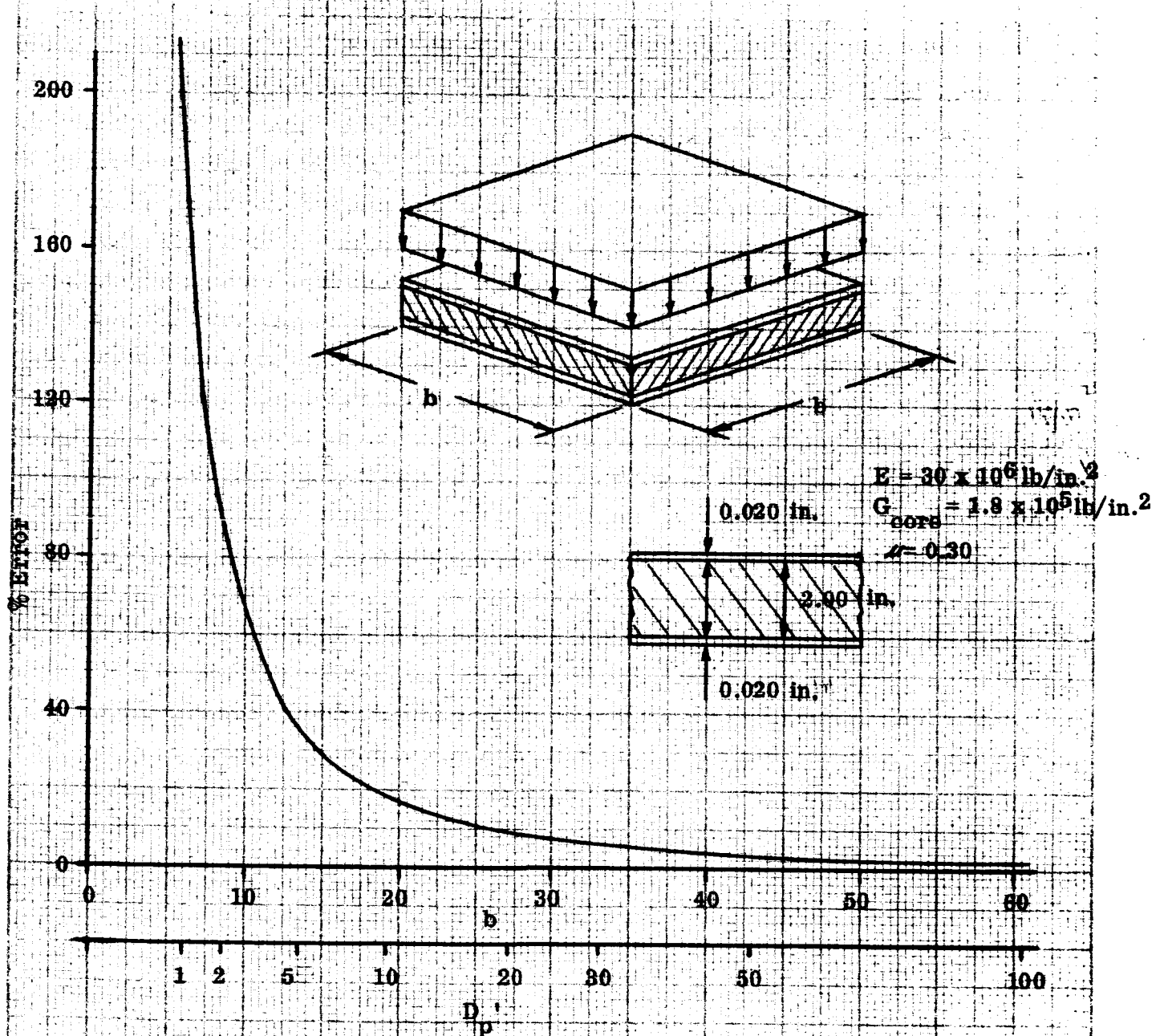


Figure V-5. Error in Central Deflection Due to Neglect of Shear Deformation

It is believed that discrete element idealizations for matrix displacement analysis should conform to the requirements of compatible displacement. If they meet these requirements, then it is assured that the displacement predictions will be smaller than the convergent solution and that the solution will monotonically approach the latter as the gridwork is refined in a consistent manner. Since discrete element formulations for matrix displacement analysis are generally based upon assumed displacement functions, there is no question regarding the satisfaction of compatibility within the elements; the problem is one of so-contriving the respective element displacement functions so that the complete model satisfies compatibility. That is, interelement compatibility must be achieved.

The element discussed previously - the triangular sandwich element - satisfies the interelement compatibility conditions. As shown, however, a very large number of these elements is necessary for an accurate representation. Thus, a more efficient approach is to utilize elements whose theoretical basis corresponds to that of conventional flexure theory, modified to account for the difference between membrane and flexural stiffness. Such elements are described in the following.

From the standpoint of geometric representation, two geometric forms are essential - the triangle and the arbitrary quadrilateral. Advanced representations have recently (October 1965) been put forward for both of these forms. The advancement which the new quadrilateral and triangular plate flexure elements represent stems from a careful construction of the element displacement modes so as to satisfy completeness and geometric admissibility requirements with respect to the whole structure. Satisfaction of these requirements guarantees that the mathematical model represents a stiffer structure than the actual structure in the sense that it has a higher potential energy than the exact solution. Furthermore, as the number of degrees of freedom are increased (e.g., grid refinement) the solution will converge monotonically toward the exact solution.

Suitable displacement behavior is described in the case of the quadrilateral element by defining a complete cubic polynomial mode shape over each of four zones (Figure V-6).

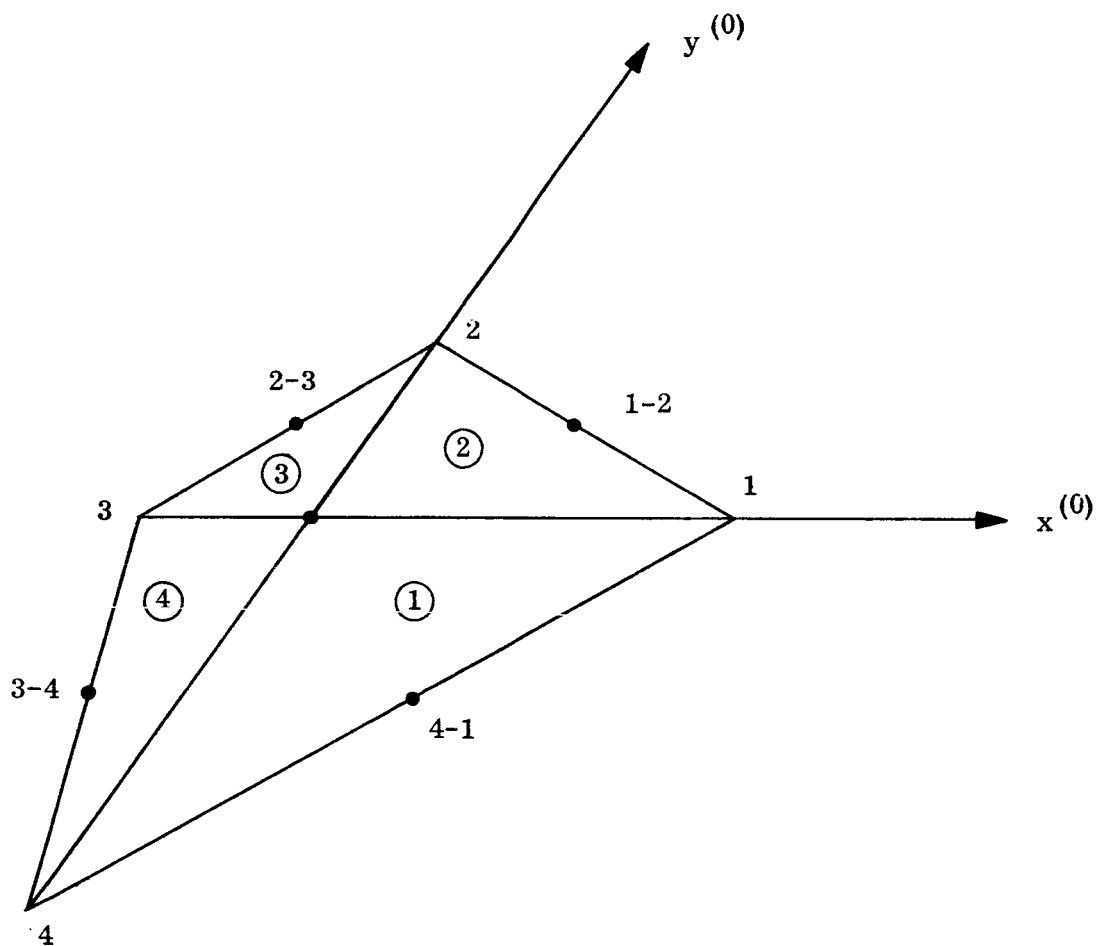


Figure V-6. Quadrilateral Plate Flexure Element

A total of ten coefficients are associated with each zone. Admissibility requirements across zone interfaces reduce the total number of undetermined coefficients to sixteen. This is precisely the number needed to establish geometric admissibility across element interfaces. This is clear since the displacement along any line is cubic in a coordinate measured along the line and is, therefore, completely specified along the boundary, by the corner point displacements and slopes. Thus, displacement compatibility is established by the interelement matching of these quantities. The four undetermined coefficients which remain are needed to satisfy slope continuity across element interfaces. The slope along any line is quadratic in a coordinate measured along the line and requires, therefore, the specification of slope at one point along an element boundary in addition to the two corner points. The boundary midpoint are selected for computational convenience. The resulting quadrilateral flexure element has sixteen degrees of freedom manifest as one displacement and two rotations at each of the four corners and one rotation at the midpoint of each boundary.

Completion of the formulation is effected in accordance with the well known Rayleigh-Ritz procedure. Substantial algebraic convenience is realized by the use of the oblique element coordinate shown in Figure V-6. Numerical evaluation of this advanced quadrilateral flexure element is being pursued at Bell Aerosystems Company.

Complete, admissible displacement mode shapes for a triangular plate flexure element have been constructed using a procedure similar to that just described for the advanced quadrilateral element. As before, complete cubic polynomial mode shapes are assumed over zones of the element (Figure V-7). Continuity requirements across zone interfaces reduce the total number of undetermined coefficients to twelve. Arguments identical to those given for the quadrilateral element associate these coefficients with the nine corner point displacements and rotations and a rotation at each of the three boundary midpoints. This advanced triangular element

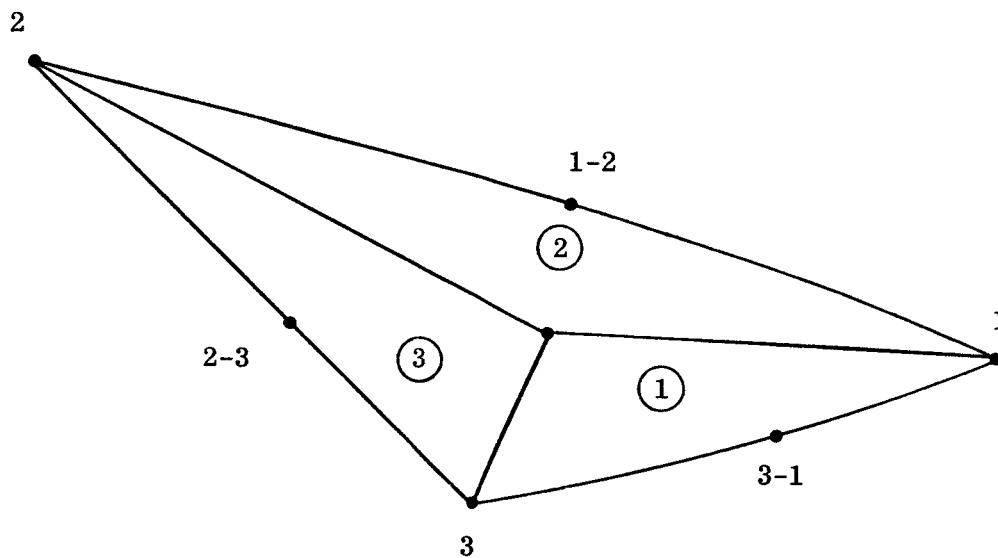


Figure V-7. Triangular Plate Flexure Element

will, like the quadrilateral element, be incorporated into the Bell general structural analysis program.

In conclusion, it is important to note that, not only are these triangular and quadrilateral flexure elements interelement compatible among other elements of their respective types, but quadrilateral elements may be interspersed with triangular elements without violation of interelement continuity requirements.

VI. ANALYTICAL SOLUTIONS

A. GOVERNING EQUATIONS

During the period when intensive efforts were directed toward the resolution of critical problems in the design of the Apollo heat shield for water impact conditions, the validity of the alternate paths toward numerical solutions for these problems was questioned. Thus, it becomes evident that classical solutions to simplified (but pertinent) problems were needed to verify that numerical analysis approaches. Furthermore, classical solutions can give a rapid, if approximate, measure of the quantities sought. The availability of convenient solutions will facilitate rapid analyses in the event new critical problems arise, and provide a means for preliminary design of future heat shields. With these considerations in mind, a portion of the work was devoted to the development of analytical solutions for a variety of heat shield problems. For the Apollo heat shield water impact cases, the loading is not axisymmetric. Also, the effects of a sandwich type of structure must be included. As discussed elsewhere, the shear deformations of the sandwich core may be neglected (in view of the comparatively large span) and the sandwich solution is then similar to that for a uniform plate except that the membrane and bending stiffnesses differ and are represented by the parameters D_m and D_s .

With these considerations, the governing differential equations are

$$\nabla^4 \left(\frac{F}{D_s} \right) + \frac{\ell}{\alpha_s} \frac{D_m}{D_s} \nabla^2 \left(\frac{w}{\ell} \right) = 0 \quad (\text{VI-1})$$

$$\nabla^4 \left(\frac{w}{\ell} \right) - \frac{1}{\alpha_s \ell} \nabla^2 \left(\frac{F_s}{D_s} \right) = \frac{p}{\ell D_s} \quad (\text{VI-2})$$

where F is a stress function, $\ell^4 = \frac{\alpha_s^2 D_s}{D_m}$, and the other symbols are defined in Figure VI-1. These equations were derived by E. Reissner (References

The homogeneous solutions to Equations (VI-1) and (VI-2) are taken as:

$$\frac{w_h}{\ell} = B_{01} \text{ber } x - B_{02} \text{bei } x + A_{03} + \sum_{n=1}^{\infty} [B_1 \text{ber}_n x - B_2 \text{bei}_n x + A_1 x^n] \cos n\theta \quad (\text{VI-3})$$

$$\frac{F_h}{D_s} = -\sqrt{\frac{\ell^4 D_m}{D_s}} \{ B_{02} \text{ber } x + B_{01} \text{bei } x + \sum_{n=1}^{\infty} [B_2 \text{ber}_n x + B_1 \text{bei}_n x + A_2 x^n] \cos n\theta \} \quad (\text{VI-4})$$

It is seen that for $\ell > 0$ there are basically four arbitrary constants to be determined. These can be obtained from the following boundary conditions.

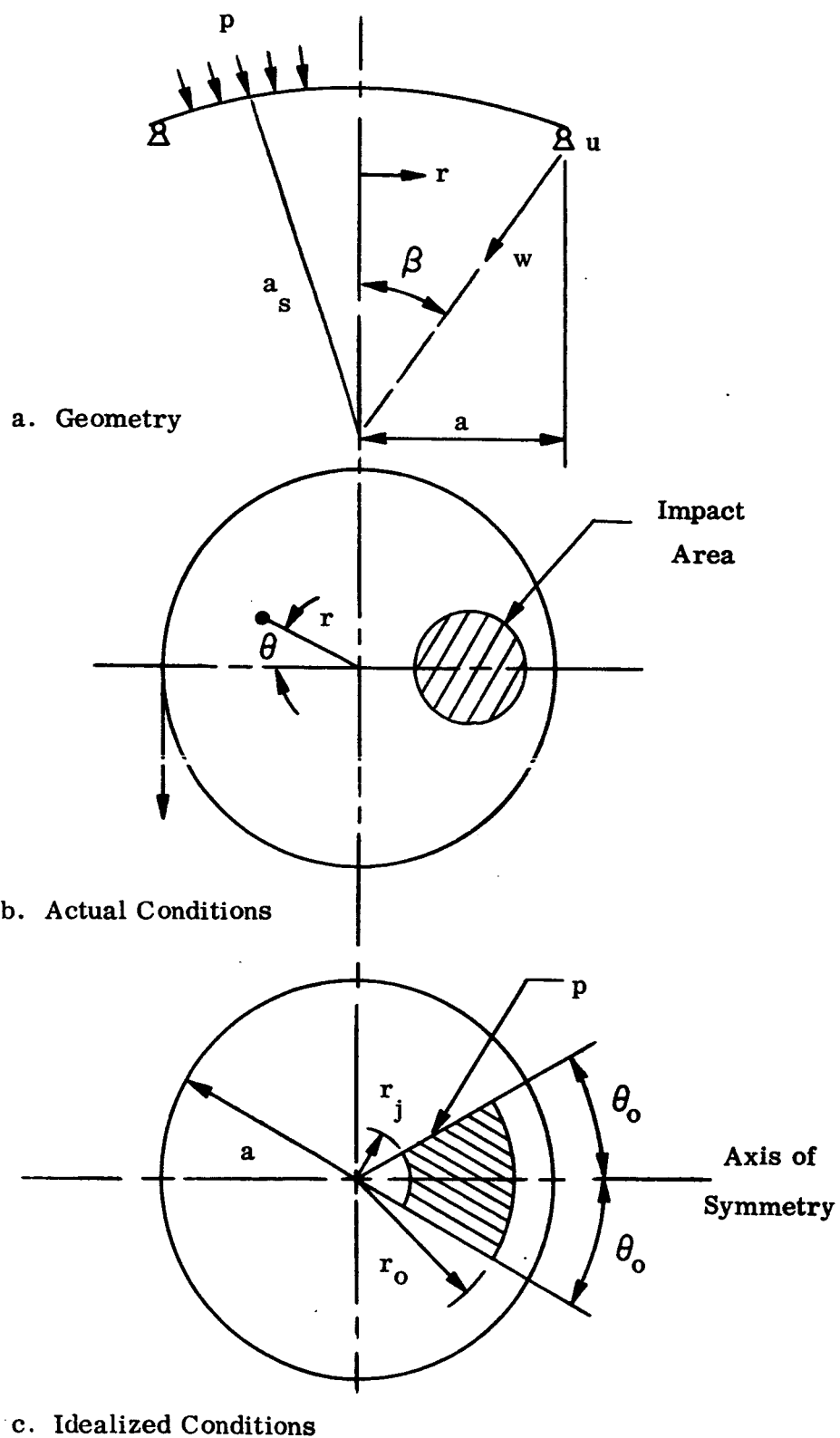


Figure VI-1. Basic Geometry

(a) For clamped edge

no axial displacement

$$w' \cos \beta = w' = 0 \quad (\text{VI-5})$$

no radial slope

$$\frac{\partial w'}{\partial r} \cos \beta = \frac{\partial w'}{\partial r} = 0 \quad (\text{VI-6})$$

no circumferential strain

$$\epsilon_{\theta} = \frac{\partial^2 F'}{\partial r^2} - \frac{\mu}{r} \frac{\partial F'}{\partial r} - \frac{\mu}{r^2} \frac{\partial^2 F'}{\partial \theta^2} = 0 \quad (\text{VI-7})$$

no meridional displacement

$$\begin{aligned} u' \cos \beta - w' \sin \beta &= u' \\ &= \frac{1}{r} \frac{\partial F'}{\partial r} + \frac{1}{r^2} \frac{\partial^2 F'}{\partial \theta^2} - \mu \frac{\partial^2 F'}{\partial r^2} = 0 \end{aligned} \quad (\text{VI-8})$$

(b) For hinged edge

Equations (VI-5), (VI-7), and (VI-8) remain while Equation (VI-6) is replaced by the condition of no radial bending moment. This is in the form of Equation (VI-9).

no radial bending moment

$$M_{rr}' = \frac{\partial^2 w'}{\partial r^2} + \frac{\mu}{r} \frac{\partial w'}{\partial r} + \frac{\mu}{r^2} \frac{\partial^2 w'}{\partial \theta^2} = 0 \quad (\text{VI-9})$$

In the above equations the primes indicate that all the variables are expressed in nondimensional form.

The development of the particular solutions for W and F has presented some problems which were not anticipated and which have necessitated the trial of a number of different approaches before a satisfactory solution could be obtained.

Initially the loaded annular sector of Figure VI-1e was expressed in the form of a double Fourier Series, one of which was then transformed into a power series. Although a solution to the governing differential equations for this loading function could be obtained, comparisons of its degenerate form for the uniform load case with known solutions indicate that the solution was not valid.

Eventually the difficulties were traced to the double Fourier, series which is apparently not valid on a shallow spherical shell. For a shallow shell Bessel Functions must be used and hence, the loading function has to be expressed through a Fourier-Bessel series.

This new solution is considerably more complex than the simple Fourier, series. Full details of the solution with results will be published as a supplement to this report.

B. HEAT SHIELD WITH OVERHANG

The analytical procedure presented above can be extended to obtain solutions to a heat shield with overhang. Such a case is defined in Figure (VI-3). The heat shield shown is supported along a circle of radius a . The portion of the shell inside the supporting circle is designated region "I" while the overhang portion is called region "II".

The governing differential equations for this case remain the same as Equations (VI-1) and (VI-2). The homogeneous solutions to Equations (VI-1) and (VI-2) in Region (I) also remain of the same form as in Equations (VI-3) and (VI-4). In the overhang portion, however, no simplifications could be made except that one constant in may be disregarded due to the fact that the derivatives of $\frac{F}{D_s}$ only are concerned. Therefore, the homogeneous solutions in Region (II) are

$$\begin{aligned} (W_n')_{II} = & \left\{ B_{01}^{(II)} \text{ber } x - B_{02}^{(II)} \text{bei } x + B_{03}^{(II)} \text{ker } x - B_{04}^{(II)} \text{kei } x \right. \\ & + A_{01}^{II} \ln x + A_{03}^{(II)} + \sum_{n=1}^{\infty} [B_1^{II} \text{ber}_n x - B_2^{II} \text{bei}_n x \\ & + B_3^{(II)} \text{ker}_n x - B_4^{(II)} \text{kei}_n x + A_1^{II} x^n + A_3^{(II)} x^{-n}] \cos n\theta \} \end{aligned} \quad (VI-10)$$

$$\begin{aligned} (F_n')_{II} = & \sqrt{\frac{D_m D_s}{D_s}} \left\{ B_{02}^{(II)} \text{ber } x + B_{01}^{(II)} \text{bei } x + B_{04}^{(II)} \text{ker } x \right. \\ & + B_{03}^{(II)} \text{kei } x + A_{02}^{(II)} \ln x + \sum_{n=1}^{\infty} [B_2^{(II)} \text{ber}_n x \\ & + B_1^{(II)} \text{bei } x + B_4^{(II)} \text{ker}_n x + B_3^{(II)} \text{kei}_n x \\ & + A_2^{(II)} x^n + A_4^{(II)} x^{-n}] \cos n\theta \} \end{aligned} \quad (VI-11)$$

From Equations (VI-10) and (VI-11), it is seen that there are ten arbitrary constants for the case $n = 0$ and twelve constants for $n \neq 0$.

To obtain the particular solutions, three loading cases are considered. These are (See Figure VI-2).

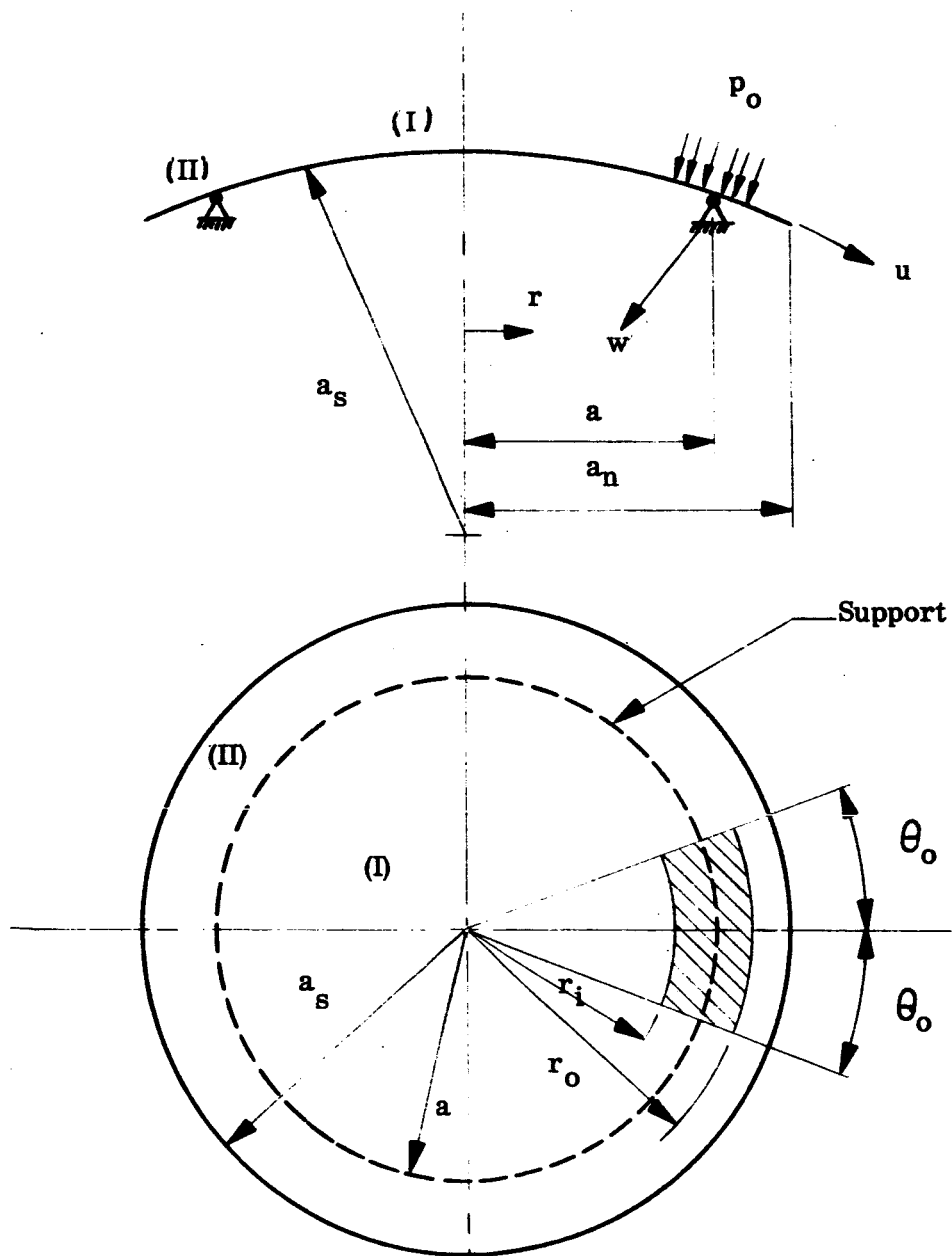


Figure VI-2. Analysis Conditions for Overhang Case

(1) The water impact area inside region (I)

$$r_i < a$$

$$r_o \leq a$$

(2) In both regions (I) and (II)

$$r_i < a$$

$$r_o > a$$

(3) In the overhang portion only

$$r_i \geq 0$$

$$r_i < r_o \leq a_n$$

For the particular solution the same approach is used as for the shell without overhang.

The boundary and continuity conditions needed for solutions are

At $r = a$

no axial displacements in both regions

$$w'_{(I)} = 0 \quad (VI-12)$$

$$w'_{(II)} = 0 \quad (VI-13)$$

no circumferential strain in both regions

$$(\epsilon_\theta)_I = 0 \quad (VI-14)$$

$$(\epsilon_\theta)_{II} = 0 \quad (VI-15)$$

no meridional displacements in both regions

$$u'_{(I)} = 0 \quad (VI-16)$$

$$u'_{(I)} = u'_{(II)} \quad (VI-17)$$

radial slopes are continuous

$$\frac{\partial w'_{(I)}}{\partial r} = \frac{\partial w'_{(II)}}{\partial r} \quad (\text{VI-18})$$

radial moments are continuous

$$(M_{rr}')_I = (M_{rr}')_{II} \quad (\text{VI-19})$$

At $r = a_h$

no radial bending moment

$$(M_{rr}')_{II} = 0 \quad (\text{VI-20})$$

boundary shear must vanish

$$\left(V_r' - \frac{l}{r} \frac{2 M_{r\theta}'}{2\theta} \right) = 0 \quad (\text{VI-21})$$

no radial membrane force

$$(N_{rr}')_{II} = 0 \quad (\text{VI-22})$$

no shear membrane force

$$(N_{r\theta}') = 0 \quad (\text{VI-23})$$

These above conditions are satisfied for the determination of the twelve arbitrary constants for the case $n \neq 0$. For $n = 0$ there are ten arbitrary constants, the conditions of Equations (VI-17) and (VI-23) are disregarded.

The solution procedure from this point on is essentially the same as that described for the case without overhang.

C. SOLUTION FOR UNIFORM THERMAL FORCE AND UNIFORM THERMAL MOMENT

Under the conditions of uniform thermal loading the governing differential equations (Equations VI-1) and (VI-2) reduce to the homogeneous form

$$\nabla^4 F' + \frac{l}{a_s} \frac{D_m}{D_s} \nabla^2 w' = 0 \quad (\text{VI-24})$$

$$\nabla^4 w' - \frac{1}{a_s l} \nabla^2 F' = 0 \quad (\text{VI-25})$$

Since the current problem is axisymmetric the homogeneous solutions can be written as

$$W' = c_1 \operatorname{bei} x - c_2 \operatorname{bei} x + c_3 \quad (\text{VI-26})$$

$$F' = -\sqrt{\frac{a^2 D_m}{D_s}} [c_1 \operatorname{bei} x + c_2 \operatorname{bei} x] \quad (\text{VI-27})$$

It is to be noted that, as yet, the effects of the thermal loading have not been introduced. In the case of uniform thermal loading, stresses are only introduced by restraining the thermal deformation and hence the magnitude of the thermal loading appear only when the boundary conditions are considered. The shell is fully fixed at the bolt circle. The boundary conditions are then

$$W' = 0, \quad \epsilon_\theta = \beta, \quad \frac{\partial W'}{\partial r} = 0 \quad \text{at} \quad \frac{r}{a} = 1$$

where the circumferential strain ϵ_θ is given by

$$\begin{aligned} \epsilon_\theta &= \frac{1}{D_m} \left[\frac{\partial^2 F}{\partial r^2} - \frac{\mu}{r} \frac{\partial F}{\partial r} + N_\alpha \right] \\ &= \frac{D_s}{a^2 D_m} \left[\frac{\partial^2 F'}{\partial x^2} - \frac{\mu}{x} \frac{\partial F'}{\partial r} \right] + \frac{N_\alpha}{D_m} \end{aligned} \quad (\text{VI-28})$$

and N_α is the thermal force.

It is to be noted, as was to have been anticipated, that the thermal moment term does not appear explicitly in this case.

The three relevant constants c_1, c_2, c_3 are then obtained by the solution of the simultaneous equations as

$$\begin{aligned} c_1 &= \frac{\frac{a_s}{a} \cdot \frac{N_\alpha}{D_m} \cdot \operatorname{bei}' \frac{a}{l}}{\operatorname{ber} \frac{a}{l} \cdot \operatorname{bei}' \frac{a}{l} - \operatorname{bei} \frac{a}{l} \operatorname{ber}' \frac{a}{l} - \frac{1+\mu}{a/l} [(\operatorname{ber}' \frac{a}{l})^2 + (\operatorname{bei}' \frac{a}{l})^2]} \\ c_2 &= \frac{\operatorname{ber}' \frac{a}{l}}{\operatorname{bei}' \frac{a}{l}} \cdot c_1 \end{aligned} \quad (\text{VI-29})$$

$$c_3 = -\operatorname{ber} \frac{a}{l} \cdot c_1 + \operatorname{bei} \frac{a}{l} \cdot c_2$$

For the case under consideration the following numerical values were used.

$$a_s = 175.6, \quad D_s = 1.4993 \times 10^6, \quad D_m = 0.9422 \times 10^6, \quad a = 57.2$$

$$M_\alpha = 1504 \text{ lb.}, \quad N_\alpha = 3426 \text{ lb./in.}$$

$$\text{Thus } l = 4 \sqrt{\frac{a^2 D_s}{D_m}} = 14.883, \quad \mu = 0.3$$

$$c_1 = 1.4440 \times 10^{-3}, c_2 = 2.9355 \times 10^{-2}, c_3 = 7.1672 \times 10^{-2}$$

$$\text{Central Deflection} = \ell (c_1 + c_3) = 1.0882 \text{ in.}$$

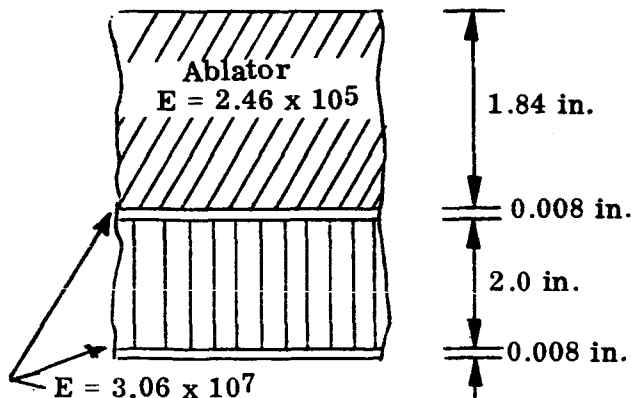
A complete profile of the displacements along the axis of symmetry is given in Figure

At center of heat shield

$$M_r = \frac{\sqrt{D_1 \cdot D_3}}{2} \cdot c_1 \left(\frac{1}{x} \text{bei } x \right)_{x=0} = 57.66 \text{ lb./in.}$$

$$M_r = - \frac{D_3}{\ell} c_2 \cdot \text{bei } 0 + M_a = -1478 + 1504 = 26 \text{ lb./in./in.}$$

For the chosen section, the details are shown in the sketch.



The position of the neutral axis is 1.953 from the lower surface.

Using the calculated membrane force $M_r = 57.66 \text{ lb./in.}$, the stresses in the ablator and steel faces are

$$\sigma_{M_{ab}} = 13.70 \text{ psi (Compressive)}$$

$$\sigma_{M_c} = 1704.1 \text{ psi (Compressive)}$$

The bending moment $M_r = 26 \text{ lb./in./in.}$ produces the following stresses.

$$\text{In lower steel face } \sigma_s = 1025.7 \text{ psi (Tensile)}$$

$$\text{In upper edge of ablator } \sigma_s = 82.0 \text{ psi (Compressive)}$$

VII. CONCLUDING REMARKS

The discrete element approach to structural analysis has been shown to be an appropriate means for the analysis of the Apollo aft heat shield where the seemingly regular geometry would appear to make attractive classical solution approaches. In the actual circumstances, the analysis must account for irregular loadings, temperatures, and a wide variety of possible support conditions. More significant perhaps is the irregularity of the cross-sectional dimensions as produced by scalloping of the sandwich faces and the variable thickness ablator, and by the portion of the heat shield which overhangs the ablator. All of these effects are treated directly by means of discrete elements of triangular and quadrilateral form.

Further developmental work in connection with discrete element properties is nevertheless indicated. Two promising directions have been found. In one, sandwich-type elements can be employed. Presently, this approach required implementation with respect to the refinement of the idealization, wherein a very much larger number of degrees of freedom must be utilized. Also, the available element relationships which are derived on the basis of equal face thicknesses, must be extended to account for a load carrying ablator attached at one face.

It should be additionally noted that if design requirements involve the determination of peaked stresses, an approach based on finite elements (or finite differences) will be inadequate, or in the least inefficient, if the problem is approached through use of a single idealization of the complete heat shield. Logically, a gridwork of reasonable refinement should be employed to obtain the overall stress and displacement pattern. Then, a high degree of refinement should be employed in the idealization of an isolated portion of the structure, where the determination of peaked stresses is desired. Procedures for this type of approach are easily defined, but have not been properly tested in practice.

With respect to buckling, a finite deformation-finite displacement formulation would be a logical step toward improved prediction of behavior of the heat shield. The present instability analysis capability exhibits complete membrane-bending coupling between discrete elements of an assembly. With reference to a single discrete element, however, only the effect of membrane action on bending stiffness is considered. This latter procedure is a conceptual extension of the linear formulation which allows the prediction of critical loads for structures which experience small deformations and small displacements prior to buckling.

Although the finite displacement formulation involves major modification of the instability analysis capability, it could be expected to significantly improve the prediction of behavior. As stated by B. Budiansky and J. Sanders as a result of their examination of certain phases of this Apollo heat shield structural analyses (Reference 18) "should a static nonlinear analysis be done? On the basis of some estimates we made we concluded that one should be done." In this same report, emphasis is given

to the view that since a nonlinear analysis is feasible, it is important to perform it and dispense with the empirically-modified linear result, since the empirical factor is of ill-defined reliability.

As a final comment, the determination of thermal stresses in the heat shield is a subject requiring more extensive and detailed attention than it could be given in this effort. Classical solutions for significant thermal stress situations in shallow shells are virtually nonexistent. This being the case, proper verification of the adequacy and special safeguards to be taken in a discrete element approach is difficult to achieve.

In a specific, related, problem the extremely high predicted thermal stresses for the heat shield are indicative of an unrealistic definition of the support conditions. The elastic nature of the support in the radial direction in the plane of the bolt circle should be taken into account. Also, no recognition has been given to the existence of initial assembly stresses. It is known that the ablator is applied to the heat shield at a temperature other than ambient room temperature. Thus, at room temperature, thermal stresses are produced in consequence of the differences in expansion coefficient of the ablator and the sandwich.

REFERENCES

1. Anon., "Analytical Solution for the Determination of Stresses and Displacements in Heat Shield Structures Under Nonuniform Loads," Bell Aerosystems Co. Report No. D7218-933005, to be released.
2. Anon., "Structural Analyses of Apollo Aft Heat Shield," First Quarterly Progress Report, Bell Aerosystems Co. Report No. D7218-933002, June 1965.
3. Gallagher, R.H. and Huff, R.D., "Derivation of the Force-Displacement Properties of Triangular and Quadrilateral Orthotropic Plates in Plane Stress and Bending," Report No. D2114-950005, Jan. 1964.
4. Pestel, E. and Leckie, F.W., "Matrix Methods in Elastomechanics," McGraw-Hill Book Co.
5. Batt, J.R., "Dynamic Response Analysis of Apollo Heat Shield," Bell Aerosystems Company, Report No. D7218-933006, March 1966.
6. Gallagher, R.H. and Padlog J., "Discrete Element Approach to Structural Instability Analysis," AIAA Journal, June 1963.
7. Wempner, G.A., and Kesti, N.E., "On the Buckling of Circular Arches and Rings," Proceedings of the 4th U.S. National Congress of Applied Mechanics, 1962.
8. Kaplan, A. and Fung, Y.C., "A Nonlinear Theory of Bending and Buckling of Thin Elastic Shallow Spherical Shells," NACA TN 3212, 1954.
9. Gerard, G. and Becker, H., "Handbook of Structural Stability, Part III--Buckling of Curved Plates and Shells," NACA TN 3783, 1957.
10. Turner, M.J., Clough, R.C., Martin, H.C. and Topp, L.J., "Stiffness and Deflection Analysis of Complex Structures," Journal of Aeronautical Sciences, Sept. 1956.
11. Melosh, R.J., "Basis for Derivation of Matrices for the Direct Stiffness Method," AIAA Journal, July 1963.
12. Bogner, F.K., Fox, R.L., and Schmit, L.A., "The Generation of Interelement-Compatible Stiffness and Mass Matrices by the Use of Interpolation Formulas," Conference on Matrix Methods in Structural Mechanics, Wright Field, Dayton, Ohio, Oct. 1965.
13. Fraeijs de Veubeke, B., "Bending and Stretching of Plates, Special Models for Upper and Lower Bounds," Conference on Matrix Methods in Structural Mechanics, Wright Field, Dayton, Ohio, Oct. 1965.

14. Clough, R.W. and Tocher, J.L., "Finite Element Stiffness Matrices for the Analysis of Plate Bending," Conference on Matrix Methods in Structural Mechanics, Wright Field, Dayton, Ohio, Oct. 1965.
15. Gellatly, R.A. and Gallagher, R.H., "Determining Maximum Stresses and Displacements in Sandwich Panels, Part I," Machine Design, Dec. 17, 1964.
16. Gallagher, R.H., "A Correlation Study of Methods of Matrix Structural Analysis," AGARDograph 69, Pergamon Press, Oxford 1964.
17. Scanlan, R. and Rosenbaum, S., "Aircraft Vibration and Flutter," MacMillan Co., 1951.
18. Sanders, J.L., "Report on Apollo Shell Structure," Communication to NASA Manned Spacecraft Center, July, 1965.
19. Reissner, E., "Stresses and Small Displacements of Shallow Spherical Shells," (I) Journal of Math. and Phys. 25 (1) 1946.
20. Reissner, E., "Stresses and Small Displacements of Shallow Spherical Shells," (II), Journal of Math. and Phys. 25 (4), 1947.
21. Reissner, E., "On the Determination of Stresses and Displacements for Unsymmetrical Deformations of Shallow Spherical Shells," Journal of Math. and Phys. 38 (1), 1959.

APPENDIX A
MATRIX DISCRETE ELEMENT ANALYSIS PROCEDURE -
LINEAR STATIC ANALYSIS

1. GENERAL CONCEPTS

The purpose of this appendix is to develop, from basic principles, the concepts of elastic linear, discrete element structural analysis (10)(16), as applied to static loading conditions.

In this method of analysis, structures are idealized as systems of connected discrete elements. The points of connection are called "reference" or "node" points. Each class of discrete element (bar, triangular plate, beam segment, etc.) possesses a finite number of connection points, the specific number in a given case being dictated by the number of parameters needed to define the variation of the edge stress systems acting upon the element. A hypothetical element, a rectangular plate segment of a plate component, having four reference points, is shown below. (Figure A-1)

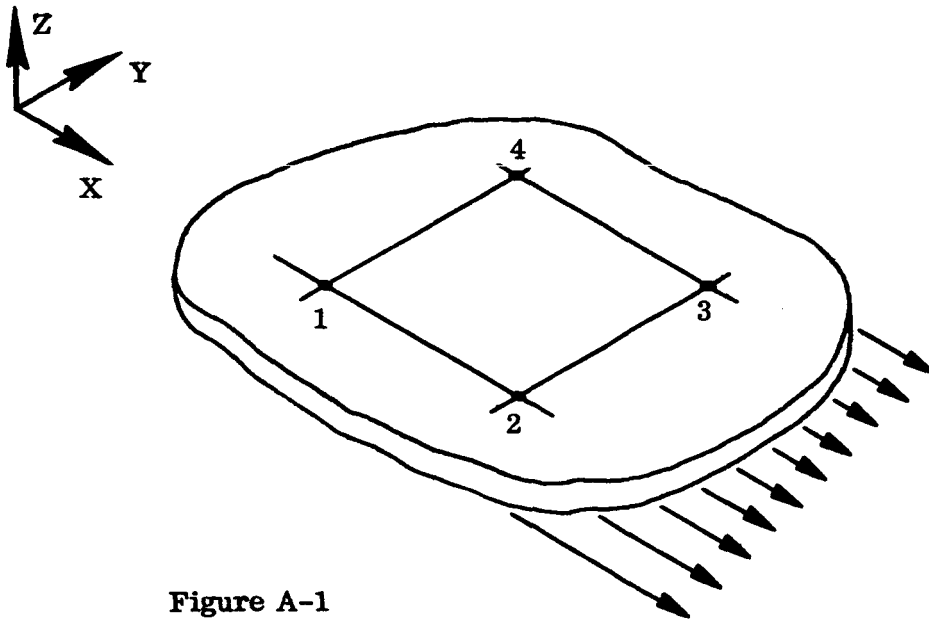


Figure A-1

For any such element, it is first necessary to derive relationships between the displacements $\{\Delta_e\}$ of the boundary points and the forces $\{F\}$ acting at these points. The node point forces are statically equivalent to the stresses that actually exist on the edge areas subtended by the point. On the basis of assumptions as to element deformational behavior, it is possible to establish the desired relationships in matrix form, as

$$\{F\} = [K] \{\Delta_e\} + \{F^*\} \quad (A-1)$$

where

$[K]$ is the "element stiffness matrix",

$\{\Delta_e\}$ are the displacements of the points on the element (node points) which join with the adjacent elements or with the supports,

$\{F\}$ are the stress resultants, or equivalent forces, at the element node points,

$\{F^*\}$ are the "thermal forces", representing the effect of a temperature change with the element.

Methods for the formulation of the terms of this equation are detailed in References 11 and 16.

Once the element relationships have been evaluated, the elements are assembled to form the complete analytical model of the structure by joining all elements at their respective juncture points and applying, in the process, the requirements of juncture point equilibrium and compatibility. The theoretical basis for this operation is as follows.

The components of internal loads $\{F\}$ and net external loads $\{P\}$ at each point are related by equilibrium requirements; i.e., $\sum F_x = P_x$, etc. The respective coordinate displacements of the corner points of all elements meeting at a point are equal, a requirement that satisfies compatibility. The result is that the stiffness matrix $[K]$ for the complete structure can be assembled by merely adding element stiffness coefficients having identical subscripts. This yields a set of algebraic equations:

$$\{P\} = [K] \{\Delta\} + \{P^*\} \quad (A-2)$$

The matrix $[K]$ will henceforth be referred to as the "master" stiffness matrix. Displacement boundary conditions can be readily imposed by assigning the pertinent Δ 's their known values (usually zero). The matrix $[K]$ will be altered in the process, and, taking note of this by utilizing the subscript R, the solution to the altered Equation (A-2) becomes (if matrix inversion is utilized),

$$\{\Delta_R\} = [K_R]^{-1} \{\{P_R\} - \{P_R^*\}\} = [\delta] \{\{P_R\} - \{P_R^*\}\} \quad (A-3)$$

where $\{\delta\}$ represents the set of displacement influence coefficients. This is the equilibrium static solution. The displacement influence coefficients are directly useful for subsequent dynamic analyses.

To obtain the stresses from the displacement solution, the displacement vectors for the respective elements $\{\Delta_e\}$ are first selected from the total column of displacements. Then, each such vector is multiplied by the associated stiffness matrix (Equation A-1) to determine the node point forces $\{F_e\}$. In an additional step, the node point forces can be transformed into the corresponding stresses. It has been found more efficient, however, to form at the outset direct relationships between the element stresses and the node point displacements, as follows:

$$\{\sigma_e\} = [S] \{\Delta_e\} + \{\sigma^*\} \quad (A-4)$$

where $\{\sigma_e\}$ are the stress values which characterize the distribution of stress within an element, $\{\sigma^*\}$ are the stresses corresponding to the thermal forces, and $[S]$ is known as the "element stress matrix". The procedure followed, therefore, is to establish, first, the stress matrices at the start of a computation. When the displacement vectors for the respective elements $\{\Delta_e\}$ are evaluated, they are premultiplied by the corresponding element stress matrices to obtain the solutions for stress.

2. BELL GENERAL PURPOSE STRUCTURAL ANALYSIS COMPUTER PROGRAM

The Bell "General Purpose" Matrix Structural Analysis Program, coded for operation on an IBM 7090 computer, is designed to accept the basic information describing a problem, establish its formulation, and perform all computations required for the development of the desired stress and/or displacement results. The operational procedures for the program conform to the theory outlined earlier.

The basic problem information (input to the program) consists of:

- (1) Dimensions of the structure
- (2) Load and temperature conditions of interest
- (3) Material mechanical properties
- (4) Operational controls; i.e., specification of the desired printout items, etc.
- (5) Designation of the discrete elements

From an operational standpoint, the Bell General Purpose Structural Analysis Program consists of three major computational routines:

- (1) A library of element stiffness relationships
- (2) A routine wherein the master stiffness matrix is calculated, boundary conditions are applied, and the matrix inverted.
- (3) A routine which selects information from (1) and the resulting inverse from (2), and calculates stress, displacement, etc.

Routine (1) is the key to the versatility of the program, since the capability to analyze a given type of configuration is dependent upon the availability, in the element library, of relationships for elements of the proper geometric form and behavior. A listing of the more commonly used elements in the program is given as Table A-1. These elements are pictured in Figure A-2. Elements employed in the subject analyses are discussed in the next section.

Three of the detailed operational capabilities of the program are of specific interest:

- (1) Although element properties are stored in the program in algebraic form and are automatically evaluated on the basis of input data, it is also permissible to input directly an evaluated element stiffness matrix. Thus, if the stiffness coefficients for a major component have been evaluated elsewhere, this component can be represented in the analysis as a single discrete element.
- (2) Special coordinate axes can be established at any or all points. The force and displacement vectors at each reference point are initially referenced to a single set of axes for the complete structure (system axes). The need for utilization of this capability arises, for example, in the following cases:
 - (a) A structure is constrained to displace in directions other than the system axes (Figure A-3a). Thus, the x' - y' axes must be defined at all the support points and used to specify the y' -direction constraints.
 - (b) On a shell in flexure, when the individual elements are each flat plates, the two-dimensional moment vectors on the respective elements meeting at a point produce on extremely small net vector in the direction normal to the tangent plane at the point (Figure A-3b). If the coordinate axes are made to correspond to the tangent plane, this degree-of-freedom normal to the tangent plane can be suppressed with a consequent improvement in the accuracy of the solution.
- (3) The inverted stiffness matrix (i.e., the flexibility matrix) can be stored on tape and any or all elements of this matrix can be recalled at a later time for the purpose of subsequent dynamic analyses.

APPENDIX B

DYNAMIC RESPONSE ANALYSIS PROCEDURE

1. GENERAL

The equations of motion for a system of grid points, describing an elastic structure, can be written in the following matrix form:

$$[M] \{\ddot{\Delta}\} + [D] \{\dot{\Delta}\} + [K] \{\Delta\} = \{\bar{F}_{(t)}\} \quad (B-1)$$

where

$[M]$ is the mass matrix

$[D]$ is the damping matrix

$[K]$ is the pertinent stiffness matrix

$\{\Delta\}, \{\dot{\Delta}\}, \{\ddot{\Delta}\}$ are displacement, velocity and acceleration vectors, respectively

$\{\bar{F}_{(t)}\}$ is a forcing function matrix

The displacement vector $\{\Delta\}$ can represent motion along and about coordinate axes. The mass, damping and stiffness matrices will then consist of terms consistent with these motions.

Equation (B-1) is applicable to any elastic structure. The component matrices, however, depend on the coordinate system employed. The displacement degrees of freedom $\{\Delta\}$ can be identical to those of the structural idealization grid system or can be derived from the natural modes of vibration of the structure. The coordinates resulting from the latter approach are called generalized coordinates and are discussed in detail in this Appendix. The appendix is concluded with a description of the integration of Equation (B-1).

The use of generalized coordinates (or the so-called normal mode approach) results in equations of motion with the following characteristics:

- (a) The first eight to ten modes of vibration will generally be sufficient for dynamic response analysis purposes, as compared to perhaps 300-500 degrees of freedom required for the accurate determination of the flexibility characteristics when the structural grid system is used. Therefore, lower order matrices in Equation (B-1) will result.
- (b) The mass matrix $[M]$ will be a diagonal matrix as there will be no mass coupling between the natural modes.
- (c) The stiffness matrix $[K]$ will be a diagonal matrix since there will be no elastic coupling between natural modes.

The adoption of the model approach in the dynamic response analysis portion of the investigation permits the initial determination of stiffness characteristics on the refined basis described previously, while enabling the performance of computationally efficient analyses.

2. DYNAMIC RESPONSE EQUATION USING GENERALIZED COORDINATES

Consider the structural grid system sketched below where the i th grid point has an assigned mass, m_i , and is undergoing a displacement w_i . In this instance, the displacement vector $\{\Delta\}$ consists of the single translational degree of freedom w at each grid point. The following results can readily be extended to include other degrees of freedom.

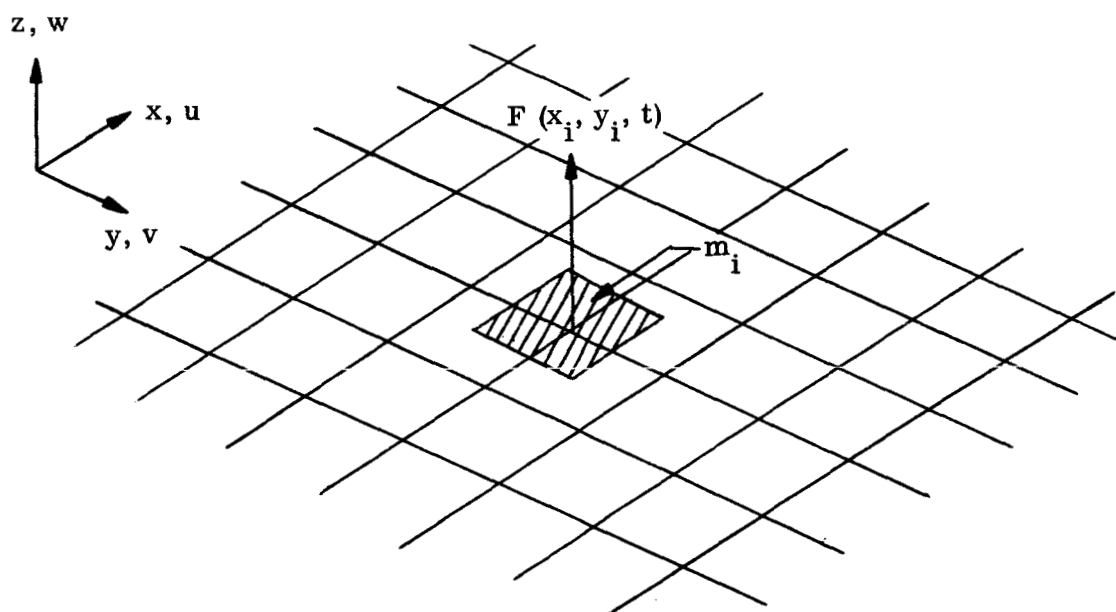


Figure B-1. Typical Grid System

It is assumed that the displacement at point i , due to a dynamic load $F(x_i, y_i, t)$ can be represented by the series

$$w(x_i, y_i, t) = \sum_{j=1}^{\infty} w_j(x_i, y_i) \xi_j(t) \quad (\text{B-2})$$

where $w_j(x_i, y_i)$ is the j^{th} normalized vibration mode shape evaluated at the i^{th} point and $\xi_j(t)$ is the generalized coordinate in the j^{th} vibration mode.

The kinetic energy at the i^{th} point may be written as

$$T_i = \frac{1}{2} m_i [\dot{w}_j(x_i, y_i, t)]^2 \quad (\text{B-3})$$

or

$$T_i = \frac{1}{2} m_i \left[\sum_{j=1}^{\infty} \bar{w}_j \dot{\xi}_j \right]^2 \quad (\text{B-4})$$

Expansion of Equation (B-4) yields

$$T_i = \frac{1}{2} m_i \bar{w}_1^2 \dot{\xi}_1^2 + \frac{1}{2} m_i \bar{w}_2^2 \dot{\xi}_2^2 + \dots \\ + \frac{1}{2} m_i \bar{w}_1 \bar{w}_2 \dot{\xi}_1 \dot{\xi}_2 + \frac{1}{2} m_i \bar{w}_1 \bar{w}_3 \dot{\xi}_1 \dot{\xi}_3 + \dots \quad (\text{B-5})$$

Since natural modes are orthogonal the sum of terms of the form

$$\frac{1}{2} m_i \bar{w}_j \bar{w}_k \dot{\xi}_j \dot{\xi}_k = 0, \quad j \neq k; \quad \frac{1}{2} m_i \bar{w}_j \bar{w}_k \neq 0, \quad j = k$$

Thus, Equation (B-5) becomes

$$T_i = \frac{1}{2} m_i [\bar{w}_1^2 \dot{\xi}_1^2 + \bar{w}_2^2 \dot{\xi}_2^2 + \bar{w}_3^2 \dot{\xi}_3^2 + \dots + \bar{w}_N^2 \dot{\xi}_N^2] \quad (\text{B-6})$$

for $j = k$.

The kinetic energy term in Lagrange's equation of motion is given by $\frac{d}{dt} \left(\frac{\partial T}{\partial \dot{\xi}_j} \right)$ where T is the total kinetic energy of the system, i.e.

$$T = \sum_{i=1}^N T_i = \sum_{i=1}^N \frac{1}{2} m_i [\bar{w}_1^2 \dot{\xi}_1^2 + \bar{w}_2^2 \dot{\xi}_2^2 + \dots + \bar{w}_j^2 \dot{\xi}_j^2 + \dots] \quad (\text{B-7})$$

$j = 1, 2, 3, \dots, \infty$

Thus, we can write

$$\frac{d}{dt} \left(\frac{\partial T}{\partial \dot{\xi}_1} \right) = \sum_{i=1}^N m_i \bar{w}_1^2 \ddot{\xi}_1 \\ \frac{d}{dt} \left(\frac{\partial T}{\partial \dot{\xi}_2} \right) = \sum_{i=1}^N m_i \bar{w}_2^2 \ddot{\xi}_2 \quad (\text{B-8})$$

etc.

or more generally

$$\boxed{\frac{d}{dt} \left(\frac{\partial T}{\partial \dot{\xi}_j} \right) = M_j \ddot{\xi}_j} \quad (\text{B-9})$$

where $M_j = \sum_{i=1}^N m_i [\bar{w}_j(x_i, y_i)]^2$ is the generalized mass.

The strain energy of the system is derivable by analogy to a simple spring-mass system vibrating in a natural mode. When the entire grid system is vibrating in a natural mode it can be said to have a mass M_j (the generalized mass), displacement ξ_j (the generalized displacement), stiffness K_j (the generalized stiffness) and natural frequency ω_j . The net potential energy stored by this system is given by (see Figure B-2).

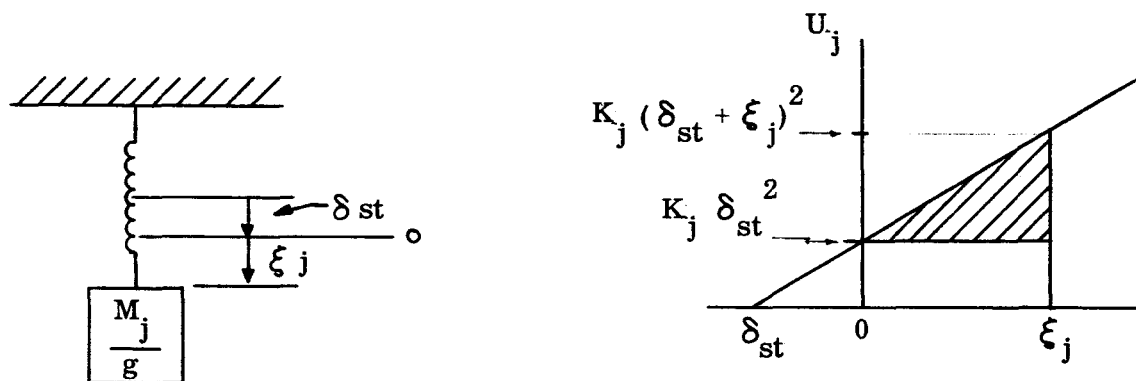


Figure B-2. Displacement

$$U_j = \left[\frac{1}{2} K_j (\delta_{st} + \xi_j)^2 - \frac{1}{2} K_j \delta_{st}^2 \right] - \left(\frac{M_j}{g} \right) \xi_j \quad (B-10)$$

Since $K_j \delta_{st} = \frac{M_j}{g}$ Equation (B-10) can be rewritten as

$$U_j = \frac{1}{2} K_j \xi_j^2 \quad (B-11)$$

$$\text{Now } K_j = \omega_j^2 M_j \quad (B-12)$$

$$\text{hence } U_j = \frac{1}{2} \omega_j^2 M_j \xi_j^2. \quad (B-13)$$

The total potential energy of the grid system is given by the following expression:

$$U = \sum_{j=1}^{\infty} U_j = \frac{1}{2} \omega_1^2 M_1 \xi_1^2 + \frac{1}{2} \omega_2^2 M_2 \xi_2^2 + \dots + \frac{1}{2} \omega_j^2 M_j \xi_j^2 + \dots \quad (B-14)$$

Equation (B-14) is a quadratic function of the generalized coordinates ξ_j and agrees with the approach discussed in Reference

The potential energy term in Lagrange's equation of motion is given by $\frac{\partial U}{\partial \xi_i}$ where U is the total potential energy of the system. Thus

$$\begin{aligned}\frac{\partial U}{\partial \xi_1} &= \omega_1^2 M_1 \xi_1 \\ \frac{\partial U}{\partial \xi_2} &= \omega_2^2 M_2 \xi_2 \\ &\text{etc.}\end{aligned}\tag{B-15}$$

or more generally

$$\boxed{\frac{\partial U}{\partial \xi_j} = K_j \xi_j}\tag{B-16}$$

where $K_j = \omega_j^2 M_j$ is the generalized stiffness and ω_j is the frequency of the vibration mode.

In accordance with Reference 17 an energy dissipation function associated with structural damping can be setup as follows

$$\bar{D}_j = \frac{1}{2} \frac{M_j \omega_j^2 g_j}{\omega} \dot{\xi}_j^2\tag{B-16a}$$

\bar{D}_j is the damping term associated with the j^{th} mode, g_j is the damping coefficient in the j^{th} mode and ω is the response frequency. The damping term in Lagrange's equations of motion is given by $\frac{\partial D}{\partial \dot{\xi}_j}$ where D is the total energy dissipated. Thus, we may write

$$\boxed{\frac{\partial D}{\partial \dot{\xi}_j} = D_j \dot{\xi}_j}\tag{B-17}$$

where $D_j = \frac{M_j \omega_j^2 g_j}{\omega}$ the generalized damping.

The total virtual work done on the system due to an incremental displacement (or virtual displacement) in each degree of freedom is

$$\delta W_e = \sum_{i=1}^N F(x_i, y_i, t) \delta w(x_i, y_i, t)\tag{B-18}$$

Substitution of Equation (B-2) into Equation (B-18) yields

$$\delta W_e = \sum_{j=1}^{\infty} \left(\sum_{i=1}^N \bar{w}_j(x_i, y_i) F(x_i, y_i, t) \right) \delta \xi_j\tag{B-19}$$

The generalized force term in Lagrange's equations of motion is given by

$$Q_j = \frac{\partial (\delta W_e)}{\partial (\delta \xi_j)} \quad (B-20)$$

thus

$$Q_j = \sum_{i=1}^N \bar{w}_j(x_i, y_i) F(x_i, y_i, t) \quad (B-21)$$

Equations (B-9), (B-16), (B-17), and (B-21) are summed to form the differential equations of motion of the system.

$$M_j \ddot{\xi}_j + D_j \dot{\xi}_j + K_j \xi_j = Q_j \quad (B-22)$$

or in matrix form

$$[M]\{\ddot{\xi}\} + [D]\{\dot{\xi}\} + [K]\{\xi\} = \{Q\}. \quad (B-23)$$

Equation (B-23) is identical in form to Equation (B-1) with the exception that the matrix coefficients are diagonal; that is, the equations of motion are uncoupled.

For a finite number of vibration modes, say $j = 3$, a finite number of grid points, say $N = 6$, and forcing functions acting only at grid points 1 and 2, three equations in three unknowns are obtained as follows:

$$\begin{bmatrix} M_1 & 0 & 0 \\ 0 & M_2 & 0 \\ 0 & 0 & M_3 \end{bmatrix} \begin{Bmatrix} \ddot{\xi}_1 \\ \ddot{\xi}_2 \\ \ddot{\xi}_3 \end{Bmatrix} + \begin{bmatrix} \frac{g_1 \omega_1^2 M_1}{\omega} & 0 & 0 \\ 0 & \frac{g_2 \omega_2^2 M_2}{\omega} & 0 \\ 0 & 0 & \frac{g_3 \omega_3^2 M_3}{\omega} \end{bmatrix} \begin{Bmatrix} \dot{\xi}_1 \\ \dot{\xi}_2 \\ \dot{\xi}_3 \end{Bmatrix}$$

$$+ \begin{bmatrix} \omega_1^2 M_1 & 0 & 0 \\ 0 & \omega_2^2 M_2 & 0 \\ 0 & 0 & \omega_3^2 M_3 \end{bmatrix} \begin{Bmatrix} \xi_1 \\ \xi_2 \\ \xi_3 \end{Bmatrix}$$

$$= \begin{bmatrix} \bar{w}_1(x_1, y_1) & \bar{w}_1(x_2, y_2) \\ \bar{w}_2(x_1, y_1) & \bar{w}_2(x_2, y_2) \\ \bar{w}_3(x_1, y_1) & \bar{w}_3(x_2, y_2) \end{bmatrix} \begin{Bmatrix} F(x_1, y_1, t) \\ F(x_2, y_2, t) \end{Bmatrix}$$

Note that the number of modes determines the matrix order of the left-hand side of the equation while the number of modes and number of forcing functions determine the matrix order on the right-hand side.

It is a simple matter to determine the true displacement at a grid point by use of Equation (B-2) once the generalized displacements as a function of time are known. Suppose that in the present illustrative example displacements at grid points 1, 3, 5, and 6 are desired. Use of Equation (B-2) yields the matrix expression.

$$\begin{Bmatrix} w(x_1, y_1, t) \\ w(x_3, y_3, t) \\ w(x_5, y_5, t) \\ w(x_6, y_6, t) \end{Bmatrix} = \begin{bmatrix} \bar{w}_1(x_1, y_1) & \bar{w}_2(x_1, y_1) & \bar{w}_3(x_1, y_1) \\ \bar{w}_1(x_3, y_3) & \bar{w}_2(x_3, y_3) & \bar{w}_3(x_3, y_3) \\ \bar{w}_1(x_5, y_5) & \bar{w}_2(x_5, y_5) & \bar{w}_3(x_5, y_5) \\ \bar{w}_1(x_6, y_6) & \bar{w}_2(x_6, y_6) & \bar{w}_3(x_6, y_6) \end{bmatrix} \begin{Bmatrix} \xi_1(t) \\ \xi_2(t) \\ \xi_3(t) \end{Bmatrix} \quad (B-25)$$

This same matrix expression is used to determine grid point velocities and accelerations by replacing the $\{\xi(t)\}$ matrix by $\{\dot{\xi}(t)\}$ and $\{\ddot{\xi}(t)\}$ matrices.

3. INTEGRATION OF THE EQUATIONS OF MOTION

The evaluation of dynamic response, in the form of time histories for Δ , $\dot{\Delta}$ and $\ddot{\Delta}$ involves the determination of instantaneous acceleration over a small interval of time, followed by the performance of single and double integrations to obtain velocity and displacement changes over the same interval. The velocity and displacement changes are then added to the initial starting values, and the process is repeated for the next interval. This process forms the basis of the Bell-Matrix-Iteration-Time-History program which is described below. Note that the method applies equally well to Equation (B-1) or (B-23).

The method proceeds as follows. First, Equation (B-1) is written in the form of a solution for $\{\ddot{\Delta}\}$

$$\{\ddot{\Delta}\} = [M]^{-1} \{F\} - [D]\{\dot{\Delta}\} - [K_R]\{\Delta\} \quad (B-26)$$

The matrices $\{F\}$, $[M]$, $[D]$ and $[K]$ are known. For any starting time t_0 , the values of $\{\dot{\Delta}\}$ and $\{\Delta\}$ are prescribed. The latter are zero if the system is initially at rest.

The foregoing values of acceleration computed for t_0 are assumed to exist over a small time interval, $t_1 - t_0$, and values of $\{\dot{\Delta}\}_1$ are computed from

$$\{\dot{\Delta}\}_1 = \{\dot{\Delta}_0\} + \frac{1}{2} (t_1 - t_0) \{ \ddot{\Delta}_1 + \ddot{\Delta}_0 \} \quad (B-27)$$

which will be recognized as a simple time integration. Then, the displacement at the end of t_1 is then computed from a second integration

$$\{\Delta\}_1 = \{\Delta\}_0 + \frac{1}{2} (t_1 - t_0) \{\dot{\Delta}\}_1 + \{\dot{\Delta}\}_0 \quad (B-28)$$

It will be noted that average velocities and displacements are obtained simply as one-half the sum of the initial and final values. While much more elaborate formulations could be used, they are considered less desirable than using closely spaced time intervals.

It will be noted that some error will exist in the above computations when the system is elastically deformed since the deflection pattern at t_1 will not be the same as at t_0 , causing accelerations at t_0 to be different than accelerations at t_1 via Equation (B-26). To eliminate this error, an iterative procedure is used. This involves recomputing accelerations for t_1 using the velocities and displacements from the initial computation. These accelerations are then used in Equation (B-27) to obtain more accurate average velocities than were obtained the first time when it was assumed that the initial acceleration remained constant over the time interval. The new velocities $\dot{\Delta}_1$ are then used in Equation (B-28) to obtain more accurate final displacements.

The cycle of acceleration, velocity and displacement computations is repeated until convergence to a satisfactory number of digits. Convergence is extremely rapid, particularly when time intervals are small enough to avoid rapid changes in acceleration between time intervals. After convergence has been obtained, the computation proceeds to $t = t_2$ and repeats the process already described here for $t = t_1$, etc. In this manner, time histories for $\ddot{\Delta}$, $\dot{\Delta}$ and Δ are computed.

APPENDIX C

MATRIX INSTABILITY ANALYSIS PROCEDURE-LINEAR

1. THEORETICAL BASIS

Elastic instability can occur for prismatic thin-walled structures or thin shells, where the behavior across the thickness can be subdivided into "flexural" and "midplane" behavior. By virtue of displacements normal to the midplane, the membrane forces have components which tend to enhance these displacements. When their magnitude is sufficiently large they produce – in the context of linear theory – infinitely large displacements for infinitesimal changes of the applied load. The values of applied load which produce the membrane stress state to cause this instability are the "critical loads".

In the case of straight beams and flat plates, the membrane forces are entirely independent of flexural behavior if finite displacements are disregarded in the formulation of the strain-displacement equations. For more general configurations such as shells, however, the applied loads produce membrane and flexural deformations which are related to each other. These influences are accounted for in the present elastic instability analysis process, although the nonlinear terms in the strain-displacement equations continue to be disregarded.

2. THEORETICAL BASIS

Although the interaction between the membrane and flexural behaviors is accounted for in the overall analysis procedure for the assembled structure, the elements are in themselves flat elements and their membrane and flexural stiffness relationships can be developed separately.

In view of this independence of element flexural and membrane behaviors, one can partition a plate element (Figure C-1) stiffness matrix, given earlier as Equation A-1 of Appendix A, as follows

$$\begin{Bmatrix} F_{x'} \\ F_{y'} \\ F_{z'} \\ M_{x'} \\ M_{y'} \end{Bmatrix} = \begin{bmatrix} K_m & & & & \\ & & & & \\ & & & & \\ & & & & \\ & & & & \end{bmatrix} \begin{Bmatrix} u' \\ v' \\ w' \\ \theta_{x'} \\ \theta_{y'} \end{Bmatrix} \quad (C-1)$$

where the primes designate "local coordinates (the coordinate system affixed to the element)".

The membrane stiffness for the flat plate element is not directly affected by instability considerations. As shown subsequently, however, element stiffness for flexural behavior in the presence of membrane forces becomes the sum of two component stiffnesses:

$$[K_f] = [K_b] + [n] \quad (C-2)$$

where $[K_b]$ is the stiffness for flexural behavior in the absence of instability effects (the conventional flexural stiffness matrix) and $[n]$ represents the effects of the element membrane forces on the element flexural behavior. The terms of $[n]$ consist of the dimensions of the element and the values of the membrane forces acting upon the element. Material properties do not appear in the $[n]$ matrix.

Using Equation (C-2), the total element stiffness matrix can be written as

$$\begin{Bmatrix} F_{x'} \\ F_{y'} \\ F_{z'} \\ M_x \\ M_y \end{Bmatrix} = \begin{bmatrix} K_m & 0 \\ - & - \\ 0 & K_b \end{bmatrix} \begin{Bmatrix} u' \\ v' \\ w' \\ \theta_{x'} \\ \theta_{y'} \end{Bmatrix} + \begin{bmatrix} 0 & 0 \\ - & - \\ 0 & n \end{bmatrix} \begin{Bmatrix} u' \\ v' \\ w' \\ \theta_{x'} \\ \theta_{y'} \end{Bmatrix} \quad (C-3)$$

The coupling of membrane and flexural behaviors in a complete analysis stems from the coupling of the elements at the joints. In the general case, the respective elements will be randomly oriented with respect to the system axes. When joining the elements at the node points (i.e., when applying the conditions of joint equilibrium), a given force component in a particular local direction will be transformed into components in all three system directions. As shown in Figure C-2 in two dimensions, the $F_{x'_A}$ force is transformed into components of both F_{x_A} and F_{y_A} when the equations of equilibrium are written at point i. By virtue of this operation, the respective force components of the elements in local coordinate directions contribute to all three directions in the system-coordinate equations for the complete structure. Thus, in the presence of instability effects, the latter have the following general form:

$$\begin{Bmatrix} P_x \\ P_y \\ P_z \\ M_x \\ M_y \\ M_z \end{Bmatrix} = \begin{bmatrix} K_{PP} & K_{PM} \\ - & - \\ K_{MP} & K_{MM} \end{bmatrix} \begin{Bmatrix} u \\ v \\ w \\ \theta_x \\ \theta_y \\ \theta_z \end{Bmatrix} + \begin{bmatrix} N_{PP} & N_{MP} \\ - & - \\ N_{MP} & N_{PP} \end{bmatrix} \begin{Bmatrix} u \\ v \\ w \\ \theta_x \\ \theta_y \\ \theta_z \end{Bmatrix} \quad (C-4)$$

or $\{P, M\} = [K] \{\Delta\} + [N] \{\Delta\}$

Equations (C-4) are the governing equations for the total problem. In particular, it is to be noted that the evaluation of the $[N]$ matrix requires a knowledge of the membrane stress state. Classical analysis techniques commonly assume that the membrane stress state is unaffected by flexural deformation. Based on this assumption, a membrane stress state is readily determined. The same approach can, of course, be taken on a discrete element analysis. The determinate membrane stress state would be hand computed and used to calculate the $[N]$ matrix.

The digital computation procedure has been arranged, however, so that the latter simplification need not be made. Consider first an equilibrium analysis, where the applied loads are not large enough to cause buckling. The analysis would begin with the $[N]$ matrix first set equal to zero - instability effects are disregarded. The solution for displacements is then

$$\{\Delta\} = [K]^{-1} \{P, M\} \quad (C-5)$$

The so-determined values of $\{\Delta\}$ are next used in the element stress equations (see Equation A-4 of Appendix A and the related discussion) to obtain a first guess for the membrane stresses. These membrane stresses account for the influence of bending. With these membrane stress values, the matrix $[N]$ can be constructed and Equation (C-4) is solved as follows

$$\{\Delta\} = [K + N]^{-1} \{P, M\} \quad (C-6)$$

Again, element membrane stresses are evaluated and the process continues iteratively until convergence.

To predict buckling, the approach taken involves a sequence of eigenvalue determinations for a succession of assumed applied load levels. In a given eigenvalue determination, based on an assumed applied load level, it is assumed that all midplane forces are at a fixed ratio to one another at all levels of applied load--from the load level chosen up to the specific value predicted to cause instability in the eigenvalue determination. Thus, Equation (C-4) is written as:

$$\{P, M\} = [K] \{\Delta\} + \lambda [N] \{\Delta\} \quad (C-7)$$

where $[N]$ is constructed from membrane stresses consistent with the assumed applied load level and λ is the scalar multiplier which defines the buckling level consistent with the membrane stress state for the assumed applied load level. Setting $\{P, M\}$ equal to zero for the purposes of eigenvalue analysis

$$0 = [K] \{\Delta\} + \lambda [N] \{\Delta\} \quad (C-8)$$

$$\frac{1}{\lambda} \{\Delta\} = -[K]^{-1} [N] \{\Delta\} \quad (C-9)$$

Using matrix iteration, the above can be solved for the eigenvalues λ_i and the associated eigenvectors $\{\Delta_i\}$. There will be as many such eigenvalues as there are

equations in (C-8), but the only eigenvalue of interest is the largest value of $\frac{1}{\lambda}$ representing the smallest λ_i and, therefore, the lowest magnitude load at which elastic instability will be experienced.

The actual buckling load will, of course, occur only when the determined $\lambda = 1.0$. To accomplish this, a trial and error process is attempted. First, an obviously low value of applied load is assumed, resulting in a high value of (> 1.0). This is shown as Point A in Figure C-3. Correspondingly, if the assumed load level is higher than that which causes buckling, the predicted λ will be less than 1.0 (Point B). By obtaining values of λ at various assumed load levels (Points C & D), the load level for buckling can be determined (Point E).

It should be noted that the determination of λ for an assumed buckling load level is accomplished only after a sequence of iterative analyses has been performed (in the manner described previously) to determine a convergent membrane stress system and, therefore, $[N]$ matrix.

3. ELEMENT RELATIONSHIPS

Procedures for formulating discrete element force-displacement equations were reviewed earlier, in Appendix A. These procedures are based on the use of Castigliano's Theorem, which, in the formulation of a stiffness matrix takes the form

$$[K] = ([B]^{-1})^T [C] [B]^{-1} \quad (C-10)$$

where $[B]$ is the matrix defining the element node point displacements $\{\Delta_e\}$ as a function of the undetermined parameters, of the assumed displacement functions for this element, i.e.

$$\{\Delta_e\} = [B] \{a\} \quad (C-11)$$

and $[C]$ is a matrix, each row of which represents the derivative of the strain energy of deformation of the element (U) with respect to one of the undetermined parameters.

Reference 6 shows that the above approach can be employed in the derivation of stiffness matrices which include instability effects if $[C]$ is expressed as the sum of two matrices

$$[C] = [c_b] + [c_n] \quad (C-12)$$

where $[c_b]$ derives from the strain energy for flexure along, (U_b) and $[c_n]$ represents the work done by the edge membrane forces acting through the edge displacements of the element (U_n).

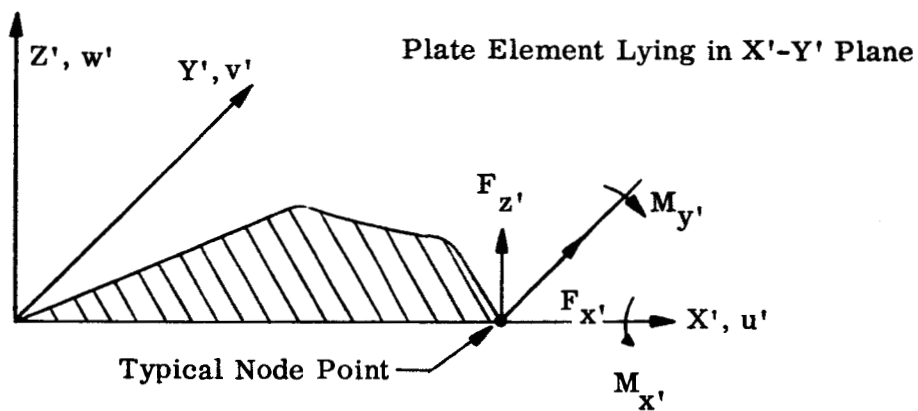


Figure C-1. Flat Plate Element

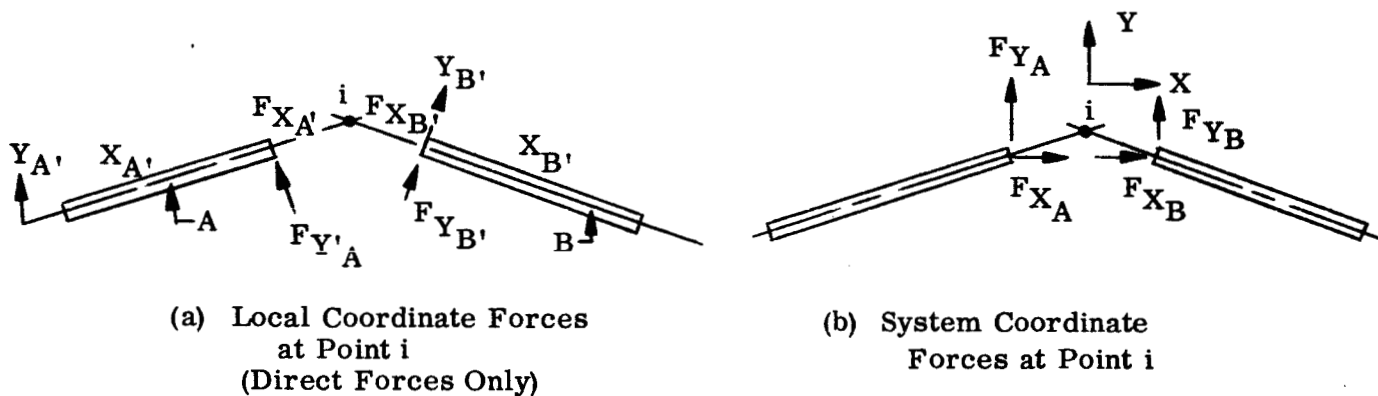


Figure C-2. Joint Equilibrium Conditions

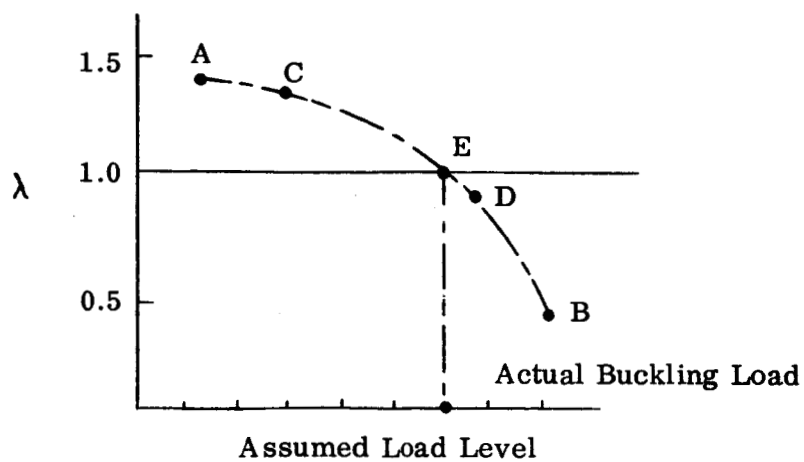


Figure C-3. Iterative Determination of Critical Load

For plates,

$$U_n = -\frac{i}{2} \int_A \left[N_x \left(\frac{\partial w}{\partial x} \right)^2 + N_y \left(\frac{\partial w}{\partial y} \right)^2 + 2 N_{xy} \left(\frac{\partial w}{\partial x} \right) \left(\frac{\partial w}{\partial y} \right) \right] dA \quad (C-13)$$

U_b was given previously, in Appendix A

Substituting (C-12) and (C-10)

$$[K] = ([B]^{-1}) [C_b] [B]^{-1} + ([B]^{-1})^T [C_n] [B]^{-1} \quad (C-14)$$

so that, by comparison with Equation (C-2)

$$[K] = ([B]^{-1})^T [C_b] [B]^{-1} \quad (C-15)$$

$$[n] = ([B]^{-1})^T [C_n] [B]^{-1} \quad (C-16)$$

Using the above concepts, and the assumed plate element deflectional nodes described in Appendix A, detailed derivations of the flexural stiffnesses for the triangle and quadrilateral have been performed and are presented in Reference 3.